UNIVERSITÀ DEGLI STUDI DI PALERMO
INAF - OSSERVATORIO ASTRONOMICO DI PALERMO

Dottorato in Scienze Fisiche
Dipartimento di Fisica e Chimica (DiFC)
Settore Astronomia e Astrofisica (FIS/05)

PLANETS AROUND LOW-MASS STARS AND STELLAR ACTIVITY EFFECTS

IL DOTTORE
Esther González Álvarez

IL COORDINATORE
Prof. Gioacchino Massimo Palma

IL TUTOR
Prof.ssa Giuseppina Micela

CICLO XXX
ANNO CONSEGUIMENTO TITOLO 2018

Dedicated to my parents

Contents

List of Figures

List of Tables

Abstract

In the last years the field of exoplanet research has focused its interest in M dwarfs. These stars have became the favourite targets in radial velocity surveys, specially when looking for small planets in the habitable zones of their parent stars. Not only for being the M dwarfs the most common objects in our Galaxy also because the Doppler signals due to small planets orbiting around them are larger and more easily detectable than those around FGK stars.

However, stellar magnetic activity and rotation affect the measured radial velocities as surface inhomogeneities rotating with the stellar surface can cause periodic changes in the spectral line centroid. Disentangle these stellar activity effects from the planetary signals is a challenge, specially for M dwarfs, which retain high magnetic activity levels for long time and, on average are more active than solar-like stars. For these reasons understanding stellar activity, in particular for M dwarfs, is crucial for the detection of exoplanets through the radial velocity technique.

Therefore, in the first part of this thesis we use a sample of 78 late-K/early-M dwarfs with relatively low activity levels observed with the HARPS-N high-resolution échelle spectrograph at the Telescopio Nazionale Galileo (Spain) in the framework of the HArps-N red Dwarf Exoplanet Survey (HADES), in order to test whether the relations between activity, rotation and stellar parameters and flux-flux relationships investigated in the literature for main-sequence FGK stars and for pre-main-sequence M stars also hold for early-M dwarfs. Our results show that early-M dwrafs follow the same relations of more massive stars and, more important, our data allow us to explore the slow rotation regime, poorly covered by previous studies. This regime for low mass stars is particularly interesting since the involved relatively long periods overlap with the periods corresponding to the habitable zone around these stars. The results of this study are part of several published papers within the HADES collaboration: Scandariato et al. (2017), Maldonado et al. (2017) and Suárez Mascareño et al. (A&A, in press).

In the second part of this thesis, we discuss in detail the analysis developed to search for planets in the low-mass star domain. In particular we focus on the analysis of GJ 720 A, an M0.5 M dwarf, that presents an interesting high significant periodic signal suggesting the presence of a companion. Our candidate planet would have a minimum mass around 13 $M_{\oplus}$ and an orbital period of 19.487 ± 0.008 days. With this characteristics our planet would occupy an interesting region of super-Earths poorly populated. To definitively verify our hypothesis further studies such as the photometric light curve or Gaussian processes analysis will be performed. Also in this part we will discuss the analysis of GJ 521 A, an M1.5 dwarf, that show some of the problems that arise when the radial velocity variations are due to stellar activity, stressing the crucial interest on understanding the stellar activity in M dwarfs that can be easily frustrate the identification of planetary signals.

Finally, in the last part of this thesis we present a different approach applied to a red giant star, TYC-4282-605-1. We discovered an orbiting low-mass companion with a period of 101 days using a multi-wavelength approach. This work was a pilot programme for the GIARPS project, the new observing mode at the TNG using at the same time HARPS-N (visible) and GIANO (NIR) spectrographs. Our study let us to confirm for the first time a planet around a giant star using quasi-simultaneous RVs in VIS and NIR. All these results have been published by González-Álvarez et al. (2017).

Keywords: Stars: activity - Stars: low-mass - Techniques: radial velocities - planetary systems

Chapter 1

Introduction

Understanding the evolution of planets and planetary systems is one of the most exciting and dynamics frontiers in modern Astrophysics. Any planet is an extremely faint light source compared to its parent star. Astronomers have generally had to resort to indirect methods to detect extrasolar planets. Since most of the planets cannot be observed directly, the planet hunters decided to observe stars, and look for the slight effects that orbiting planets can induce in their hosting stars.

1.1 Methods of detecting exoplanets

In the following some of the different and most used approaches in detecting exoplanets are explained including in detail the principal method used in the development of this thesis, the radial velocity method.

Each method has its own biasses and measure different planetary properties. The most used methods, for example, the spectroscopic measurements of radial velocity (RV) and photometric light curve measure mass and radius, respectively.

1.1.1 Transit Photometry

If a planet crosses (transits) in front of its parent star's disk, then the stellar brightness drops by a small amount depending on the relative radii of the star and the planet (see Fig.1.1). Observations of brightness variations can immediately reveal several parameters about the system as the radius. One advantage is that combining transit method with detection methods that yield mass (e.g. radial velocity method), it can be estimate planet's density.

Another important advantage of this method is the possibility to study the atmosphere of the transiting planet, nowadays one of the most important goals in extrasolar planet science. When a planet transits the star, light from the star passes through the upper atmosphere of the planet and by studying the changes in the stellar spectrum at different wavelengths one can construct an absorption spectrum which will determine the composition of the planet's atmosphere. Analogously it is possible to study the reflected spectrum at the secondary transit (eclipse).

Transit photometry is currently the most effective and sensitive method for detecting extrasolar planets. The Kepler mission (Borucki et al. 2010), launched in March of 2009, uses photometry to search for extrasolar planets from space. The spacecraft's sensitivity is such that it has already detected thousands of planetary candidates, including several that are Earth-sized and orbiting in their star's habitable zone.

The main difficulty with this method is that a transit must occur. This means that the distant planet must pass directly between it's star and the Earth. Assuming a random orientation distribution, the probability of a transit is very low and can be expressed as a function of the planetary orbit, and the planetary and stellar radii:

$$P_{tr} = 0.0045 \left(\frac{AU}{a}\right) \left(\frac{R_\star + R_p}{R_\odot}\right) \left[\frac{1 + e\cos(\pi/2 - \omega)}{1 - e^2}\right] \tag{1.1.1}$$

where ω is the angle at which orbital periastron occurs, and e is the orbital eccentricity.

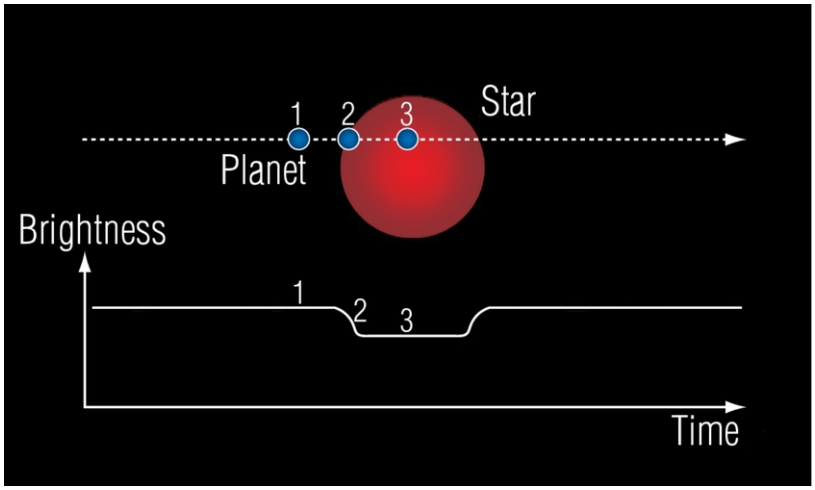

Figure 1.1: Planetary transit. When the planet moves in front of its star, the star's luminosity decreases, and returns to its former level when the transit is completed. Figure taken from planetary.org: http://www.planetary.org/explore/space-topics/exoplanets/transit-photometry.html

1.1.2 The Microlensing Method

Gravitational microlensing occurs when the gravitational field of a star acts like a lens, magnifying the light of a distant background star. The resulting effect is a sudden dramatic increase in the brightness of the lensing star, by as much as 1,000 times. This effect occurs only when the two stars are almost exactly aligned (see Fig. 1.2) and is an astronomical effect predicted by Einstein's General Theory of Relativity.

Microlensing is the only known method capable of discovering planets at truly great distances from the Earth. Whereas radial velocity searches look for planets in our immediate galactic neighbourhood, up to 100 light years from Earth, and transit photometry can potentially detect planets at a distance of hundreds of light-years, microlensing can find planets orbiting stars near the center of the galaxy, thousands of light-years away.

Unlike planets detected by other methods, which are associated with particular stars and can be observed repeatedly, planets detected by microlensing will never be observed again. This is because microlensing events are unique and do not repeat themselves.

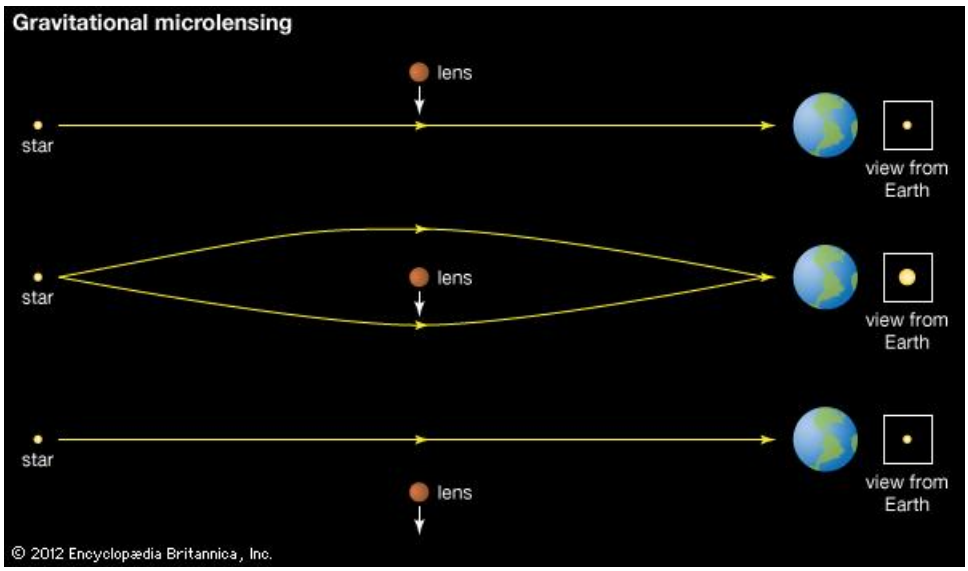

Figure 1.2: Brightening of a star by an object passing between the star and an observer. Figure from Encyclopaedia Britannica, Inc: https://www.britannica.com/topic/gravitational-microlensing

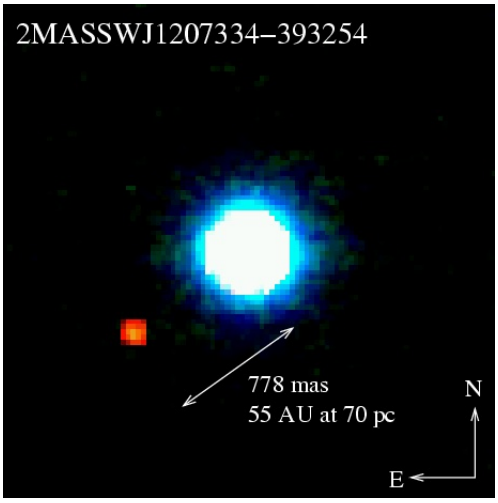

Figure 1.3: Planetary-mass object in orbit around brown dwarf 2M1207. Figure from Chauvin et al. (2004).

1.1.3 The Direct Imaging Method

Direct imaging of exoplanets is extremely difficult, and in most cases impossible because they are faint light sources compared to stars. Nevertheless, with actual telescope technology a planet can be directly observed if the adequate conditions are reached (see Fig. 1.3).

In July 2004 a group of astronomers using the European Southern Observatory's Very Large Telescope Array imaged a planetary mass object, several times the mass of Jupiter and close to a brown dwarf called 2M1207 (Chauvin et al. 2004). The star distance is 200 light years from Earth and the planet was considered to be the first directly imaged exoplanet.

Direct imaging works better for planets that orbit at a large distance from their host stars, and that are positioned face-on when observed from Earth. This makes this method complementary to the radial velocity or transit methods, which are most effective for planets orbiting close to the star.

1.1.4 The Radial Velocity Method

The radial velocity (RV) method, based on Doppler spectroscopy, has played a fundamental role in exoplanetary science. It is one of the most effective method for locating extrasolar planets with over 1000 exoplanets discoveries.

We would probably not be studying exoplanets today if were not for RV measurements. The first exoplanet discovered around a solar type-stars was 51 Peg b (Mayor & Queloz

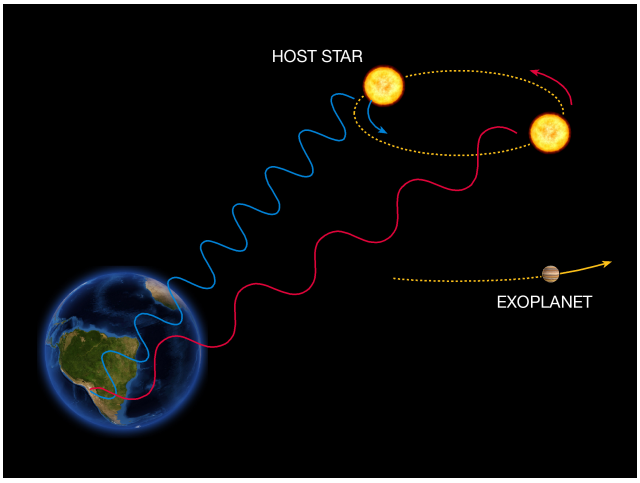

Figure 1.4: Doppler shifts due to stellar wobble. Figure from The European Southern Observatory (ESO): https://www.eso.org/public/unitedkingdom/images/eso0722e/

1995) more than 20 years ago with this method.

The RV method relies on the fact that a star does not remain stationary when it is orbited by a planet. It moves responding to the gravitational tug of its smaller companion around the centre of mass of the star-planet system. One can measure motions of the star along the line of sight (radial) via the Doppler effect. When the star is moving towards the observer, then its spectrum would appear slightly shifted towards the blue and if it is moving away, it will be shifted towards the red (see Fig. 1.4).

Using highly sensitive spectrographs, we can track a star's spectrum, searching for periodic shifts towards the red, blue, and back again. If the shifts are regular, repeating themselves at fixed intervals of days, months, or even years, it means that the star is moving back and forth towards the line of sight in a regular cycle.

The Doppler shift of a star due to the presence of a planetary companion depends on the mass, the period and therefore on the distance of the planet to its host star. So, more massive and close-in planets are easier to detect. Early on, most of the planets detected by spectroscopy were of a type known as hot Jupiters. These are giant planets composed mostly of gas, similar to our Jupiter, but orbiting at very fast speeds at a very short distance from their star. Their close proximity and short periods can produce large stellar reflex motions than can be detected by spectroscopy. On the contrary, cool planets orbiting at large distance from the star produce small reflex motions, factor which makes them much harder to detect with RV method.

We can get an estimate of the reflex motion of the star using the Kepler's third law:

$$P^2 = \frac{4\pi^2 a^3}{G(M_s + M_p)} \tag{1.1.2}$$

where M_s is the mass of the star, M_p is the mass of the planet, P the orbital period, a the semi-major axis and G is the gravitational constant.

For planets $M_s \gg M_p$. If we assume circular orbits and the fact that $M_p \times a_p = M_s \times a_s$, where a_s and a_p are the semi-major axes of the star and planet, respectively, we can derive the amplitude of the barycentric radial velocity variations, V, as:

$$V\ [m\ s^{-1}] = 28.4 \left(\frac{P}{1\ yr}\right)^{-1/3} \left(\frac{M_p \sin i}{M_{Jup}}\right) \left(\frac{M_s}{M_{sun}}\right)^{-2/3} \tag{1.1.3}$$

where i is the inclination of the orbital axis to the line of sight. Fig. 1.5 shows the reflex motion of a one solar mass star due to various planets at difference orbital distances calculated with Eq. 1.1.3. A Jupiter mass planet orbiting a one solar mass star at an orbital distance of 5.2 AU and with a period of 12 years will induce an 11.8 m s^{-1} reflex motion in the host star. The same Jupiter mass planet closer to the star would induce an amplitude of several hundreds of m s^{-1}. For an Earth planet at 1 AU we see that the reflex motion caused on

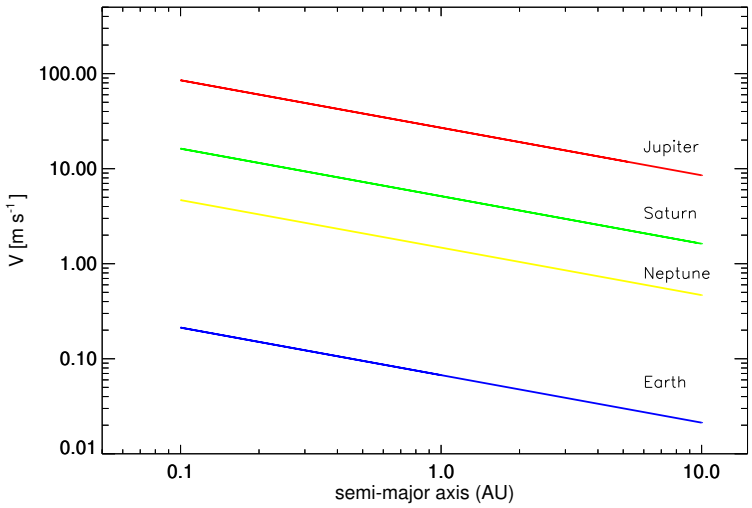

Figure 1.5: The amplitude of the barycentric radial velocity variations for a one solar mass star orbited by the Earth, Neptune, Saturn and Jupiter at several orbital distances.

the host star would be 10 cm s^{-1} and this only increases a little more by moving this planet to 0.1 AU.

The success of the RV method was made possible by the development in recent years of extremely sensitive spectrographs, which can detect even very small movements of a star. Currently, modern techniques are able to achieve an RV precision of 0.5-1 m s^{-1} thanks to HARPS (the High Accuracy Radial velocity Planet Searcher, Mayor et al. 2003) echelle spectrograph located in the Southern hemisphere, at the ESO La Silla 3.6 metre telescope and its twin for the Northern hemisphere HARPS-N echelle spectrograph (Cosentino et al. 2012) installed at the Italian Telescopio Nazionale Galileo (TNG), a 3.58 metre telescope located at the Roque de los Muchachos Observatory on the island of La Palma, Canary Islands, Spain. See Section 2.1 for more details about the TNG telescope and its instruments.

The main scientific goals of these two instruments are the discovery and characterization of terrestrial super-Earths by combining the measurements using transit photometry (obtained with high precision photometry from space) and Doppler spectroscopy which provide both, the size and mass of the exoplanet and they are able to achieve the measurement of RV with the highest accuracy currently available.

This spectacular increase in RV precision was reached through three developments: high quantum efficiency electronic detectors, large wavelength coverage cross-dispersed echelle spectrographs and the simultaneous wavelength calibration.

Unfortunately spectral resolution and signal-to-noise (S/N) of our data are not the only factors that influence the RV measurements precision. The properties of the star can have a much larger effect, as not all stars are appropriate to conduce precise RV measurements.

Stellar doppler shift measurements depend on the presence of spectral features in the spectrum and its bases are the measurements of numerous spectral lines present in stellar spectra. The stars emit most of their electromagnetic energy between the UV and mid-IR spectral range but the UV and mid-IR domains are not accessible from the ground. So, the RV technique has always focused on spectral lines in the visible and near-IR regions. Stellar spectra vary widely with the effective temperature of the stars. On the hot stars all chemical elements are at least partly ionized and the atomic energy levels responsible of electronic transitions are depopulated in the visible and near-IR. This effect and the high rotation rate of hot stars yield RV measurements that are not very precise. Contrary, solar-type stars and M dwarfs exhibit thousands of absorption lines in their spectra.

Left panel of Fig. 1.6 shows the spectral region of two stars, corresponding the top and lower figures with a A7 and a K0 star, respectively. The hot star shows only one spectral

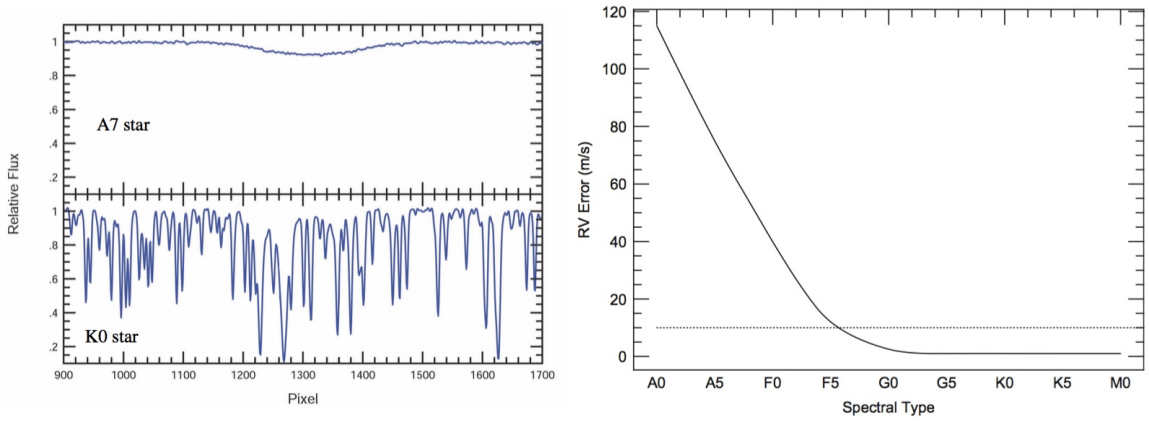

Figure 1.6: *Left panel top:* A spectrum of a A7 star with high projected rotation. *Left panel bottom:* The spectrum of a K0 star. *Right panel:* The expected radial velocity error as a function of spectral type. The *horizontal line* marks the precision of 10 m s^{-1} needed to detect a Jovian-like planet. Taken from Bozza et al. (2016)

line in this region and it is quite wide and smooth due to the high rotation of the star. It is difficult to determine the centroid position and thus the doppler shift of this spectral line. In the case of the cooler star we see many spectral lines in this region which are much more narrow due to the slow rotation of the star. In this case the radial velocity can be very precise.

In the right panel of Fig. 1.6 the RV error as a function of stellar spectral type is shown. The horizontal dashed line indicates the 10 m s^{-1} that are needed to detect a Jovian planet at 5 AU orbiting around a Sun-like star. For early spectral types the RV error is very large, but for spectral types later than F6 the RV error decreases substantially. There are two factors that play an important role. First, the rotation of the stars decreases for spectral types later than F6. This spectral type marks the starting of the outer convection zone of the star. The convection zone is the motor for the stellar magnetic activity and becomes deeper for cooler stars breaking the star's rotation. Second, the number of spectral lines in the spectrum decreases with increasing effective temperature (i.e, when moving to early spectral types). This explains why most RV exoplanets discoveries were found for host stars later than spectral type F6.

Measuring Doppler shifts with a precision of 1 m s^{-1} (achieved today) is a truly challenging task from an instrumental point of view. Normally it cannot be achieved using a single spectral line because of insufficient S/N. Only the use of thousands of lines makes it

possible to reach such high levels of precision. Therefore all stellar phenomena that could deform or modify the spectral lines contribute to dismiss the radial velocity precision.

1.2 Stellar activity

Currently, rather than the instrumental precision the main challenge to high doppler precision is the star itself. The stellar noise (result from physical phenomena associated with the star) is more difficult to minimize because the error in RV is dominated by intrinsic stellar noise (S/N) and line richness (density and depth) instead of instrumental errors.

Sources of intrinsic stellar noise can be oscillations, stellar activity (e.g., spots), granulation, convection patterns as well as radial and non-radial pulsations (Hatzes & Cochran 2000). These phenomena may occur on several time scales (see Table 1.1) and are expected to produce changes in the shape of the spectral line profile which can be misinterpreted with velocity shifts (Hatzes 1999; Hatzes et al. 1999) hardly distinguishable from those induced by a low-mass companion:

- Spots

  In Fig. 1.7 it can be seen that if the stellar surface presents no features, the Doppler shifts from both sides give the same contrinution with the net effect to broaden the line in a symmetric way. While if a starspot is present in the stellar surface rotating as the star rotates, it blocks some of the flux of the star, inducing an imbalance between the redshifted and blueshifted halfs of the star. This produces an asymmetry in the shape of the total line profile shifting its centroid by a small amount. These perturbations in the line profile can be translate into RV variations (stellar jitter) due to sunspots. Stellar jitter due to the rotational modulation of starspots is wavelength dependent and smaller in amplitude at longer (redder) wavelengths due to the lower flux contrast

Table 1.1: Main sources of intrinsec stellar noise with their typical amplitudes and time scales. Data from Bozza et al. (2016).

Phenomenon	RV amplitude m s^{-1}	Time scales
Solar-like oscillations	0.2-0.5	$\sim$ 5-15 min
Stellar activity	1-200	$\sim$ 2-50 days
Granulation/Convection pattern	$\sim$ few	$\sim$ 3-30 years

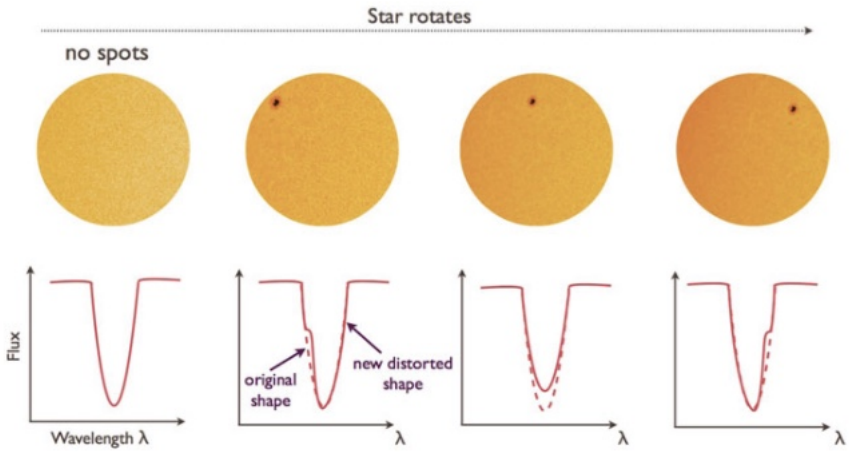

Figure 1.7: The diagram shows how flux blocked by starspots induces asymmetries in the spectral lines and produces variations in RV.

between star-spots and the stellar photosphere. For more active and rapidly rotating stars the starspot induced RV variations can be much bigger than the variation due to a planet as showed by Saar & Donahue (1997). Note that the most important source of stellar noise errors in Sun-like stars is the activity in form of cool spots, hot faculae and plagues.

For long-lived spots (time scale $>$ stellar rotation) the RV variations due to the activity will be coherent and appear as a periodic signal with a period corresponding to the rotational period. Spots can also migrate in longitude and latitude changing the rotational period due to differential rotation. This creates very complex time series that can hide the real planetary signal, in particular the ones with small RV amplitudes.

- Stellar oscillations.

  Stellar oscillations, in general, do not present a big problem for the RV in the detection of exoplanets because their amplitudes are small and more important their time scales are short. It is possible to remove the oscillation noise by taking an exposure longer than those time scales or by co-adding observations.

- Convection.

  Stellar magnetic activity occurs in all stars with a sufficient degree of rotation and convection, and both are required in the standard α - ω dynamo theory of magnetic

field generation (Noyes 1984). The stellar surface magnetic activity can show a complex convective pattern through convective cells within inflows and outflows of matter. The variability of the convection pattern impacts on stellar radial velocities and therefore on exoplanet detectability. The time scales of convection pattern of the star are associated with the stellar activity and can be a problem when trying to find long period planets.

- Pulsations.

  Precise radial velocities measurements can also provide knowledge of stellar pulsations and have already shown that the K giants are a new class of pulsating stars. The RV variations of these objects can show amplitudes between $\sim$ 50-400 $m\ s^{-1}$ and can be multi-periodic with several periods ranging between tens to hundreds of days and arise from radial and non-radial pulsations (Hatzes et al. 1999). The period of the fundamental radial mode of pulsation is considered as the entire star expands and contracts together. The pulsational radial velocities variations have been studied and their RV amplitude shown a strongly dependence with the spectral region used for computing radial velocity showing the complex behaviour of these stars.

All these phenomena (responsible of the RV variations) can produce alterations (variations of the asymmetries) on the spectral line profiles of the stars. A direct measure of these activity jitter (Queloz et al. 2001) can be performed considering variations of line bisector (e.g. Martínez Fiorenzano et al. 2005; Stempels et al. 2007). The line bisector of an absorption line is the combination of bisector points from the core toward the wings of the lines with the same flux level between the left and right sides of the line profile (see top panel of Fig. 1.8). For example, an inhomogeneous distribution of spots on the stellar surface will make the line profiles appear asymmetric, which is detectable as a change in the line bisector. In order to quantify the asymmetry of the line profile, bisector velocity span (BVS) is used. It can be determined through a top zone near the wings and a bottom zone close to the core of the line. The difference between velocity values in the top and the bottom zones determines the BVS.

Any correlation between the BVS and the apparent radial velocity is often used as a strong indication that the radial velocity variations are indeed changes in the shape of the line profiles due to some process related to stellar surface features. Queloz et al. (2001) used an anti-correlation between the BVS and the observed radial velocity to show that spots can cause a periodic signal in the apparent radial velocity.

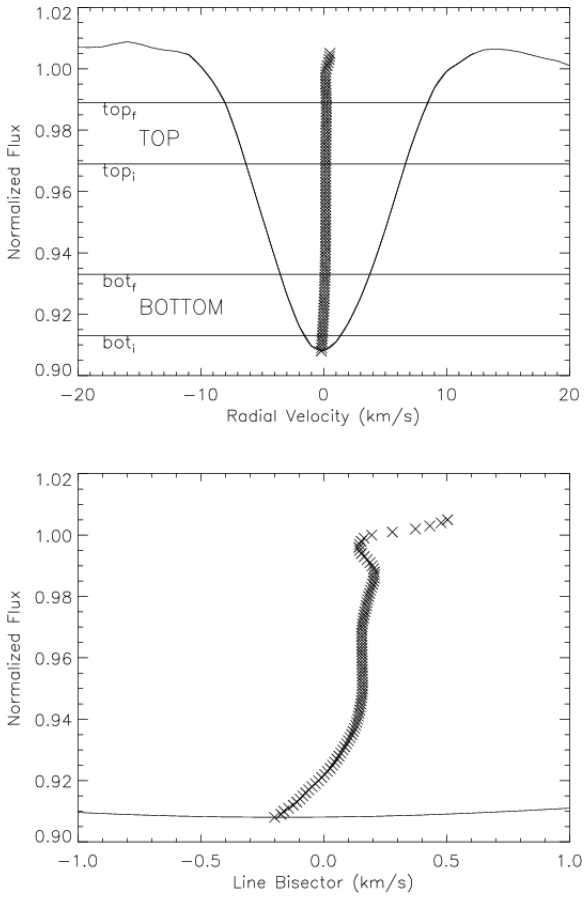

Figure 1.8: *Top panel:* The normalized cross correlation profile, the line bisector, is shown on the same velocity scale as the profile. *Bottom panel:* A zoom of the profile to better display the asymmetries of the line bisector. Figure taken from Martínez Fiorenzano et al. (2005).

In order to disentangle Keplerian variations from activity related signals is useful to determine the rotational period with independent methods as photometric measurements or Ca II H & K lines analysis or other activity indicators series. Alternatively we can take advantage of activity induced effects as spectral line bisector or multi-band RV determination.

The time-serie obtained are often sparse. In order to asses the presence of periodic variations it is necessary to use efficient methods sensitive to periodic variations. The most common method used in case of unequally spaced data to determine possible periodic signal is the Generalized Lomb-Scargle periodogram (GLS, Zechmeister & Kürster 2009). It is characterized by an efficient computation of a Fourier-like power spectrum estimator determining the periodic variations. The periodic variability found by GLS periodogram will be considered significant if the power of the corresponding period is higher than a chosen

confidence level. If this method is applied on activity indicators it allows us to determine the stellar rotation period or the periodic signal at which are produced pulsations, oscillations amongst others.

1.3 M dwarfs

Currently, the search for small, rocky planets with the potential capability of hosting life has been focused around M dwarf stars (dMs). These stars are relatively cool (approx. between 2200 and 4000 K), have masses smaller than $\sim 0.6 M_{\odot}$ and have several advantages. First of all, dM stars are the most abundant component of the solar neighbourhood, $\sim 75\%$ of the stars within 10 pc (e.g. Henry et al. 2006; Reid et al. 2002). Moreover, the contrast planet-star is more favorable. The motion induced by an Earth mass planet in the habitable zone around dM stars is of the order of 1 m s^{-1} (within today capabilities) while the same planet, as shown in Fig. 1.5, would induce a motion $\sim$ 10 cm s^{-1} around of solar-like star (e.g. Dressing & Charbonneau 2013; Sozzetti et al. 2013; Howard et al. 2012). M dwarfs are more likely to host rocky planetary companions (Bean et al. 2010). From an observational point of view, the chances of finding an Earth-like planet in the habitable zone of the star increase as the stellar mass and rotational period decreases (Kasting et al. 1993), as a consequence the small separation and shorter periods make the amplitude of the variation of RV large and, therefore, the temporal stability of the instrument is less constraining. The habitability is not guaranteed simply by an assessment of the distance from the star, several other factors such as stellar activity, may move the habitable zone of the star (Vidotto et al. 2013). Thus, it is crucial to understand the activity of M dwarfs and how it can affect the circumstellar environment.

M dwarf stars have large convective regions and they are on average more active than solar-like stars (Leto et al. 1997; Osten et al. 2005). Stellar activity describes the various observational consequences of magnetic fields, which appear on the stellar photosphere, in the chromosphere or in the corona. All these phenomena affect the circumstellar environment (including planets). Furthermore, as said in the previous section, magnetic inhibition of surface convection, spots, plagues, and other inhomogeneities of the stellar surface, all affect the shape of spectral lines inducing line profile distortion, and consequently affecting the measured radial velocity. For all these reasons understanding stellar activity of these stars is crucial.

We need to develop an optimal strategy to discern true keplerian signals from activity

induced radial velocity variations. This would help us in identifying small rocky planets orbiting in the habitable zone of M dwarfs.

The Kepler mission has recently shown that terrestrial planets are more frequent around M dwarfs compared to solar-like FGK stars, so in the last years M-dwarfs became more interesting targets for the search of planets. The NIR RV measurements would appear to be advantageous for many reasons: M dwarfs are intrinsically faint at optical wavelengths which makes them difficult targets, the spectral energy distribution of late-type M dwarfs peaks between 1 and 2.5 μm, so they can be better observed in the near-infrared region; further advantage of RVs measured from NIR spectra is that the jitter related to activity is reduced relative to visible measurements, because in the NIR the contrast between stellar spots or plagues and the rest of the stellar disk is reduced. Provided that RV can be measured with enough accuracy from NIR spectra, a comparison between variations of RV measured in the optical and NIR can establish the origin of the RV variations in an unambiguous way (González-Álvarez et al. 2017). For all these reasons there is a raising interest for measuring high precision RVs from NIR spectra. Recent technological improvements allowed to build stable high-resolution NIR spectrographs capable of delivering high RVs.

An example of these improvements can be GIANO (more details in chapter 2.1). GIANO is a near IR high resolution spectrograph (Oliva et al. 2006) mounted at the Nasmyth A focus of the TNG (Telescopio Nazionale Galileo). The instrument provides cross dispersed echelle spectroscopy at a resolution of 50.000 over the 0.95-2.45 μm spectral range in a single exposure. In particular, no other IR instruments have GIANO's capability to cover the entire NIR wavelength range. So, GIANO could be a fantastic option to study M dwarfs stars because it covers the range in which these stars emit most of their energy. Carleo et al. (2016) assessed the precision of the RV measurements obtained using spectra acquired with GIANO and the authors show that high precision RV are possible with GIANO using the telluric lines as reference, at least for stars with bright H-magnitude.

Considering the approximative error of HARPS-N, the most precise optical spectrograph in the nothern emisphere (see section 2.1): $N_{err\ HARPS-N}(\mathrm{km/s}) = 10^{0.2\mathrm{V}-4.5}$, and for GIANO: $N_{err\ GIANO}(\mathrm{km/s}) = 10^{0.2\mathrm{H}-3.05}$, the study by Carleo & Gratton (2015) states that GIANO provides more precision in the RV measurements than HARPS-N for stars with $\mathrm{V}-\mathrm{H} > 7.25$, corresponding to spectral types later than M6.5, as shown in Fig. 1.9 (left panel). GIANO is also advantageous for active stars. Considering that activity decreases with stellar age, GIANO offers the possibility to observe young stars. Right panel of Fig. 1.9 indicates when GIANO and/or GIARPS (more details in chapter 2.1) are better suited

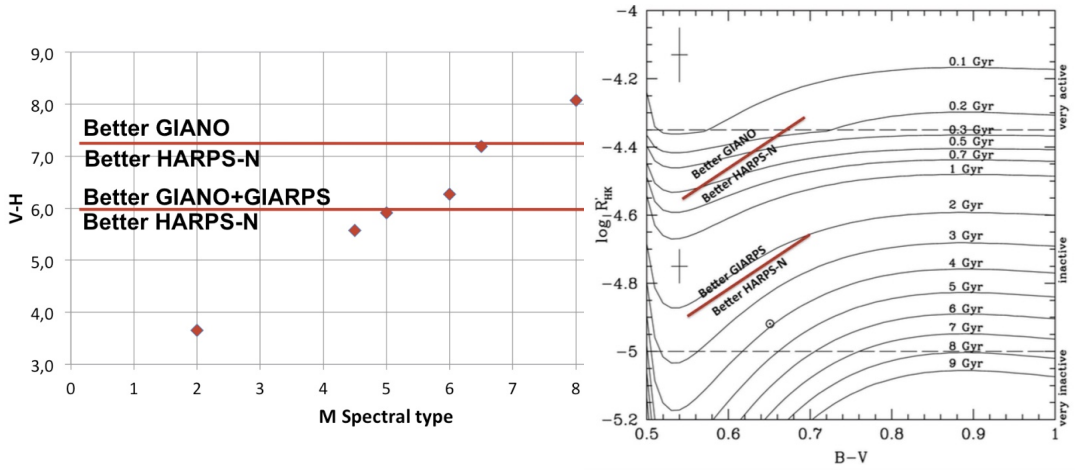

Figure 1.9: Comparison GIANO-HARPS-N. *Left panel:* Colour V-H vs. M spectral type. GIANO is better than HARPS-N for targets with a colour $>$ 7.25; with GIARPS, that means GIANO-B configuration with an absorbing cell, the sample includes stars with colour $>$ 6. *Right panel:* GIANO is better than HARPS-N for targets with age smaller than 0.2 Gyr. GIARPS enlarges the sample to ages of about 2 Gyr. Figure taken from Carleo & Gratton (2015).

to discover planets around young stars. The sample of targets for GIANO can grow if we consider GIARPS, a very new observing mode with a common feeding for HARPS-N and GIANO (see details in chapter 2.1).

1.4 The stellar sample

Part of the following work is based on the HADES project in which we monitor and analyse a sample of 78 late-K/early-M dwarfs with relatively low activity in a homogeneous and coherent way. The sample are currently been observed in the framework of the HArps-N red Dwarf Exoplanet Survey (HADES, Affer et al. 2016; Perger et al. 2017) a collaborative effort between the Global Architecture of Planetary Systems project (GAPS, Covino et al. 2013), the Institut de Ciències de l'Espai (ICE/CSIC) and the Instituto de Astrofísica de Canarias (IAC). The sample covers an effective temperature range from 3400 to 3900 K, corresponding to spectral types between K7 and M4V (Fig 1.10, left panel) and masses between about 0.2 and 0.7 $M_{\odot}$ (Fig. 1.10, right panel). We group the stars in bins of 0.5 spectral subclasses, with K7 corresponding to -1, M0 to 0, and so on until M4, which is the last sub-type for which we have stars in our sample.

The stars were selected from the Palomar-Michigan State University (PMSU) catalogue

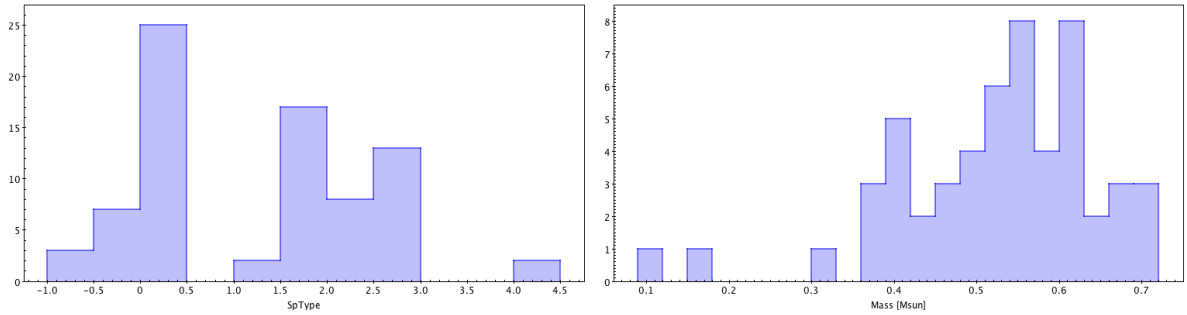

Figure 1.10: Distribution of SpT and masses for the HADES M dwarfs sample. Negative indices denote SpT earlier than M, where the value -1 stands for K7.

(Reid et al. 1995), Lépine & Gaidos (2011) and are targets observed by the APACHE transit survey (Sozzetti et al. 2013) with a visible magnitude lower than 12. Furthermore, most of the sample stars will have accurate Gaia (Gaia Collaboration et al. 2016) data. High-resolution échelle spectra of the stars were obtained at La Palma observatory (Canary Islands, Spain) during several observing runs between September 2012 and November 2017 using the HARPS-N instrument (Cosentino et al. 2012) at the Telescopio Nazionale Galileo (TNG). In order to determine stellar parameters for stars with more than one observation, spectra were combined into a single spectrum following the procedure described in Scandariato et al. (2017). Basic stellar parameters (effective temperature, spectral type, surface gravity, iron abundance, mass, radius and luminosity) were computed using a methodology based on ratios of spectral features (Maldonado et al. 2015a).

1.5 Main goal of this thesis

This thesis is the result of the work carried out during my PhD at the Osservatorio Astronomico di Palermo and the Università degli studi di Palermo. The thesis was planned as part of the project Global Architecture of Planetary Systems (GAPS). GAPS is a large observational programme with HARPS-N at the TNG. It is a structured, largely synergetic observational programme specifically designed to maximise the scientific return in several aspects of exoplanetary astrophysics, taking advantage of the unique capabilities provided by HARPS-N. The GAPS programme is composed of three main elements, including a) radial-velocity searches for low-mass planets around stars with and without known planets over a broad range of properties (mass, metallicity) of the hosts, b) characterisation measurements of known transiting systems, and c) improved determinations of relevant physical parameters

(masses, radii, ages) and of the degree of star-planet interactions for selected planet hosts. On the other hand, HADES (the HArps-N red Dwarf Exoplanet Survey) project being a collaborative effort between GAPS, the Institut de Ciències de l'Espai (ICE/CSIC) and the Instituto de Astrofísica de Canarias (IAC) allowed us monitoring and analysing the sample of 78 late-K/early-M dwarfs used in this work.

My thesis follows two main lines of research: i) the study of the presence of planets around M dwarfs stars using radial velocity method, and ii) the characterization of stellar activity in order to disentangle the radial velocity variations induced by stellar activity from those by planetary companion.

The structure of this thesis is as follows:

Chapter 2 includes all the information related to the observations, data reduction, telescopes and instruments used.

Chapter 3 includes all the studies on M stars related with activity indicators. The content of this chapter is included in Maldonado et al. (2017), Scandariato et al. (2017) and Mascareño et al. (A&A, in press).

Chapter 4 consists in a detailed analysis of M dwarfs stars data searching the presence of planets.

Chapter 5 contains the optical-NIR confirmation of a planet orbiting a K giant star. The work was performed in the elaboration of the article: "The GAPS Programme with HARPS-N at TNG XV. A substellar companion around a K giant star identified with quasi-simultaneous HARPS-N and GIANO measurements" (González-Álvarez et al. 2017)

Chapter 6 the summary and conclusions obtained in this Ph.D. thesis, as well as, the list of papers in which the results of this thesis are presented.

Chapter 2

Observations and data reduction

A summary of the instruments used in this thesis is presented in this chapter. Observations were carried out at the Telescopio Nazionale Galileo (TNG) located at the Roque de los Muchachos Observatory (ORM). With a primary mirror of 3.58 m, is one of the most important installation of the Italian astronomical community.

2.1 Instruments

2.1.1 HARPS-N

HARPS-N (High Accuracy Radial velocity Planet Searcher in North hemisphere) is an echelle spectrograph covering the wavelength range between 383 to 693 nm, with a spectral resolution R=115,000 (Cosentino et al. 2012). Table 2.1 summarizes the instrument properties and Fig. 2.1 shows an image of the spectrograph. This instrument allows the measurement of radial velocities with the highest accuracy currently available in the north hemisphere and is designed to avoid spectral drifts due to temperature and air pressure variations thanks to a very accurate control of pressure and temperature. HARPS-N is fibre-fed by the Nasmyth-B focus of the 3.6 TNG telescope through a Front End Unit (FEU). The two HARPS fibres (object + sky or Th-Ar) have an aperture on the sky of 1", this produces a resolving power of 115,000 in the spectrograph. Both fibres are equipped with an image scrambler to provide a uniform spectrograph pupil illumination, independent from pointing decentering.

The main scientific rationale of HARPS-N is the characterization and discovery of terrestrial planets by combining transits and Doppler measurements.

The HARPS-N Project is a collaboration between the Astronomical Observatory of the Geneva University (lead), the CfA in Cambridge, the Universities of St. Andrews and Edinburgh, the Queens University of Belfast, and the TNG-INAF Observatory.

Table 2.1: HARPS-N instrument description.
Data from TNG webpage: http://www.tng.iac.es/instruments/harps/

Spectrograph type	Fiber fed, cross-disperser echelle spectrograph
Spectral resolution	R= 115,000
Fiber field	FOV = 1”
Wavelength range	383 nm - 690 nm
Total efficiency	e = 8 % at 550 nm (incl. telescope and atmosphere at 0.8" seeing)
Sampling	s = 3.3 px per FWHM
Calibration	ThAr + Simultaneous reference (fed by 2 fibers)
CCD	Back illuminated CCD 4k4 E2V chips (graded coating)
Pixel size	15 μm
Environment	Vacuum operation - 0.001 K temperature stability
Global short-term precision	0.3 m/s (10^{-9})
Global long-term precision	better than 0.6 m/s (2x10E-9)
Observational efficiency	SNR = 50 per extracted pixel on a Mv=8 in 1 minute exposure
Wavelength accuracy	60 m/s (2×10^{-7}) on a single line

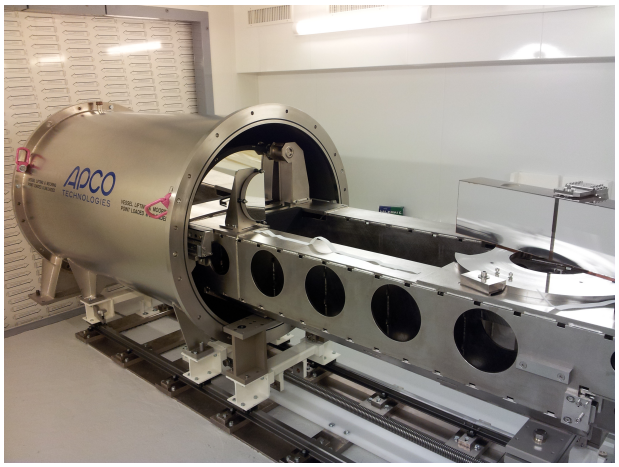

Figure 2.1: HARPS-N echelle spectrograph. Figure taken from TNG webpage: http://www.tng.iac.es/instruments/harps/

2.1.2 GIANO

GIANO is the NIR high resolution spectrograph of the TNG that was originally designed for direct feeding of light at the Nasmyth-B focus (Oliva et al. 2006). The instrument provides cross dispersed echelle spectroscopy at a resolution of 50,000 over the 0.95-2.45 micron spectral range in a single exposure (Y, J, H and K bands).

In July 2012 the spectrometer was provisionally positioned in Nasmyth-A focus (called GIANO-A) fed via fibers (Origlia et al. 2014). In October 2013 the Commissioning was completed and in September 2014 the Science Verification was successfully carried out. The spectrometer was offered to the community in 2015 (TNG call AOT31). In this provisional position, it was fiber-fed with two fibers of 1 arcsec angular diameter at a fixed angular distance of 3 arcsec on sky. GIANO has only one observing mode (R 50,000) and it can acquire spectra either of astrophysical objects and sky simultaneously, or of calibration lamps (halogen for flat-field and U-Ne for wavelength calibration) and dark frames. The GIANO detector and spectral characteristics are provided in Table 2.2 while Fig. 2.3 shows a picture of GIANO.

With the goal of optimize the instrument for planetary studies, the Italian exoplanetary community decided to invest the resources to realize a more appropriate interface for direct light-feeding that was designed and built. The spectrograph in this new configuration is now called GIANO-B now operating in Nasmyth-B. This new interface, that also includes a dichroic for simultaneous observations of GIANO-B and HARPS-N (GIARPS, Claudi et al. 2016), was successfully implemented and commissioned between August 2016 and March 2017.

Figure 2.2: Picture of Giano dewar in the TNG Nasmyth-A. Figure taken from TNG webpage.

Table 2.2: GIANO detector and spectral characteristics.

Parameters	Value
Detector	HAWAII-2 2048x2048
Pixel size	18 microns
Gain	2.2 e- / ADU
Readout Noise	5 e-
Dark Current	0.05 e- / s/pixel
Spatial resolution	0.25 arsec/pixel
Wavelength Coverage	0.95 - 2.45 microns
Spectral resolution	50000
Fiber Size	85 microns - 1.0 arsec on the sky
Slicer	2x

2.1.3 GIARPS

GIARPS is the observing mode with the new configuration of GIANO-B and HARPS–N having a new common feeding for both high resolution spectrographs, HARPS-N in the visible and GIANO in the NIR. GIARPS allows the two instruments mounted on the same focal station working simultaneously where is possible to take in a single exposure a high resolution spectrum from 0.383 μm to 2.45 μm.

The two instruments are also able to work separately, so we have three different observing modes: a) HARPS–N only (maintaining the current optical configuration with the already existing mirror); b) GIANO-B only; c) both: GIANO-B and HARPS–N splitting the light with a dichroic.

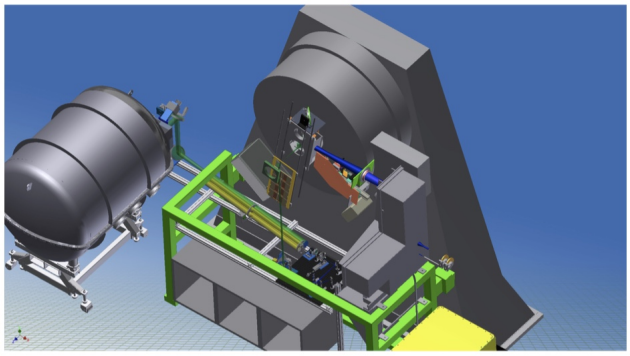

Figure 2.3: Mechanical solution for the housing of GIANO (left side) in Nasmyth-B. Figure taken from Claudi et al. (2017).

The flexibility of the three observing modes allow users to select the best wavelength range useful for their preferred science cases.

2.2 Data reduction

2.2.1 HARPS-N spectra

All spectra were automatically reduced using the Data Reduction Software (DRS V3.7, Lovis & Pepe 2007). The DRS deals with all the aspects of the scientific reduction of the raw data, as well as the processing of these reduced data to extract the radial velocities. It reduces the data using the classical optimal extraction method by Horne (1986) including bias and background subtraction and flat field and delivers cosmic ray corrected, and wavelength calibrated spectra. Furthermore, it calculates RVs using the cross correlation function (CCF) method (e.g. Baranne et al. 1996; Pepe et al. 2002). The CCF is fitted by the pipeline with a Gaussian function and the peak is the desired RV value. But there is a further approach to derive the RVs, namely the Java-based Template-Enhanced Radial velocity Re-analysis Application (TERRA, Anglada-Escudé & Butler 2012). It has been demonstrated by Perger et al. (2017) that HARPS-TERRA radial velocities show less scatter than those computed by the DRS and seem to extract RVs with better accuracy and less affected by stellar magnetic activity. For each order TERRA corrects for the blaze function variability and in a first run does a least-squares fit with each spectrum and the spectrum of highest S/N of each target. With this information, a co-added template including all RV corrected input spectra of very high S/N is calculated. This is used as reference in a second run of least-squares fitting to find the final RVs. It can be supposed that smaller observed RV rms correspond to the smaller RV noise rms making TERRA the best option in the calculation of RVs.

2.2.2 GIANO-A spectra

In the course of this thesis, I had the need to analyse GIANO-A data. This was one of the first attempt to use GIANO-A observations for scientific purpose, in particular to derive radial velocity. For this reason during the analysis new reduction procedures were analysed and adopted. This work has been conducted in strict collaboration with the GIANO team.

Note that GIANO-A was the original configuration of GIANO spectrograph located in Nasmyth-A focus. In that configuration, GIANO-A was fiber fed and has not yet been devel-

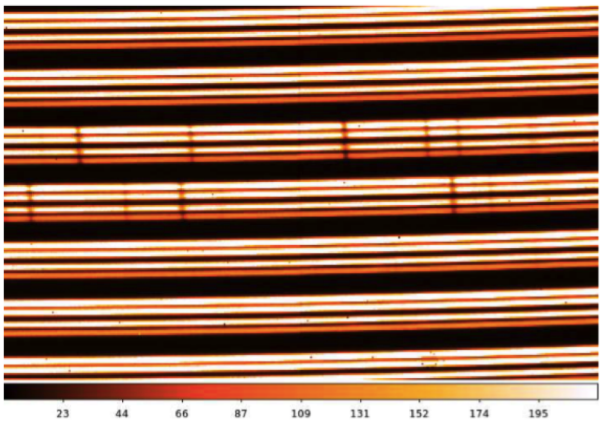

Figure 2.4: Zoom-in on a GIANO image of a continuum lamp. Note that each order is split in four parallel tracks due to the insertion of an image slider that divides the image of the two fibers.

oped a pipeline to reduce the spectra automatically. This constrained us to reduce manually the data taken in the early periods. Actually, with the new configuration (GIANO-B) in Nasmyth-B focus and common feeding with HARPS-N, it has been possible the development of an automatic pipeline called GOFIO (Reiners et al. in preparation).

To extract and wavelength-calibrate the GIANO-A spectra, we have used the ECHELLE package in IRAF and some new, ad-hoc scripts that have been grouped in a package named GIANO TOOLS [I]. The GIANO data reduction manual [II] with a detailed description is available on the TNG website.

A typical 2D output from a GIANO integration with the original fibers configuration, is shown in Fig. 2.4. The whole frame contains 49 groups of 4 arc-shaped tracks where each group represents a spectral order. Any group is composed of two pairs of arcs, each pair corresponding to the output of one of the two optical fibres used to transfer the signal from the telescope focal plane to the spectrograph. Within each order, wavelength increases from right to left. In addition, wavelength decreases with increasing order. One of the goals of the reduction procedure is to find the curve that best fits the signal peak in each sub-track and to count the signal as a function of position within apertures centred on these curves (called traces). In order to obtain an accurate extraction we need a set of calibration frames (dark frames, flat-field frames and reference lamp spectra) and follow the following steps:

- Dark and frame subtraction

[I] Available on `http://www.tng.iac.es/instruments/giano/`

[II] `http://www.bo.astro.it/giano/documents/handbook_giano_v1.2.0.pdf`

Dark subtraction is only needed by flat-fields and lamp reference spectra. The dark frames to subtract, must have been taken with the same integration time as the image to be corrected. We have to combine all the darks with the same integration time and then subtract the final image from all the calibration files (flats and UNe).

It is important to remember that the images taken in cycle AB do not need the dark subtraction but it is necessary to remove any residual scattered and diffuse light contribution. For these reasons we subtract frame B from frame A for every target taken in cycle AB and the resulting 2D spectra will exhibit the target signal in all sub-tracks and have most of the bias removed. If there are more than one subtracted AB pair of frames from the same target we have to combine them together before extracting the spectra.

Then, it is necessary to apply bad-pixel corrections to all flat-field frames, calibration-lamp frames and A-B frames. The correction can be done by using the GIANO TOOLS task called CLEAN-UP.

- Flat-field correction

  The spectrograph efficiency varies with the spectral order and produce differences in peak counts between the four tracks of each order due to the different efficiencies of the two fibres and the positioning of the source in the fibre.

  CCDs and NIR detectors exhibit pixel-to-pixel variations in their quantum efficiency. These need being corrected in order to increase the signal-to-noise ratio. The issue is more complicated for images of echelle spectra, due to the large fraction of the detector area (between orders) exposed to a very low flux. To avoid various degrading effects on the noise statistics, flat-field corrections should only be made inside each aperture.

  There are two possibles ways of flat-field spectra correction:

  – Construct a 2D flat-field map by deriving a flat-field correction only inside the apertures and divide each frame by this map.
  – Extract the 1D spectrum from each aperture of the flat-field image, normalise it, and divide all extracted (1D) unflatted spectra by the corresponding normalised flat-field 1D spectra.

  Here, we describe the 2D technique because making a 2D flat-field frame allows us

to define the traces for all orders and check that the subsequent spectrum extraction works. Both methods are equivalent and the same results are obtained.

First of all, we have to combine together all flat-field frames to enhance the signal-to-noise ratio. This is the image we will use to construct the 2D flat-field map and also to find and fit the traces.

- Find traces

  Following the previous step a final average flat-field image that has the highest signal-to-noise ratio is obtained. Then we fit polynomials to the signal tracks because these polynomials define the traces associated to each track.

  An intermediate step is necessary in order to remove the scattered component because a high level of scattered light can drive small spurious peaks between the central orders exhibiting more counts than the peaks at the highest order. Using the task GIANO FIND TRACE it is possible to construct the scattered light map necessary as a reference file when we will determine the traces (Fig. 2.5).

- Fit traces and construct a 2D flat-field frame

  It is necessary to derive a polynomial curve fitting (Right panel of Fig. 2.6) to the

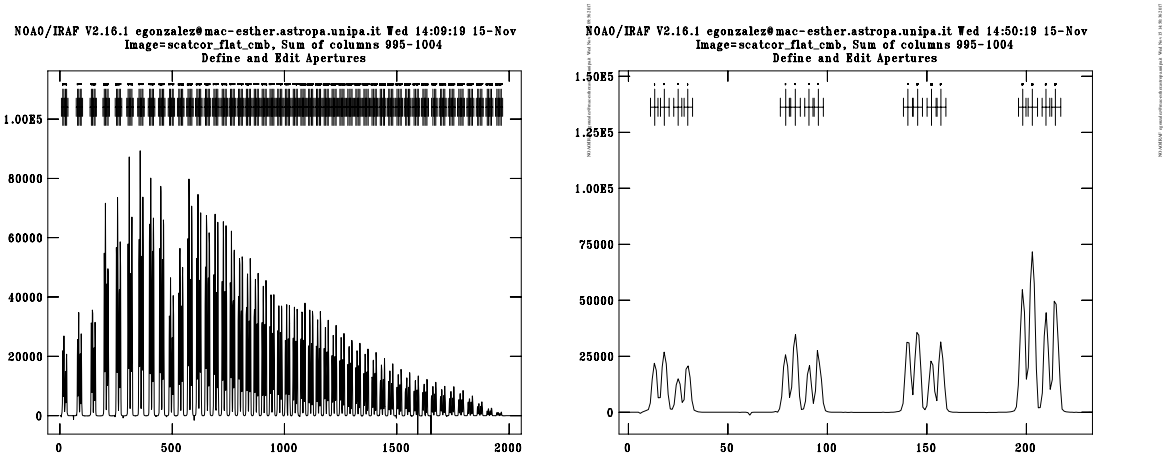

Figure 2.5: Graphic window showing the apertures found. Each peak represents a sub-track, each group of four sub-tracks represents a spectral order. The numbered segments on top of the panel mark the selected apertures and must always correspond to the peaks. *Left panel:* Graphic window showing all apertures found. *Right panel:* After zoom in.

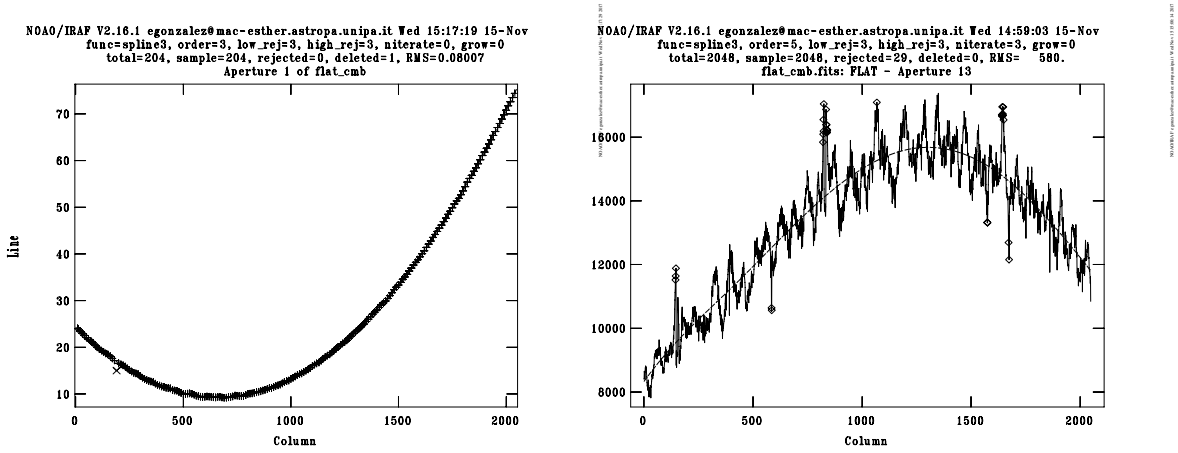

Figure 2.6: Graphic window showing the typical trace fit and the polynomial fit. *Left panel:* Typical trace fit. *Right panel:* Polynomial fit to aperture n. 13.

corresponding signal across the detector by using APFLATTEN. It determine the traces that will be used to extract the spectra from any frame.

This IRAF task allows us to check the trace fit (Left panel of Fig. 2.6) and spectrum fit when we follow the procedure and it gives a final image corresponding with a normalised flat frame.

Then we have to correct all the images (lamp spectra and science frame) dividing (pixel by pixel) each frame by the normalised flat.

- Cloning frame

  There are 196 traces and 49 orders on the detection (four traces for each order). In fact, for each order there is a bottom trace, a mid-lower one, a mid-upper one and a topmost one. Each trace must be extracted and calibrated independently to obtain four 1D for each detection. For this reason we need to make four copies of each detection. The task to use is *copyfile* of GIANO TOOLS. We do the same for the lamp, obtaining four sets of frames for the four different traces.

- Spectrum extraction

  The task used for extracting spectra is DOECSLIT. However, we first need to run APEDIT in order to associate the traces already found in the flat-field frame to science frame through GIANO FIND TRACE and APFLATTEN.

Before running APEDIT, we have to split the traces found and re-arrange them in the correct order. To this purpose, we use the GIANO TOOLS task SPLIT FILE operating on the non normalised flat-field frame. The output of this task are four sets of frames for the flat (lower, middown, midup and topmost).

The next step is to run APEDIT and check that the aperture locations have been set correctly for each frame. We must run APEDIT for all the four track group (lowest, middown, midup and topmost), so that every frame will have its trace set associated.

The next step is DOECSLIT to extract and wavelength calibrate the 1D spectra. This task also has to be done four times, for the four groups of frames. The output file is the extracted spectra in 1D.

- Combining the extracted 1D spectra together

  At this point, we have four different 1D spectra for each target. It is necessary to combine them together to increase the S/N (Fig. 2.7). The output of each fibre is split into two spots, both feeding the slit. This means that the exposure time is exactly that of the single A or B frame after summing together the pair of 1D spectra corresponding to the same fibre. Consequently, if we add together all four 1D spectra extracted from an AB subtracted frame, the effective exposure time will be twice that of the single A or B frame. If you average together the four 1D spectra, the exposure time will be half that of the single A or B frame.

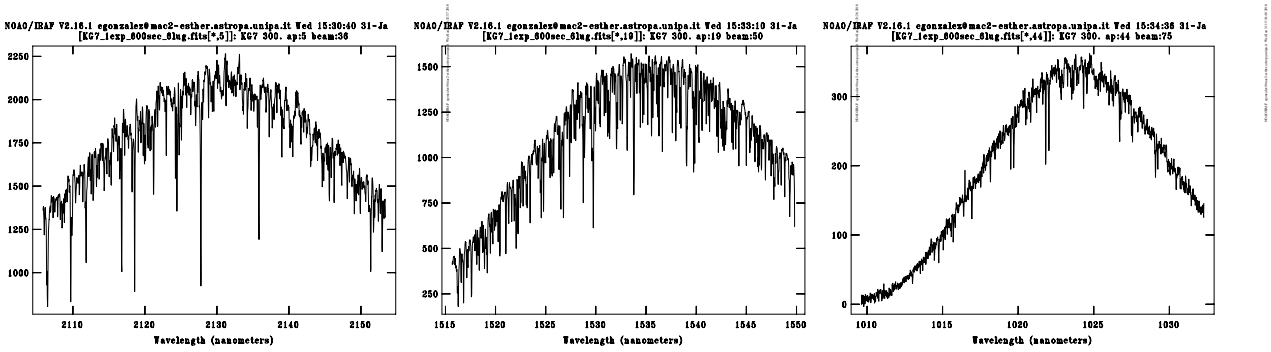

Figure 2.7: Combined 1D final spectra extracted. *Left panel:* Low spectral orders. *Middle panel:* Central spectral orders. *Right panel:* High spectral orders.

Chapter 3

Activity indexes

3.1 Introduction

Understanding the stellar activity is crucial to correctly interpret the physics of stellar atmospheres and the ongoing radial velocity exoplanet programmes. In particular, stellar activity distorts line profiles modifying the radial velocity curves and therefore affects our capability to detect small planets. This is specially critical for M dwarfs as they show high stellar activity levels due to their deep convective layers. Therefore we need to analyse very carefully the activity properties of these targets.

It is well known that for FGK stars activity and rotation are linked by the stellar dynamo and both diminish as the star ages (e.g. Strassmeier et al. 1990; Robinson et al. 1990; Stelzer et al. 2012). Despite the increasing interest in M dwarfs, the knowledge of the chromosphere of these stars is still very far from being fully understood, even if some studies suggest that the connection between age, rotation, and activity may also hold in early M dwarfs (e.g. Delfosse et al. 1998; Pizzolato et al. 2003).

This chapter aims to test whether the relations between activity, rotation and stellar parameters and flux-flux relationships investigated in literature for main-sequence FGK stars and for pre-main-sequence M stars also hold for early-M dwarfs on the main-sequence. Part of the content of this chapter is included in Maldonado et al. (2017), Scandariato et al. (2017) and Suárez Mascareño et al. (A&A, in press).

We analyse our sample of 78 late-K/early-M dwarfs where the stellar parameters (effective temperature, spectral type, surface gravity, iron abundance, mass, radius and luminosity) were computed using a methodology based on ratios of spectral features (Maldonado et al.

2015a). Projected rotational velocities $v \sin i$ have been computed using the cross-correlation technique (CCF). The full details on this technique can be found in e.g. Melo et al. (2001) and Martínez-Arnáiz et al. (2010).

3.2 Coronal activity

Traditionally the most frequently investigated diagnostics of chromospheric activity are the Ca II H & K or the Balmer lines measured from optical spectra. In order to measure also a stellar activity diagnostic independent of the spectra, we decided to investigate the coronal activity indicator X-ray luminosity (L_x). L_x is emitted from the upper atmosphere and can be easily determined for nearby M stars.

With the purpose of study the coronal activity, we collected the information for our sample of M dwarfs (described in detail in Section 1.4) from the main X-ray missions, ROSAT (e.g. Truemper 1992; Voges et al. 1999) and XMM-Newton. Even if ROSAT is older and less sensitive than the most recent X-ray observatories, it is still the main source of X-ray measurements since it covered all the sky. In particular, we consult the ROSAT Bright and Faint Source catalogues (BSC and FSC: Voges et al. 1999), the second ROSAT All-Sky Survey Point Source Catalog (2RXS: Boller et al. 2016), the third ROSAT Catalogue of Nearby Stars (CNS3: Hünsch et al. 1999), the XMM-Newton XAssist source list (XAssist: Ptak & Griffiths 2003), the XMM-Newton Slew Survey Full Source Catalog, v2.0 (XMM-SLEW: Saxton et al. 2008) and the Third XMM-Newton Serendipitous Source Catalogue (3XMM-DR7: Rosen et al. 2016).

For ROSAT detected sources, we need to apply a count-to-flux conversion factor (CF) because the X-ray emission is expressed by count rates (CRT) and hardness ratio (HR) quantities. The HR is defined through $HR = \frac{H-S}{H+S}$, denoting by H and S the counts recorded in the soft (0.1-0.4 keV) and hard (0.5-2.0 keV) PSPC channels. In order to obtain the X-ray flux (f_x) from the Position Sensitive Proportional Counters (PSPC) detector, it is possible to derive the CF (Schmitt et al. 1995) appropriate for a coronal spectral model with a given HR as:

$$CF = (8.31 + 5.30 \cdot HR) \times 10^{-12} \text{ [erg cm}^{-2} \text{ count}^{-1}] \tag{3.2.1}$$

The CF depends on the given spectral model and on the instrument, the details on this conversion procedure are given by Fleming et al. (1995). For the cases with no HR in the

data it is assumed a HR value of -0.4, corresponding to a middle activity level star ϵ Eri (Schmitt et al. 1995; Huensch et al. 1998; Sanz-Forcada et al. 2011) and then used a fixed CF value of 6.19×10^{-12} erg cm^{-2} count^{-1}. Combining the X-ray count rate with the conversion factor, the X-ray flux can be estimated as

$$f_x = CF \cdot CRT \text{ [erg cm}^{-2} \text{ s}^{-1}] \tag{3.2.2}$$

where the flux observed error is basically due to signal-to-noise ($S/N = \frac{eCRT}{CRT}$):

$$ef_x = \frac{eCRT}{CRT} f_x \tag{3.2.3}$$

For the case of XMM-Newton detected sources, the different XMM-Newton catalogues used provide directly the X-ray flux values calculated from count rates based on energy conversion factors assuming a spectral model of an absorbed power-law (see XMM Science Survey Center memo SSC-LUX TN-0059 for a general description of the technique).

Using the distance of the stars d from Lépine & Gaidos (2011) and Gaia (Gaia Collaboration et al. 2016), the X-ray luminosity is determined by

$$L_x = f_x 4\pi d^2 \ \ [erg\, s^{-1}] \tag{3.2.4}$$

where the absorption due to the interstellar material can be neglected due to the closeness of our stars. Table 3.1 presents the 37 out of 78 stars with X-ray information collected for our M dwarfs sample. The total uncertainties on the derived luminosities are calculated by error propagation while empty fields correspond to missing values. Also in Table 3.1 are presented the $L_x/L_{\rm bol}$ values of each star, a usual approach to compensate for the different stellar sizes. The luminosity of the stars ($L_\star$ or $L_{\rm bol}$) was calculated following the Stefan-Boltzmann law:

$$L_\star = 4\pi R_\star^2 \sigma_B T_{\rm eff}^4 \ \ [erg\, s^{-1}] \tag{3.2.5}$$

where σ_B is the Stefan-Boltzmann constant ($5.6704 \cdot 10^{-5}$ erg cm^{-2} s^{-1} K^{-4}). The $R_\star$ and $T_{\rm eff}$ correspond with the radius and effective temperature of the star, respectively and were computed using a methodology based on ratios of spectral features described in Maldonado et al. (2015b). The corresponding stellar parameters for our M dwarfs sample were published in Maldonado et al. (2017).

Table 3.1: Stars with derived X-ray emission.

Name	d [pc]	$\log L_x$ [erg s^{-1}]	$\log L_x/L_{\rm bol}$
G243-30 *	12.48 ± 0.22	28.87 ± 0.13	-3.16 ± 0.43
GJ15A	3.58 ± 0.01	27.29 ± 0.05	-4.64 ± 0.12
GJ2	11.24 ± 0.17	27.56 ± 0.13	-4.63 ± 0.16
GJ2128	14.90 ± 0.59	27.60 ± 0.18	-4.20 ± 0.24
GJ26	12.48 ± 2.49	27.18 ± 0.17	-4.66 ± 0.23
GJ272	16.42 ± 0.51	27.38 ± 0.21	-4.71 ± 0.23
GJ3014	19.60 ± 0.69	27.95 ± 0.11	-4.20 ± 0.15
GJ3117A	17.36 ± 0.12^a	27.23 ± 0.19	-4.78 ± 0.21
GJ3822	19.84 ± 0.78	27.76 ± 0.19	-4.59 ± 0.22
GJ3942	16.92 ± 0.28	27.68 ± 0.17	-4.66 ± 0.20
GJ408	6.66 ± 0.07	26.93 ± 0.21	-4.86 ± 0.26
GJ412A *	4.85 ± 0.02	26.63 ± 0.03	-5.31 ± 0.12
GJ414B	12.04 ± 2.40	27.52 ± 0.23	-4.65 ± 0.24
GJ450	8.58 ± 0.08	27.65 ± 0.12	-4.44 ± 0.16
GJ47	11.00 ± 2.20	27.27 ± 0.22	-4.59 ± 0.27
GJ476 *	18.28 ± 1.00	$27.05 \pm -$	$-4.82 \pm -$
GJ49 *	9.96 ± 0.15	27.58 ± 0.02	-4.69 ± 0.08
GJ548A	16.36 ± 0.37	28.04 ± 0.11	-4.43 ± 0.15
GJ552	14.00 ± 0.41	27.58 ± 0.19	-4.50 ± 0.21
GJ606	13.88 ± 0.36	27.72 ± 0.16	-4.37 ± 0.19
GJ625	6.51 ± 0.04	26.87 ± 0.03	-4.99 ± 0.24
GJ685	14.10 ± 0.19	27.45 ± 0.07	-4.87 ± 0.12
GJ694.2	21.49 ± 0.50	27.48 ± 0.19	-4.70 ± 0.21
GJ70	11.41 ± 0.26	27.41 ± 0.03	-4.46 ± 0.14
GJ720A	15.55 ± 0.24	27.39 ± 0.15	-5.11 ± 0.18
GJ740	10.90 ± 0.17	27.51 ± 0.14	-4.85 ± 0.17
GJ793	7.993 ± 0.07	27.77 ± 0.03	-3.99 ± 0.18
GJ835	13.31 ± 0.33	27.97 ± 0.12	-4.27 ± 0.43

Table 3.1: Stars with derived X-ray emission. (continue)

Name	d [pc]	$\log L_x$ [erg s^{-1}]	$\log L_x/L_{\rm bol}$
GJ895	12.95 ± 0.21	27.20 ± 0.21	-5.07 ± 0.23
GJ908 *	5.97 ± 0.04	27.15 ± 0.08	-5.09 ± 0.20
GJ9440 *	16.97 ± 0.43	27.04 ± 0.12	-5.17 ± 0.15
GJ9793	36.36 ± 2.90	28.80 ± 0.18	-3.82 ± 0.24
NLTT51676 *	20.92 ± 1.09	29.29 ± 0.22	-3.09 ± 0.43
NLTT53166	22.72 ± 1.13	28.58 ± 0.08	-3.80 ± 0.12
TYC2703-706-1 *	36.75 ± 0.47^a	29.97 ± 0.12	-2.48 ± 0.15
TYC2710-691-1	45.60 ± 1.23^a	28.89 ± 0.12	-3.61 ± 0.15
TYC3720-426-1	35.21 ± 2.72	29.18 ± 0.08	-3.29 ± 0.17

* Stars with X-ray data from XMM-Newton. For the rest of stars data comes from the ROSAT catalogues.

[a] Distance, d, comes from Gaia. The rest comes from Lépine & Gaidos (2011)

3.2.1 Comparison with the nearby stellar population

In order to test whether our M dwarf sample is representative of the solar neighbourhood we compare its X-ray properties with a large sample of nearby M stars. The comparison sample is taken from the NEXXUS database (Schmitt & Liefke 2004) where only M dwarfs between M0 to M4.5 spectral types were selected (the same SpT range of our sample). NEXXUS is a catalogue of all known stars within a distance of 25 pc to the Sun that are identified as X-ray and/or extreme UV sources from Einstein, EUVE, ROSAT, and XMM-Newton data, based on positional coincidence. Figure 3.1 shows the cumulative distribution functions of $\log L_x$ for the NEXXUS M dwarfs and for our sample. The comparison shows a clear tendency of our sample to show higher levels of activity in X-ray emission with a L_x median value about twice the median value of the nearby population. A Kolmogorov-Smirnov (K-S) test shows the significant difference between the two samples with a K-S statistic value D=0.49 and p-value=6.13×10^{-6}. Therefore we are studying the regime of moderately active M dwarfs and our research for exoplanets may be compromised by the presence of stellar activity. This

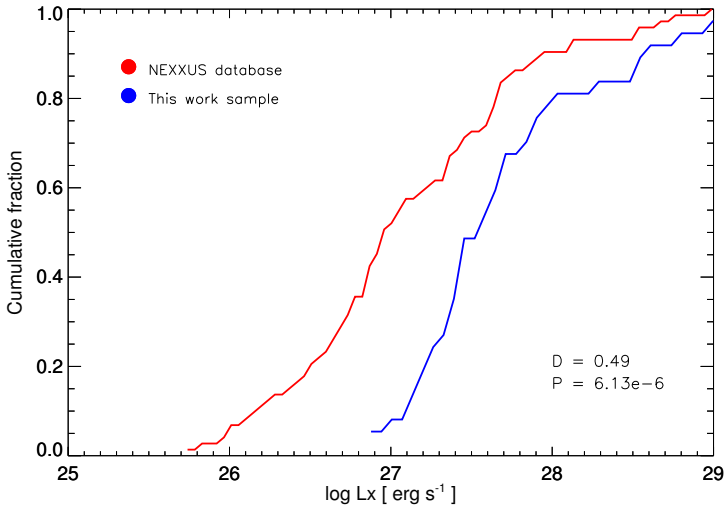

Figure 3.1: Cumulative distribution function of $\log L_x$. The red and blue lines correspond with the NEXXUS M dwarfs and this work sample, respectively.

motivated us to carefully study the activity of our stars.

3.2.2 X-ray emission dependence on stellar parameters

Here we analyse the coronal X-ray emission as a function of the stellar parameters. We adopt the usual approach to parametrize the X-ray information with X-ray luminosity to bolometric luminosity ratio (L_x/L_{Bol}) or X-ray surface flux to bolometric flux ratio (F_x/F_{Bol}) in order to directly compare stars with different bolometric luminosity.

The value of X-ray flux, f_x, obtained previously is the observed X-ray flux. This is transformed in the surface flux, F_x, by applying the scaling factor $(\frac{d}{R_*})^2$, and transformed into luminosity using the individual distance by $L_x = 4\pi d^2 f_x$.

$$\frac{L_x}{L_{Bol}} = \frac{4\pi d^2 f_x}{4\pi R_*^2 \sigma T_{eff}^4} = \frac{F_x}{F_{Bol}} \tag{3.2.6}$$

where R_* is the radius of the star, d the distance, $T_{\rm eff}$ the effective temperature and σ the Boltzmann's constant. Interstellar abortion can be neglected.

Left panel of Figure 3.2 shows $\log F_x$ as a function of the projected rotational velocity. For low $v \sin i$ values (< 2 km s^{-1}), the scatter in X-ray values is large. The stars with the highest $v \sin i$ also show the largest X-ray emission. The statistical analysis of the data

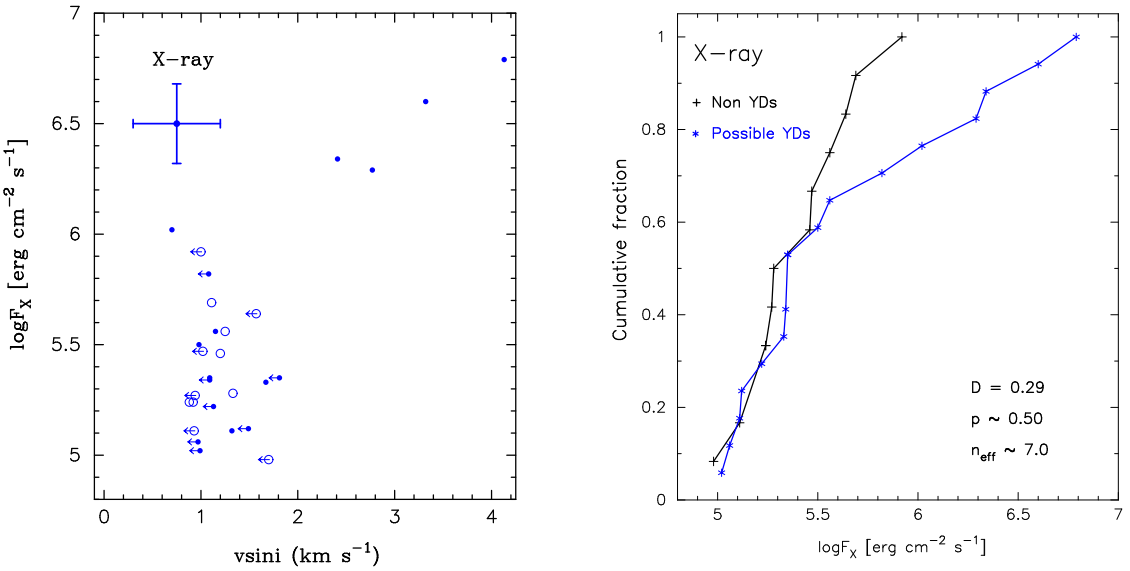

Figure 3.2: X-ray emission as a function of the stellar parameters. *Left panel:* X-ray flux vs. vsin i. Typical error bars are given in the top left corner. Upper limits are shown as arrows. Possible young stars according to their kinematics are shown with filled symbols. *Right panel:* Cumulative distribution function of $\log F_x$ for possible young (blue line) and old (black line) disc stars.

shows that the probability that X-ray fluxes and $v \sin i$ are correlated by chance is relatively low ($\sim$ 1-2 %) with a Spearman correlation coefficient of the order of 0.40.

Stellar age is one of the most difficult parameters to measure accurately. However, if the star is a member of a stellar kinematic group or a young star association it is possible obtain an age estimate. According to Reiners et al. (2012) it seems that most of the active early-M dwarfs may belong to young associations. However, many old stars can share the spatial motion of young stars belonging to kinematics groups so kinematic criteria alone are not sufficient to determine the stellar age. A combination of kinematics, spectroscopic signatures (e.g. rotation, activity) and the location of the stars in color-magnitude diagrams are usually used to assess the likelihood of membership of a star to young kinematic groups (e.g. Montes et al. 2001; Maldonado et al. 2010). However, the criterion is based on statical properties, and we are aware of the limitations of this age-dating procedure.

With this limitation in mind, in order to test whether young M dwarfs show higher levels of X-ray emission, our stars were classified into young and old based on their kinematics (Fig. 3.2 right panel). A Kolmogoróv-Smirnov (K-S) test, used to compare whether two samples come from the same parent distribution, shows no significant difference between the two samples with a K-S statistic value $D \sim 0.29$ and a p-value of $p \sim 0.50$. Nevertheless the

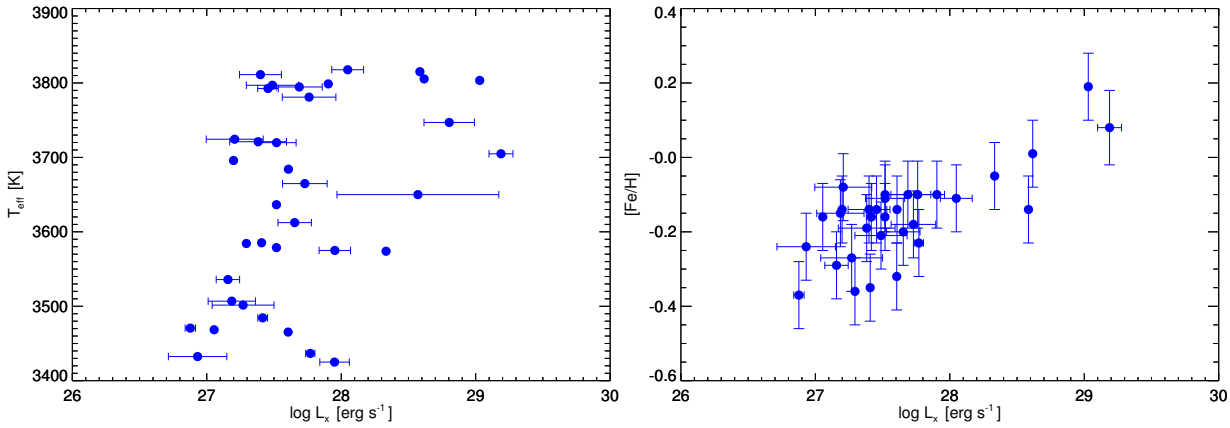

Figure 3.3: $T_{\rm eff}$ and [Fe/H] versus the X-ray luminosity.

figure reveals that while the $\log F_x$ distribution of young and old stars seems to be identical for values of X-ray emission $\log F_x < 5.5$ erg cm^{-2} s^{-1}, at larger values young stars tend to show larger X-ray emission than old stars.

We finally study the dependence of X-ray luminosity on the effective temperature and the metallicity. Left panel of Fig. 3.3 shows that the luminosity drops for stars cooler than $T_{\rm eff} = 3600$ K (spectral type M1), analoughously to the result found by Scandariato et al. (2017) using the flux excess for Ca II H & K lines for our sample of M dwarfs.

The dependence on the stellar metallicity is presented in right panel of Fig. 3.3 showing that more metallic stars tend to have larger values of L_x. The same result obtained in Scandariato et al. (2017) when Ca II H & K lines are studied.

The reason for such metallicity dependence can be due to an age effect, because stars with younger age have on average higher metallicities, consistent with the fact that the activity of the star is related with the age. Younger stars (on average more metal rich) tend to be more active. Another effect could be the enhanced opacity due to the presence of metals that may make more efficient the convection, and then the dynamo process.

3.2.3 Rotation period - activity relationship

Stellar activity has became the biggest obstacle to find small planets when radial velocity measurements are used inducing apparent Doppler shifts. When these induced signals are periodic, they not only introduce noise, but also coherent signals that can mimic those of

planetary origin (Queloz et al. 2001; Robertson et al. 2014).

Magnetic activity in late-type main-sequence stars is an observable manifestation of the stellar magnetic fields. The generation of surface magnetic fields in solar-like stars are considered the end result of a complex dynamo mechanism, whose efficiency depends on the interaction between differential rotation and convection inside the star (Kosovichev et al. 2013). So, stellar rotation must play a very important role and numerous studies have searched for relations between several chromospheric and coronal magnetic activity indicators and stellar rotation rate (e.g. Pallavicini et al. 1981; Maggio et al. 1987; Randich et al. 1996; Pizzolato et al. 2003; Wright et al. 2011; Newton et al. 2017). In a feedback mechanism, magnetic fields are responsible for the spin-evolution of the star (Matt et al. 2015), and therefore rotation and magnetic fields are intimately linked and play a fundamental role in stellar evolution. Early works have used spectroscopic measurements as a measure of stellar rotation ($v \sin i$) with intrinsic ambiguities related to unknown inclination angle of the stars (Pallavicini et al. 1981). Stellar rotation rates are best derived from the periodic brightness variations induced by cool star-spots (photometrically measured) which can be directly associated with the rotation period which has been proven more useful than $v \sin i$ (Pizzolato et al. 2003; Wright et al. 2011).

Theory predicts a qualitative change of the dynamo mechanism at the transition into the fully convective regime (spectral type (SpT) $\sim$ M4, Stassun et al. 2011). This makes studies of the rotation dependence of magnetic activity across the M spectral range crucial for understanding fully convective dynamos. Rotation-activity studies have been presented with different diagnostics for activity, Hα and X-ray emission. X-ray emission was shown to be more sensitive to low activity levels in M dwarfs (Stelzer et al. 2013b). On the other hand, studies with optical emission lines (Hα, Ca II H & K) as activity indicators have been mostly coupled with $v \sin i$ as a rotation measure because both parameters can be obtained from the same set of spectra (Browning et al. 2010; Reiners et al. 2012). The combination of Hα data with photometrically measured M star rotation periods has been studied by West et al. (2015).

We now study the dependence of X-ray emission on the stellar rotation period in early M type main-sequence stars. We extend, for the first time, the up to now available sample of dM stars to the non-saturated X-ray emission regime with respect to previous studies (e.g. Pizzolato et al. 2003; Stelzer et al. 2016; Wright et al. 2011).

In order to study the M star rotation-activity connection, we used the X-ray data collected in Sect. 3.2. Rotation periods were determined in the framework of the HADES collaboration

(section 1.4) by analysing time-series high-resolution spectroscopy of the Ca II H & K lines and Hα activity indicators (Suárez Mascareño et al. A&A, in press). These authors studied a fraction of our original M dwarf sample, composed of 72 stars (out of a total of 78) providing 33 rotation period measured from the spectra as well as 34 periods derived from the Ca II H & K - rotational period relationship. The distribution of rotation periods is shown in Fig. 3.4. It can be seen that our $P_{\rm rot}$ values cover the range between 8 and 85 days. As explained in Sect. 3.2 a total of 37 M dwarfs of our sample have an X-ray counterpart. Finally, by merging the information collected in X-ray emission with $P_{\rm rot}$, our sample for the study of the rotation-activity relationship is reduced to 33 stars with both measurements. The final sample is given in Table 3.2 (measured $P_{\rm rot}$) and Table 3.3 (derived $P_{\rm rot}$).

In previous works (Pizzolato et al. 2003; Stelzer et al. 2016) the dependence between magnetic activity and rotation for dM stars remained poorly constrained, specially in the non-saturated regime (slow rotators). Therefore the turn-over point between the saturated and non-saturated regimes and the slope of the decaying part of the relation was not well constrained. Stelzer et al. (2016) studied a sample of 134 bright, nearby M dwarfs (SpT K7-M6), where only a total of 26 stars had X-ray measurements in the archival data bases that they consulted. These 26 stars were divided into three SpT groups (K7-M2, M3-M4 and M5-M6).

Pizzolato et al. (2003) studied a sample of 259 solar-type dwarfs in the $B-V$ range 0.5-2.0, all of them with X-ray counterpart. The sample was divided as a function of the stellar mass (8 groups from 0.22-1.29 $M_{\odot}$ range) in order to investigate how the observed spread of X-ray emission levels depends on the stellar mass and to determine the best-fit

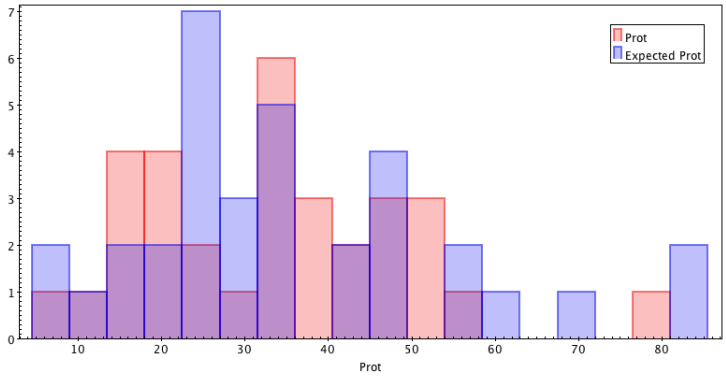

Figure 3.4: Distribution of the rotation periods for the stars in our sample. The red area shows the measured rotation periods and the blue area corresponds to the derived rotation periods when a direct determination was not possible.

relations between X-ray emission and rotation period for each mass bin.

Our sample of M dwarfs include stellar masses from 0.16 to 0.7 $M_{\odot}$ (SpT K7-M4) comparable with M dwarfs samples of previous studies. In Fig. 3.5 we present an update of the activity-rotation relation of dM stars using the X-ray data extracted from archives and the rotation periods by Suárez Mascareño et al. (A&A, in press) for our M dwarfs sample, including the derived rotation periods. We also indicate the relation derived by Pizzolato et al. (2003) and their sample for their lowest mass bin, M = 0.22-0.60 $M_{\odot}$. It must be noted, that this derived relation in the saturated regime is dominated by $P_{\rm rot}$ values estimated from $v \sin i$ measurements (therefore only upper limits values for $P_{\rm rot}$) and only two stars are present in the non-saturated regime. Most of our data fill the slow rotation area of low-mass stars covering the regime poorly populated in previous studies.

It can be seen in Fig. 3.5 (left panel) a spread of our data around the best-fit relation estimated by Pizzolato et al. (2003). This spread is more evident in the right panel of Fig. 3.5 where L_x/L_{bol} is reported. It could be due to two possible reasons: i) the mass range studied by Pizzolato et al. (2003) (M = 0.22-0.60 $M_{\odot}$) is too large and it should be divided in subgroups that follow a tighter relation; ii) the derived rotational periods are too uncertain and their inclusion produce a large spread. We, therefore, excluded from our analysis the derived P_{rot} values (i.e, those derived from calcium measurements using a Ca II H & K -

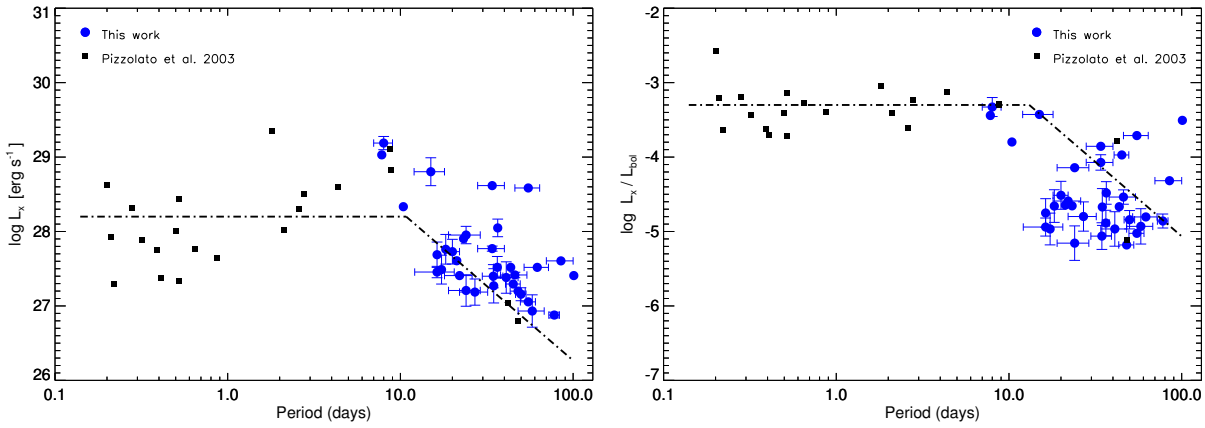

Figure 3.5: L_x (Left panel) and L_x/L_{bol} (right panel) versus rotation period. The black squares correspond to the stellar sample from Pizzolato et al. (2003) in the mass range $0.22 < M/M_{\odot} < 0.60$. The blue large dots correspond to the M dwarfs studied in this work. The black dashed line represents the broken power law obtained by the fitting procedure from Pizzolato et al. (2003) with $P_{\rm rot}$ values estimated from $v \sin i$ in saturated regime.

$P_{\rm rot}$ relationship) and divided our sample into two $T_{\rm eff}$ groups: 3400-3600 K and 3700-3800 K (corresponding to mass range $M = 0.16 - 0.6\ M_{\odot}$ and $M = 0.58 - 0.7\ M_{\odot}$, respectively). This leaves us with a total of 19 M dwarfs in our sample, 11 stars in the 3400-3600 K range and 8 in the 3700-3800 K range.

Table 3.2: Stars with X-ray activity level and measured rotation periods. Rotation values are from Suárez Mascareño et al. (A&A, in press) while L_x values are computed in this work.

Name	SpT*	$T_{\rm eff}$ (K)	$\log L_x$ (erg s^{-1})	$\log L_x/L_{bol}$	P_{rot} (days)
TYC2703-706-1	0.0	3803.41 ± 69.62	29.97 ± 0.12	-2.48 ± 0.15	7.8 ± 0.2
GJ3942	0.0	3794.66 ± 68.4	27.68 ± 0.17	-4.66 ± 0.20	16.3 ± 0.1
GJ685	0.0	3792.59 ± 68.87	27.45 ± 0.07	-4.87 ± 0.12	16.3 ± 4.2
GJ720A	0.0	3811.18 ± 69.3	27.39 ± 0.15	-5.11 ± 0.18	34.5 ± 4.7
GJ412A	0.0	3585.32 ± 67.79	27.63 ± 0.03	-5.31 ± 0.12	100.9 ± 0.3
GJ694.2	0.0	3796.94 ± 69.04	27.48 ± 0.19	-4.70 ± 0.21	17.3 ± 0.1
GJ548A	0.0	3817.76 ± 69.32	28.04 ± 0.11	-4.43 ± 0.15	36.6 ± 0.1
GJ740	0.0	3719.8 ± 68.57	27.51 ± 0.14	-4.85 ± 0.17	36.4 ± 1.7
GJ3822	0.0	3781.0 ± 68.89	27.76 ± 0.19	-4.59 ± 0.22	18.3 ± 0.1
GJ2	1.5	3684.12 ± 68.13	27.56 ± 0.13	-4.63 ± 0.16	21.2 ± 0.5
GJ15A	1.5	3584.34 ± 67.71	27.29 ± 0.05	-4.64 ± 0.12	45.0 ± 4.4
GJ49	1.5	3703.56 ± 68.16	27.58 ± 0.02	-4.69 ± 0.08	18.4 ± 0.7
GJ606	1.5	3664.78 ± 68.09	27.72 ± 0.16	-4.37 ± 0.19	20.0 ± 2.0
GJ908	2.0	3535.89 ± 67.68	27.15 ± 0.08	-5.09 ± 0.20	49.9 ± 3.5
GJ625	2.0	3470.64 ± 67.49	26.87 ± 0.03	-4.99 ± 0.24	77.8 ± 5.5
GJ9440	2.0	3695.84 ± 68.28	27.04 ± 0.12	-5.17 ± 0.15	48.0 ± 4.8
GJ47	2.5	3501.58 ± 67.52	27.27 ± 0.22	-4.59 ± 0.27	34.7 ± 0.1
GJ552	2.5	3578.78 ± 67.54	27.58 ± 0.19	-4.50 ± 0.21	43.5 ± 0.1
GJ476	2.5	3468.48 ± 67.55	$27.05 \pm -$	$-4.82 \pm -$	55.0 ± 5.5

* SpT = 0 - 2.5 correspond to M0 - M2.5 spectral types.

Table 3.3: Stars with X-ray activity level and derived rotation periods. Rotation periods are taken from Suárez Mascareño et al. (A&A, in press) and L_x values are computed in this work.

Name	SpT*	$T_{\rm eff}$ (K)	$\log L_x$ (erg s^{-1})	$\log L_x/L_{bol}$	Derived P_{rot} (days)
GJ9793	-1.0	3746.95 ± 68.08	28.80 ± 0.18	-3.82 ± 0.24	15.0 ± 3.0
NLTT53166	-0.5	3815.18 ± 68.93	28.58 ± 0.08	-3.80 ± 0.12	55.0 ± 9.0
TYC3720-426-1	-0.5	3704.84 ± 67.68	29.18 ± 0.08	-3.32 ± 0.12	8.0 ± 1.0
TYC2710-691-1	-0.5	3805.48 ± 69.67	28.89 ± 0.12	-3.61 ± 0.15	34.0 ± 6.0
GJ895	1.5	3724.44 ± 68.18	27.20 ± 0.21	-5.07 ± 0.23	24.0 ± 5.0
GJ3014	1.5	$3575.0 \pm -$	27.95 ± 0.11	-4.20 ± 0.15	24.0 ± 5.0
GJ272	1.5	3721.08 ± 68.46	27.38 ± 0.21	-4.71 ± 0.23	41.0 ± 7.0
GJ414B	2.0	3636.46 ± 67.93	27.52 ± 0.23	-4.65 ± 0.24	62.0 ± 10.0
GJ3117A	2.5	3535.96 ± 67.75	27.23 ± 0.19	-4.78 ± 0.21	22.0 ± 4.0
GJ70	2.5	3484.45 ± 67.83	27.41 ± 0.03	-4.46 ± 0.14	46.0 ± 8.0
GJ26	2.5	3506.85 ± 67.5	27.18 ± 0.17	-4.66 ± 0.26	27.0 ± 5.0
GJ793	2.5	3436.68 ± 67.34	27.77 ± 0.03	-3.99 ± 0.18	34.0 ± 6.0
GJ408	2.5	3432.45 ± 67.45	26.93 ± 0.21	-4.86 ± 0.26	58.0 ± 10.0
GJ2128	2.5	3465.32 ± 67.35	27.60 ± 0.18	-4.20 ± 0.24	85.0 ± 15.0

* SpT = -1 - 2.5 correspond to K7 - M2.5 spectral types.

Fig. 3.6 shows the behaviour of M dwarfs in the non-saturated regime by dividing our stars into two $T_{\rm eff}$ groups plotted with different colours. We have not enough stars to determine here the saturated regime level (fast rotators) because almost all the stars in our sample are placed into the non-saturated regime. We assume the saturation level as described by Pizzolato et al. (2003). In a more recent work and using a larger sample, Stelzer et al. (2016) determine a higher saturation level than the one found by Pizzolato et al. (2003). However, the sample in Stelzer et al. (2016) is taken from *Kepler* Two-Wheel (K2) light curves and it is likely biased towards bright X-ray M dwarfs which can be translated into a higher value of the saturation level.

In order to obtain a new parametrization of the X-ray emission vs. rotation relationship for M dwarfs in the non-saturated regime for the two bins of $T_{\rm eff}$, the data were fitted in each temperature bin with a fixed power law exponent of -2 (as determined by Pizzolato et al.

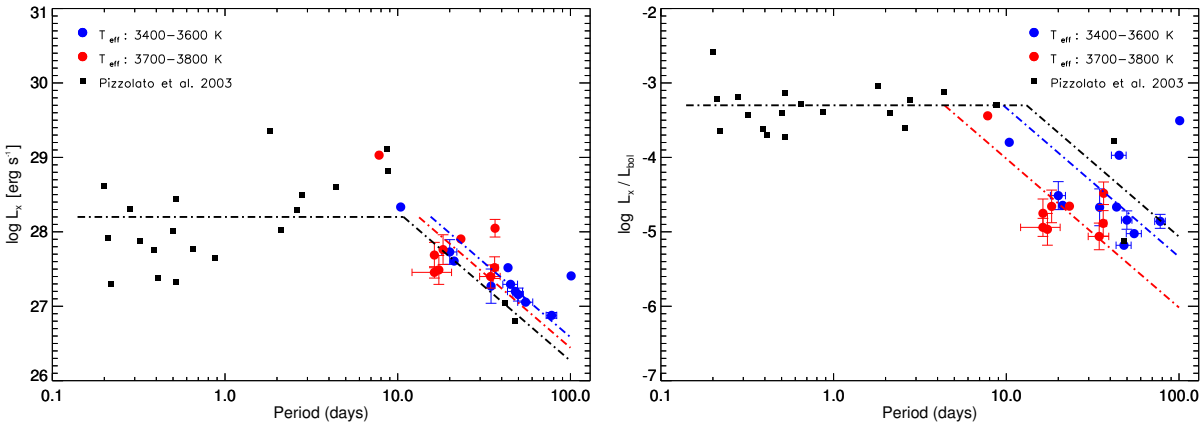

Figure 3.6: L_x (left) and L_x/L_{bol} (right) versus rotation period for stars with direct rotation period determination. The black squares correspond with the stellar sample from Pizzolato et al. (2003) in the mass range $0.22 < M/M_{\odot} < 0.60$. Blue and red dots correspond to the M dwarfs from this work in the two different range of $T_{\rm eff}$ indicated in the legend. The black dashed line represents the broken power law obtained by the fitting procedure from Pizzolato et al. (2003). The blue and red dash line represent our best fit for 3400-3600 K and 3700-3800 K $T_{\rm eff}$ range, respectively.

(2003)) leaving the intercept parameter free to vary. Power-law functions were fitted to the data,

$$\log F_1 = a_0 + a_1 \ \log F_2 \tag{3.2.7}$$

where $\log F_1$ corresponds with the analysed values of $\log L_x$ and $\log L_x/L_{bol}$, F_2 with the P_{rot} and a_0 and a_1 are the fit coefficients. In our case we set the value a_1 fixed to -2 and obtained the best two intercept parameters presented in Table 3.4.

The best-fit relations between L_x and P_{rot} obtained (Fig. 3.6, left panel) are very similar for the two $T_{\rm eff}$ bins. Note the complementary behaviour of the $L_x/L_{\rm bol}$ versus $P_{\rm rot}$ case

Table 3.4: Coefficients of the activity-rotation relationships with slope parameter set to -2.

$T_{\rm eff}$	$\log F_1$	F_2	a_0	χ^2
3400-3600 K	$\log L_x$	$P_{\rm rot}$	30.58 ± 0.09	11.29
	$\log L_x/L_{bol}$	$P_{\rm rot}$	-1.34 ± 0.05	57.68
3700-3800 K	$\log L_x$	P_{rot}	30.44 ± 0.05	15.90
	$\log L_x/L_{bol}$	P_{rot}	-2.02 ± 0.06	13.59

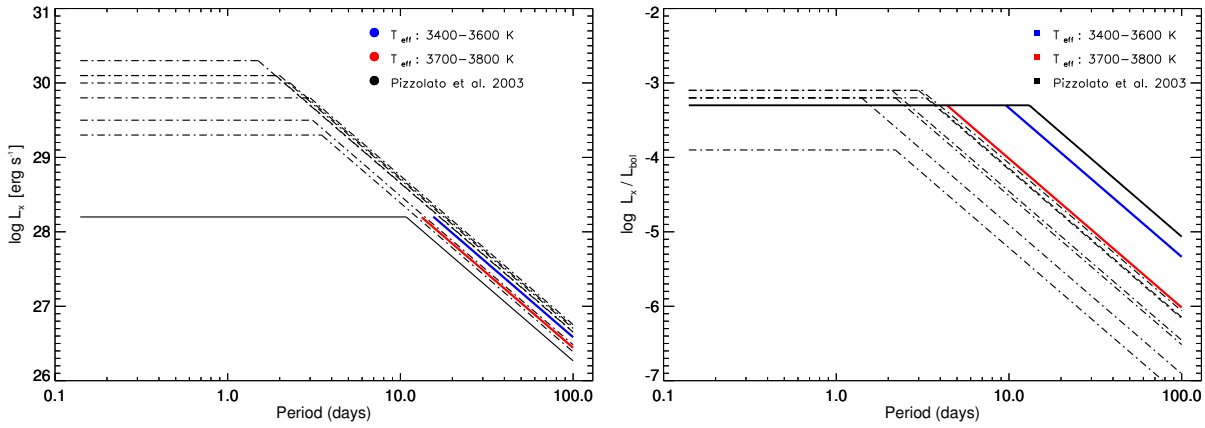

Figure 3.7: All the best-fit relations between X-ray emission and rotational period for all the mass range considered in Pizzolato et al. (2003) are presented with black dash lines. The black line corresponds with the best-fit in $0.22 < M/M_{\odot} < 0.6$ mass range. The blue and red lines represent our best-fit for 3400-3600 and 3700-3800 K $T_{\rm eff}$ range, respectively.

(Fig. 3.6, right panel) where is more evident the different loci occupied by the two $T_{\rm eff}$ bins groups. This behaviour is coherent with that seen in Pizzolato et al. (2003) for more massive stars.

Our work extends to the low mass regime the observed trend for massive stars. Using L_x/L_{bol} as indicator, the trend observed for massive stars has a well defined saturated value (except for the most massive bin). On the contrary, if the L_x indicator is considered, the L_x is a function of rotation in the non-saturated regime where is independent from stellar mass.

This behaviour, across all spectral types, is clearly seen in Fig. 3.7 where we represent the collection of all best-fit relations found by Pizzolato et al. (2003) in all the mass ranges including the new relations found in this work in the non-saturated regime. In the left panel our best-fits are placed in the same range of non-saturated regime of all spectral types while in the right panel (L_x/L_{bol} vs.$P_{\rm rot}$) the new curve of the M dwarfs is on the right of the curves of more massive stars. We have extended the study of X-ray emission of the M dwarfs in non-saturated regime and finding a continuous shift of the L_x/L_{bol} vs. $P_{\rm rot}$ power law towards higher $P_{\rm rot}$ values.

Consequently we are able to determine in more accurate way than in previous works the value of rotation period at which the saturation occurs (P_{sat}) for dM stars. Assuming a well defined saturated value for all mass range in L_x/L_{bol} as -3.3 (except for most massive bin) and knowing the mean bolometric luminosity for each temperature group it is possible

Table 3.5: X-ray saturated level for M dwarfs.

SpT	N*	$\log L_{x,\mathrm{sat}}$ (erg s^{-1})	$\log L_{x,\mathrm{sat}}/L_{bol}$	$P_{sat}^{L_x}$ (days)	$P_{sat}^{L_x/L_{bol}}$ (days)
3400-3700 K (M0 − M2.5)[a]	11	$28.76 \pm 0.2^{(c)}$	$-3.3 \pm 0.2^{(c)}$	$8.1^{(a)}$	$9.6^{(a)}$
3700-3800 K (K7 − M1.5)[a]	8	$29.16 \pm 0.2^{(c)}$	$-3.3 \pm 0.3^{(c)}$	$4.4^{(a)}$	$4.4^{(a)}$
2900-3680 K (M2 − M5.5)[c]	21	28.2 ± 0.2	-3.3 ± 0.2	> 10.8	>13.1
K7 − M2[b]	5	29.2 ± 0.4	-3.0 ± 0.4	<10	–
M3 − M4[b]	7	28.6 ± 0.3	-3.1 ± 0.2	<10	–

$^{(a)}$ This work; $^{(b)}$ Stelzer et al. (2016); $^{(c)}$Pizzolato et al. (2003)

estimate a better saturated value for each temperature bin in L_x instead of assume the value of 28.2 (erg s^{-1}) established by Pizzolato et al. (2003). The derived values are presented in Table 3.5.

3.3 Chromospheric activity

3.3.1 S-index

In order to study the chromospheric activity for each star in the sample the Ca II H & K S-index was computed from HARPS-N spectra. Chromospheric activity has been traditionally studied using the R'_{HK} index defined as the ratio of the emission from the chromosphere in the cores of the Ca II H & K lines to the total bolometric emission of the star.

To use the R'_{HK} index, the core fluxes have to be corrected from the photospheric contribution (R_{phot}), using an empirical calibration based on color index $B - V$, where $R'_{HK} = R_{HK} - R_{phot}$ (Noyes et al. 1984). R_{phot} depends only on the $B - V$ so, the same value of R_{phot} is subtracted from R_{HK} for all stars of the same spectral type.

Since we have several spectra for each source to compute the R_{HK} value it is necessary to use the mean value of the S-index. To determine the S-index value we summ the flux in the central cores of the Ca II H & K lines and divide by the fluxes in two 20 Å windows on either side of the line. Our definition of the bandpass for the S-index is done following Henry et al. (1996).

$$S = \frac{F_{Hcore} + F_{Kcore}}{F_{3901\text{Å}} + F_{4001\text{Å}}} \tag{3.3.1}$$

where F_{Hcore} and F_{Kcore} are the fluxes in a 3.28 Å window width centred in the cores of the Ca II H & K lines (3968.47 and 3933.67 Å, respectively) and the continuum fluxes on the side of the lines ($F_{3901Å}$ and $F_{4001Å}$) are measured in two 20 Å window with central wavelengths at 3901.07 Å and 4001.07 Å.

To get R'_{HK} is necessary to calibrate the S-index with the S_{MW} in the Mount Wilson HK scale. Once the S-index is set into the Mount Wilson scale, R'_{HK} can be computed as: $R_{HK} = 1.340 \times 10^{-4} \cdot C_{cf} \cdot S$ following the calibration by Noyes et al. (1984) which is valid only in the $0.45 < B - V < 0.9$ range, outside of our sample range. We note however that Suárez Mascareño et al. (2015) extended the original R'_{HK} calibration up to (B-V) = 1.9.

However, for the purpose of this work it is not needed the use of R'_{HK} therefore we do not attempt to convert our S-index into the Mount Wilson scale or to correct it from the stellar photospheric contribution. In Table 3.6 all the values of S-index for our sample are summarized.

In order to test the usefulness of S-index as activity indicator we use as activity calibrator the X-ray luminosity, derived in the previous sections. Fig. 3.8 shows the S-index values as a function of the X-ray luminosity, L_x. The correlation between S-index and L_x shows a high Spearman correlation coefficient ($\rho = 0.82$). Considering that the X-ray and spectroscopic measurements are not simultaneous we can conclude that there is a good correlation between these two quantities and that the S-index obtained in this work is an adequate activity indicator for M dwarfs.

We have noted that it is not necessary to convert S-index into the Mount Wilson scale but even so, it is possible to obtain it (see Table 3.6) thanks to the YABI platform. YABI is a Python web application installed at IA2 [I] in Trieste (Italy), that allows authorized users to run the HARPS-N DRS pipeline on their own proprietary data with custom input parameters.

Right panel of Figure 3.8 shows the equivalence to use S-index or S-index into the Mount Wilson scale (in the following, S_{MW}) in our sample of M dwarfs. The Spearman correlation coefficient is $\rho = 0.98$. We conclude the S_{MW}-index obtained with YABI application also can be used in a reliable way to compute the S-index value when dealing with low-mass stars.

[I] IA2 is an Italian Astrophysical research infrastructure project that aims at co-ordinating different national initiatives to improve the quality of astrophysical data services. It aims at co-ordinating these developments and facilitating access to this data for research purposes.

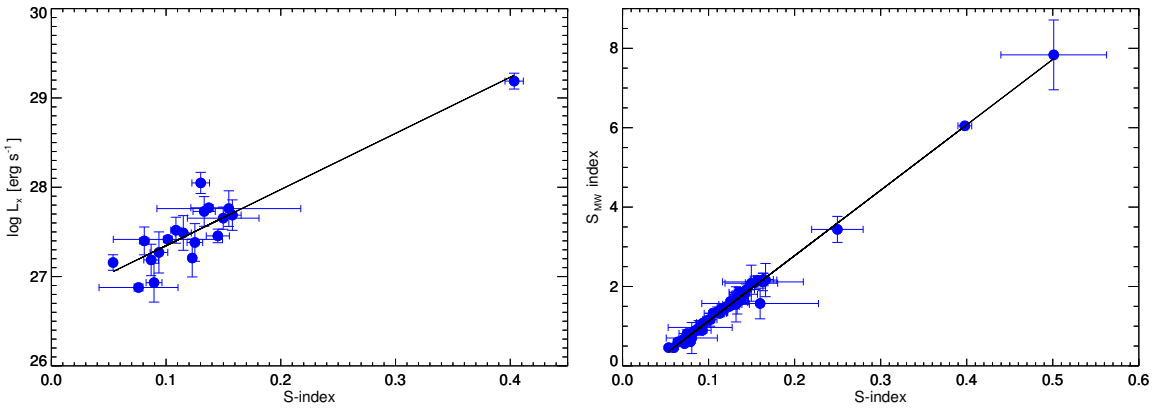

Figure 3.8: Correlation between coronal and chromospheric activity indicators. *Left panel:* Correlation between S-index and L_x *Right panel:* Correlation between S-index and S-index into the Mount Wilson scale (S_{MW}).The black line represents the best linear fit.

Table 3.6: S-index and S_{MW}index values.

Name	S-index	S_{MW}index
BPM96441	$0.1361 \pm 4.0 \times 10^{-4}$	1.7425 ± 0.0392
G243-30	$0.1324 \pm 3.0 \times 10^{-4}$	1.0826 ± 0.0263
GJ1030	$0.1253 \pm 4.0 \times 10^{-4}$	1.5484 ± 0.0355
GJ1074	$0.1173 \pm 3.0 \times 10^{-4}$	1.0489 ± 0.7306
GJ119A	$0.0885 \pm 3.0 \times 10^{-4}$	0.9558 ± 0.0437
GJ119B	$0.0798 \pm 3.0 \times 10^{-4}$	0.7866 ± 0.0474
GJ150.1B	$0.1364 \pm 4.0 \times 10^{-4}$	1.7628 ± 0.0228
GJ156.1A	$0.1122 \pm 3.0 \times 10^{-4}$	1.3682 ± 0.03
GJ15A	$0.0638 \pm 2.0 \times 10^{-4}$	0.3267 ± 0.8186
GJ16	$0.1174 \pm 4.0 \times 10^{-4}$	1.4469 ± 0.0282
GJ162	$0.1332 \pm 5.0 \times 10^{-4}$	1.5969 ± 0.0287
GJ184	$0.0751 \pm 2.0 \times 10^{-4}$	0.7944 ± 0.0138
GJ2	$0.1339 \pm 4.0 \times 10^{-4}$	1.7267 ± 0.014
GJ21	$0.1536 \pm 5.0 \times 10^{-4}$	2.0935 ± 0.0313
GJ2128	$0.0721 \pm 3.0 \times 10^{-4}$	0.5603 ± 0.0419
GJ26	$0.0894 \pm 3.0 \times 10^{-4}$	0.9294 ± 0.0335
GJ272	$0.1247 \pm 4.0 \times 10^{-4}$	1.5201 ± 0.0469
GJ3014	$0.1569 \pm 8.0 \times 10^{-4}$	2.1101 ± 0.6905

Table 3.6: S-index and S_{MW}index values. (continue)

Name	S-index	S_{MW}index
GJ3117A	$0.1179 \pm 3.0 \times 10^{-4}$	1.4645 ± 0.0326
GJ3126	$0.0986 \pm 3.0 \times 10^{-4}$	0.9522 ± 0.0208
GJ3186	$0.124 \pm 2.0 \times 10^{-4}$	1.5560 ± 0.0244
GJ3352	$0.1258 \pm 3.0 \times 10^{-4}$	1.6286 ± 0.0332
GJ3649	$0.1419 \pm 5.0 \times 10^{-4}$	1.8044 ± 0.0385
GJ3822	$0.1631 \pm 9.0 \times 10^{-4}$	2.1156 ± 0.0806
GJ3942	$0.1573 \pm 5.0 \times 10^{-4}$	2.1531 ± 0.0217
GJ399	$0.1003 \pm 5.0 \times 10^{-4}$	0.7206 ± 0.4315
GJ3997	$0.071 \pm 2.0 \times 10^{-4}$	0.6706 ± 0.0172
GJ3998	$0.1101 \pm 4.0 \times 10^{-4}$	1.3508 ± 0.03
GJ4057	$0.1018 \pm 4.0 \times 10^{-4}$	1.1635 ± 0.0242
GJ408	$0.0929 \pm 3.0 \times 10^{-4}$	0.8978 ± 0.0177
GJ4092	$0.0931 \pm 2.0 \times 10^{-4}$	1.0664 ± 0.0262
GJ412A	$0.0596 \pm 2.0 \times 10^{-4}$	0.4571 ± 0.0079
GJ414B	$0.1143 \pm 4.0 \times 10^{-4}$	1.3230 ± 0.0186
GJ4196	$0.0642 \pm 2.0 \times 10^{-4}$	0.5871 ± 0.0189
GJ4306	$0.1352 \pm 5.0 \times 10^{-4}$	1.8530 ± 0.0323
GJ450	$0.1497 \pm 5.0 \times 10^{-4}$	2.0830 ± 0.0291
GJ47	$0.0937 \pm 3.0 \times 10^{-4}$	1.0044 ± 0.0316
GJ476	$0.0643 \pm 2.0 \times 10^{-4}$	0.6047 ± 0.0343
GJ49	$0.1799 \pm 5.0 \times 10^{-4}$	2.4738 ± 0.0293
GJ521A	$0.075 \pm 2.0 \times 10^{-4}$	0.8153 ± 0.0224
GJ548A	$0.1312 \pm 4.0 \times 10^{-4}$	1.7204 ± 0.0190
GJ552	$0.1002 \pm 3.0 \times 10^{-4}$	1.1625 ± 0.0256
GJ606	$0.1351 \pm 4.0 \times 10^{-4}$	1.8055 ± 0.0304
GJ625	$0.0805 \pm 2.0 \times 10^{-4}$	0.7026 ± 0.0161
GJ671	$0.0789 \pm 2.0 \times 10^{-4}$	0.6072 ± 0.0249
GJ685	$0.1437 \pm 4.0 \times 10^{-4}$	1.9145 ± 0.0151
GJ686	$0.0706 \pm 1.0 \times 10^{-4}$	0.5501 ± 0.0153
GJ694.2	$0.1155 \pm 4.0 \times 10^{-4}$	1.4121 ± 0.0284
GJ70	$0.0902 \pm 4.0 \times 10^{-4}$	0.9687 ± 0.0351
GJ720A	$0.084 \pm 3.0 \times 10^{-4}$	0.8814 ± 0.0105

Table 3.6: S-index and S_{MW}index values. (continue)

Name	S-index	S_{MW}index
GJ731	$0.1054 \pm 3.0 \times 10^{-4}$	1.3234 ± 0.0118
GJ740	$0.1128 \pm 4.0 \times 10^{-4}$	1.3227 ± 0.0096
GJ793	$0.1319 \pm 4.0 \times 10^{-4}$	1.5503 ± 0.0281
GJ895	$0.1227 \pm 3.0 \times 10^{-4}$	1.5185 ± 0.0129
GJ908	$0.0536 \pm 1.0 \times 10^{-4}$	0.4595 ± 0.0041
GJ9404	$0.1242 \pm 4.0 \times 10^{-4}$	1.4994 ± 0.0212
GJ9440	$0.1125 \pm 4.0 \times 10^{-4}$	1.3387 ± 0.0279
GJ9689	$0.1125 \pm 4.0 \times 10^{-4}$	1.3466 ± 0.0371
GJ9793	$0.1662 \pm 5.0 \times 10^{-4}$	2.1614 ± 0.0234
NLTT10614	$0.1072 \pm 4.0 \times 10^{-4}$	1.2808 ± 0.0419
NLTT21156	$0.2497 \pm 16.0 \times 10^{-4}$	3.438 ± 0.1343
NLTT4188	$0.1404 \pm 4.0 \times 10^{-4}$	1.7731 ± 0.0289
NLTT52021	$0.1432 \pm 6.0 \times 10^{-4}$	1.7347 ± 0.0513
NLTT53166	$0.0943 \pm 3.0 \times 10^{-4}$	1.0874 ± 0.0271
TYC1795-941-1	$0.1319 \pm 3.0 \times 10^{-4}$	1.6931 ± 0.0444
TYC2703-706-1	$0.5011 \pm 16.0 \times 10^{-4}$	7.8713 ± 0.1534
TYC2710-691-1	$0.1638 \pm 4.0 \times 10^{-4}$	2.2647 ± 0.0356
TYC3379-1077-1	$0.1599 \pm 13.0 \times 10^{-4}$	1.5717 ± 0.1225
TYC3720-426-1	$0.3978 \pm 11.0 \times 10^{-4}$	6.0468 ± 0.055
TYC743-1836-1	$0.1637 \pm 3.0 \times 10^{-4}$	2.1759 ± 0.0489
2MASS J2235*	$0.1431 \pm 7.0 \times 10^{-4}$	$- \pm -$
StKM 1-650	$0.1378 \pm 4.0 \times 10^{-4}$	1.6556 ± 0.0757

*2MASS J22353504+3712131

3.4 Relation between chromospheric and coronal activity

Flux-flux relationships between activity indicators originated in different temperature regimes of the stellar outer atmospheres (chromosphere, transition region and corona) have been extensively studied in the literature for different kind of stars (e.g. Montes et al. 1996b, 1995; Stelzer et al. 2012). In the following, we test whether these relationships also hold for early-

M dwarfs by using the HADES sample (see sect. 1.4). We use the Ca II H & K and $H\alpha$ line flux excess data to study the flux-flux relationships between the chromospheric activity indicators and the coronal X-ray emission.

In order to measure the flux excess emitted in the Ca II H & K and $H\alpha$ lines, a specific technique has been developed to correct the spectra for instrumental and atmospheric effects by means of synthetic spectra. This leads to the calibration of the spectra to a common absolute flux scale, which enables the measurements of line flux excess in units of the flux at the stellar surface. An extensive description of this procedure to compute the excess fluxes is provided by Scandariato et al. (2017).

Figure 3.9 shows the comparison between pairs of fluxes of different chromospheric lines for the stars in our sample. Power-law functions were fitted to the data,

$$\log F_1 = a_0 + a_1 \log F_2 \tag{3.4.1}$$

where F_1 and F_2 are the fluxes of two different lines and a_0 and a_1 the fit coefficients. Note that here we are considering the flux excesses measured over the combined spectra [II], so for each star all the fluxes are obtained from the same average spectrum.

Several samples are overplotted for comparison: a sample of F, G and K stars from López-Santiago et al. (2010); Martínez-Arnáiz et al. (2010, 2011); a sample of late-K and M dwarfs (from the same authors); and a sample of pre-MS M stars from Stelzer et al. (2013a). For better comparison with our data, from the last sample only stars in the spectral range K7-M3 were considered. Fits were obtained following the least-squares bisector regression described by Isobe et al. (1990) and the values of a_0 and a_1 obtained in this work are shown in Table 3.7

Our sample of M dwarfs seems to follow the same trend as FGK stars and other late-K/early-M in the Ca II H vs. Ca II K plane (Figure 3.9, left panel) without any obvious deviation from the other samples. The $H\alpha$ vs. Ca II K plot is shown in the right panel of Fig. 3.9. Martínez-Arnáiz et al. (2011) identified two branches in the flux-flux relationships when the $H\alpha$ line is considered. The inactive branch is composed of the majority of the stars including stars with spectral types from F to M. The deviating stars constitute the upper or active branch, which is composed of young late-K and M dwarfs with saturated $H\alpha$ emission. Figure 3.9, right panel, shows our M dwarfs sample located in the inactive branch. We can

[II]For each star we have observed several spectra also in different seasons. Here we are considering the average spectrum neglecting any time variation that can occurs.

Table 3.7: Coefficients of the flux-flux relationships.

$\log F_1$	$\log F_2$	a_0	a_1	a_1 Other works
Ca II K	Ca II H	0.0121 ± 0.0006	1.0110 ± 0.0001	$0.99 \pm 0.03^{(a)}$; $0.98 \pm 0.02^{(b)}$; $0.86 \pm 0.08^{(c)}$
H_α	Ca II K	-5.55 ± 0.02	2.069 ± 0.003	$1.13 \pm 0.10^{(d,e)}$; $0.95 \pm 0.08^{(a)}$; $1.20 \pm 0.07^{(b)}$
F_x	Ca II K	1.22 ± 0.14	0.86 ± 0.03	$2.38 \pm 0.26^{(f,e)}$; $1.06 \pm 0.17^{(g)}$
F_x	H_α	1.95 ± 0.15	0.76 ± 0.03	$2.11 \pm 0.20^{(d,e)}$; $1.60 \pm 0.07^{(b)}$

$^{(a)}$ Martínez-Arnáiz et al. (2010); $^{(b)}$ Martínez-Arnáiz et al. (2011); $^{(c)}$Stelzer et al. (2012); $^{(d)}$Montes et al. (1995); $^{(e)}$Montes et al. (1996a); $^{(f)}$Montes et al. (1996b); $^{(g)}$Stelzer et al. (2013a)

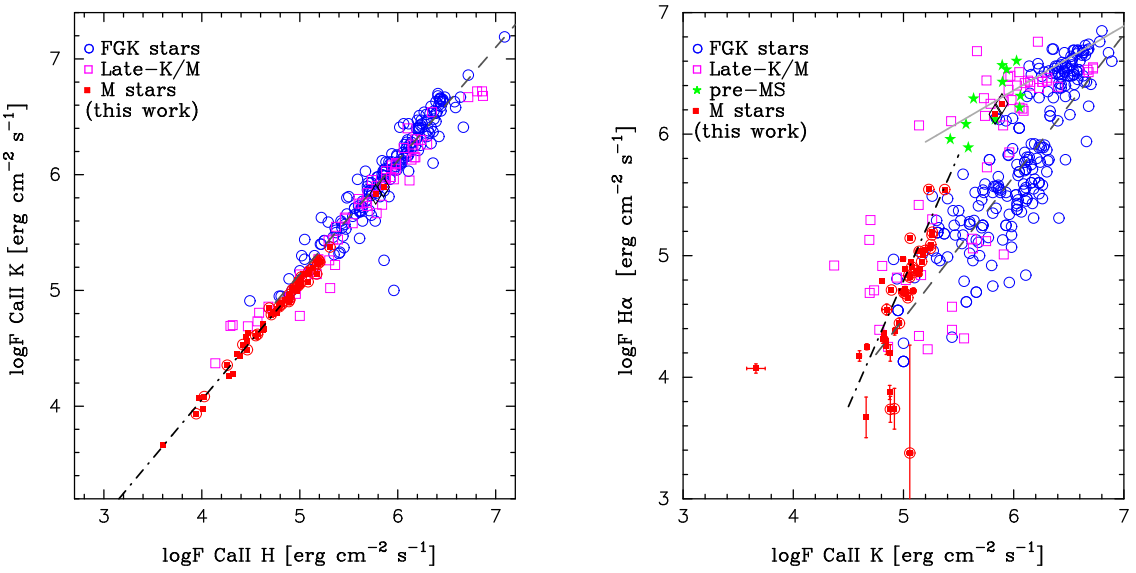

Figure 3.9: Flux-flux relationships between calcium lines (Ca II H & K, left panel), and between $H\alpha$ and Ca II K (right panel). M dwarfs from this work are plotted with red filled squares; FGK stars from López-Santiago et al. (2010); Martínez-Arnáiz et al. (2010, 2011) with open circles, late-K and M stars from the literature (same references than for FGK stars) are shown in purple open squares; green stars denote the M0-M3 pre-MS M stars from Stelzer et al. (2013a). Possible young disc stars in our M star sample are shown with circles. The dot-to-dash black line represents our best fit; the relations for the active and inactive branches by Martínez-Arnáiz et al. (2011) are shown in light grey solid and dashed dark grey lines respectively.

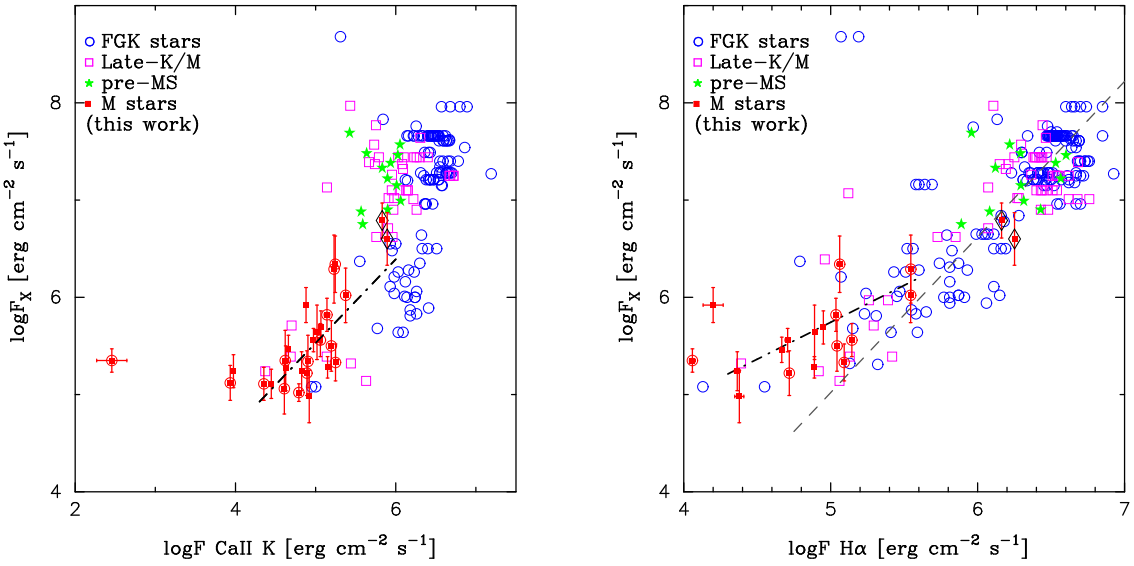

Figure 3.10: Flux-flux relationships between X-ray and the calcium line Ca II K *(left panel)*, and between X-ray and the Hα line *(right panel)*. Colours and symbols are as in Fig. 3.9

conclude that our sample is complementary to the literature samples because it follows the same flux-flux relationships and it constitutes an extension of the analysis of the Ca II H & K and $H\alpha$ flux-flux relationships of main-sequence dwarfs to the low flux domain.

Now, we study the relation between X-ray emission and Ca II K emission and $H\alpha$. All the stars with X-ray detections show Ca II K emission while only 69% of the stars with X-ray data show emission in $H\alpha$. Figure 3.10 shows the X-ray flux as a function of the flux in Ca II K (left) and $H\alpha$ (right). No distinction between active and inactive branches was found in the literature for the $\log F_x$ vs. Ca II K line and $H\alpha$ relationships (Martínez-Arnáiz et al. 2011). Our sample of M dwarfs seems to follow the same tendency as the literature estimates but our analysis clearly reveals that our M dwarfs have lower levels of X-ray fluxes and chromospheric emission than the FGK stars. Our lower levels of X-ray fluxes translates into significant lower slopes than the ones previously reported in the literature (see Table 3.7). The analysis of our M dwarfs sample is complementary to other literature samples, extending the analysis of the flux-flux relationships to the low-chomospheric and low-coronal fluxes domain being our sample a benchmark for the characterisation of magnetic activity

at low levels.

3.5 Summary and conclusions

The aim of this chapter was to test the relations between activity, rotation and stellar parameters and to study if the flux-flux relationships for main-sequence FGK stars also hold for early-M dwarfs. The importance of analysing all these relations using our sample of M dwarfs and concluding that are also valid for these targets, lies in that our data fill the slow rotation area. This area exactly corresponds with a specific region in which planets in habitable zone could be discovered. However, as shown in Figure 3.11 taken from Newton et al. (2016), the habitable zone of early M dwarfs coincides with the stellar rotation period. In this case when RV variations induced by activity coincide with the planetary orbital period, it can be difficult to identify the planetary signal. As demonstrated by Newton et al. (2016), for 0.25 $M_{\odot} < M_{*} < 0.5\ M_{\odot}$ (corresponding to M1-M4 SpT) the stellar rotation can be a confounding factor on searching for habitable planets around early-M dwarfs and dealing with activity effect is assumed. The vast majority of our studied sample covers the stellar rotation period range between 15 to 60 days and mass range between 0.35 to 0.7

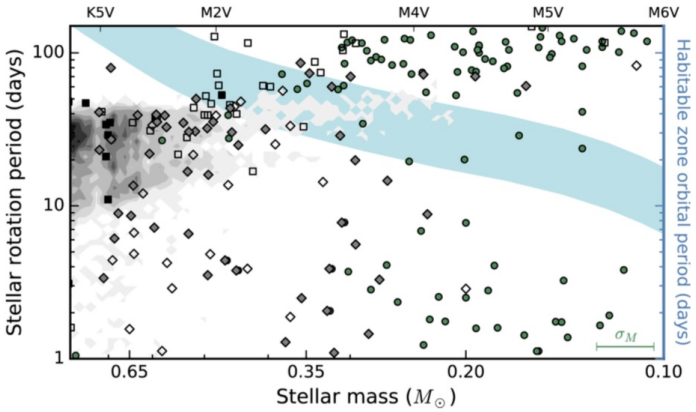

Figure 3.11: Figure taken from Newton et al. (2016). Stellar rotation period as a function of stellar mass and its relation to the planetary habitable zone. Gray shading shows the rotation period distribution. The different dots are data collected in literature. The blue shaded region shows the habitable zone as a function of stellar mass. For early M dwarfs, the habitable-zone period overlaps with the rotation periods of typical stars, both of which are of about 40 days. This coincidence complicates the radial velocity detection of habitable planets around early M dwarfs, but not for mid-to-late M dwarfs, or for G and K dwarfs.

$M_{\odot}$, i.e., the region in which habitable zone period overlaps with the rotation periods. This confirm the big challenge that the stellar activity supposes for our radial velocity survey on discovering planets in early M dwarfs and our interest on a good understanding.

Chapter 4

Planets around M dwarf stars

In this chapter we discuss in detail the analysis developed to search for planets in the low-mass star domain (M dwarfs), in the framework of the HADES collaboration. The studied sample (see Sect. 1.4) is composed by 78 late-K/early M dwarfs but an individual and thorough analysis for each star is needed in order to identify new possible planets. In particular, in this chapter we focus on the analysis of two dM stars that show high significant periodic signals pointing to the possible presence of companions. The work presented in this chapter is still ongoing. I will present the today results and the future steps needed to confirm the presence of companions.

4.1 Search for planets around GJ 720 A

GJ 720 A is an M0.5 M dwarf located at a distance of 15.56 ± 0.24 pc (Lépine & Gaidos 2011) from the Sun. Basic stellar parameters (effective temperature, stellar metallicity, spectral type, mass, radius, surface gravity, and luminosity) were computed by using the same spectra used in RV analysis, following the procedure described in Maldonado et al. (2015a). GJ 720 A has a rotation period (P_{rot}) of 34.5 ± 4.7 days determined from Ca II H & K and $H\alpha$ spectroscopy time-series (Suárez Mascareño et al. A&A, in press). Table 4.1 shows the main stellar properties of GJ 720 A.

4.1.1 Spectroscopic observations

GJ 720 A has been monitored from the 26th of May 2013 to the 17th of October 2017 for a total of 112 data points. The spectra were obtained with the high resolution ($R \sim 115,000$)

Table 4.1: Stellar parameters of GJ 720 A.

Parameters	Value
α (J2000)	18:35:18.0
δ (J2000)	+45:44:35
B [mag]	11.26
V [mag]	9.85
d (pc)	15.56 ± 0.24
Derived from HARPS-N spectra	
$T_{\rm eff}$ (K)	3837 ± 69
log g (dex)	4.71 ± 0.05
[Fe/H] (dex)	-0.14 ± 0.09
$v \sin i$ (km s^{-1})	0.99 ± 0.53
P_{rot} (days)	34.5 ± 4.7
Mass ($M_\odot$)	0.57 ± 0.06
Radius ($R_\odot$)	0.56 ± 0.06
log $L/L_\odot$	-1.217 ± 0.096

optical echelle spectrograph HARPS-N with exposure time of 15 minutes and average signal-to-noise ratio (S/N) of 76 at 5500 Å. Data were reduced using the latest version of the Data Reduction Software (DRS V3.7, Lovis & Pepe 2007) and RVs were computed by matching the spectra with an high S/N template obtained by co-adding the spectra of the target, as implemented in the Java-based Template-Enhanced Radial velocity Re-analysis Application (TERRA, Anglada-Escudé & Butler 2012), which provides accurate RVs when it is applied to M-dwarfs, considering orders redder than the 22nd. The TERRA RVs show a root mean square (rms) dispersion of 4.04 ms^{-1} and a mean error of 0.8 ms^{-1}. The radial velocity time-series is shown in Fig. 4.1.

4.1.2 Data analysis

The first step of the RV data analysis consists in identifying significant periodic signals in the data. The procedure was applied to the full RV data using the Generalized Lomb-Scargle (GLS) periodogram algorithm (Zechmeister & Kürster 2009). The periodogram considers significant periods if the power is higher than a chosen false alarm probability (FAP). Figure 4.2 reports the GLS periodogram where there are several significant peaks higher than the FAP 0.1 % with the most prominent peak at 19.49 ± 0.01 days. FAPS

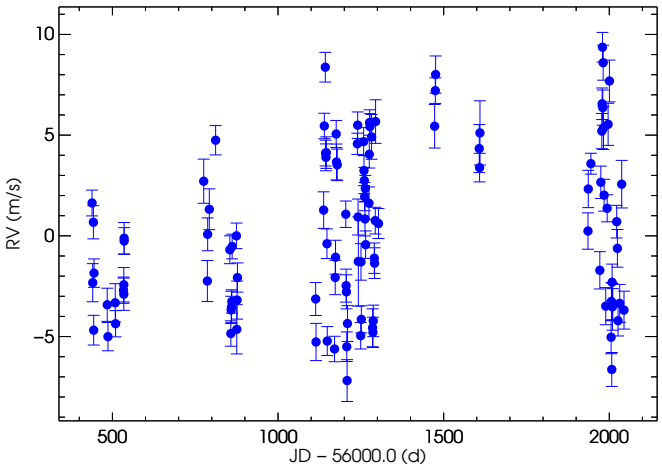

Figure 4.1: Radial velocity time-series for GJ 720 A derived with the TERRA pipeline.

were estimated by using a bootstrap method (Endl et al. 2001) with 1,000 iterations. To verify the presence of possible aliasing phenomena (Dawson & Fabrycky 2010), resulting from the discrete sampling, we study the periodogram of the spectral window function in

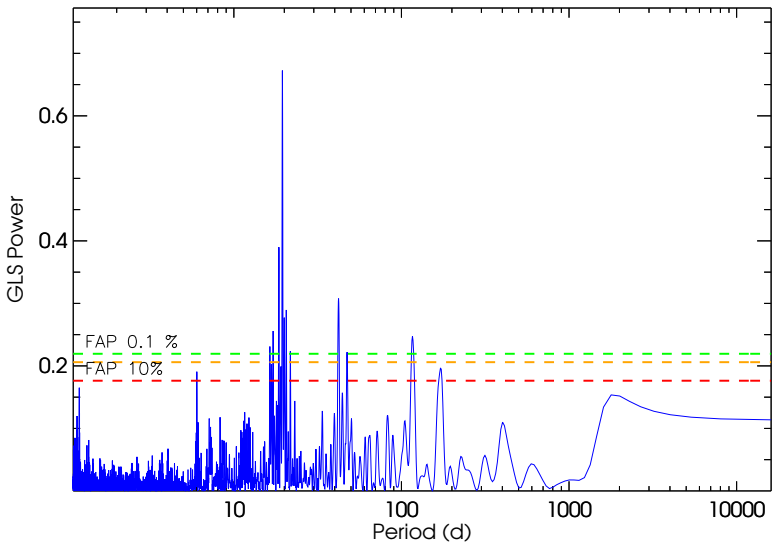

Figure 4.2: GLS periodogram of the radial velocities of GJ 720 A of the original data. The dashed lines indicate the 0.1% (green), 1% (orange) and 10% (red) level of false alarm probability.

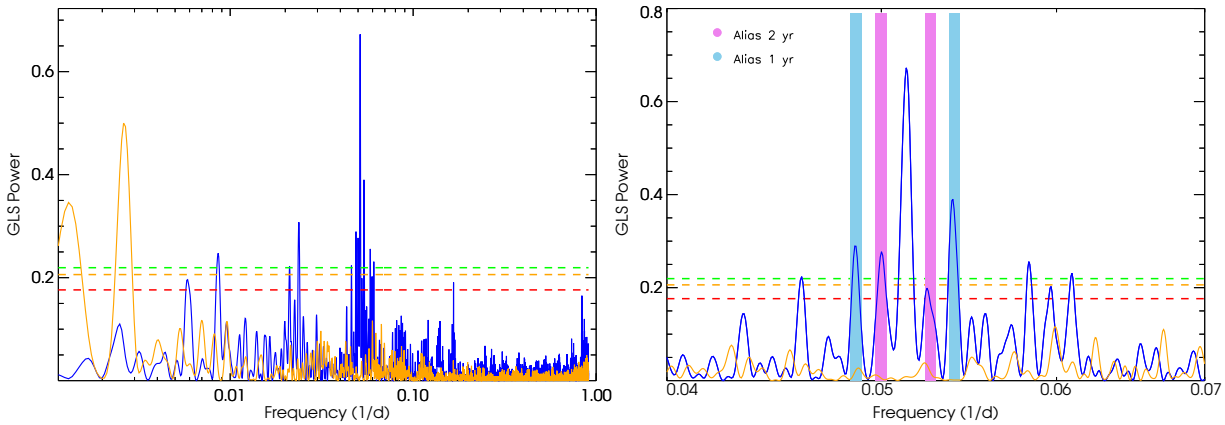

Figure 4.3: Spectral window function and RVs GLS periodogram for GJ 720 A expressed in frequency. *Left panel:* The orange line shows the spectral window function and the blue line corresponds to the GLS of RV in the frequency range 0.00125-1 d^{-1} (1-800 days). *Right panel:* Zoom-in around the most significant period at 19.49 days (0.051315 d^{-1}). The horizontal dash lines correspond to the different levels of the false alarm probability, 0.1% (green), 1% (orange) and 10% (red). The violet and blue lines represent the 1 and 2 years alias of the 19.49 days period.

Figure 4.3. This function is overplotted to the GLS periodrogram of RVs to compare the frequencies of predicted aliases with peaks present in the data. Left panel of Figure 4.3 shows the periodogram of the window function (orange line) in the frequency range 0.00125-1 d^{-1} (1-800 days) showing two highest peaks that correspond with the periodic modulation in the spectral window around 1 and 2 years. Searching for this modulation around the highest RV peak, in right panel of Fig. 4.3 we found that the most significant peaks seen around 19.49 days are due to alias at 1 and 2 years of the original higher peak signal (19.49 days).

In order to visualize the stability of the peaks we calculated the GLS periodogram increasing the number of observations, from 20 to 112, adding one observation at a time (e.g. Affer et al. 2016). We compute the power corresponding to each period in the range 1.2 to 500 days, for each of the 92 periodograms obtained. Left panel of Fig. 4.4 shows the stacked periodograms while right panel of Fig. 4.4 shows a zoom-in around the most significant period found at 19.49 days. It is clearly visible how increasing the number of observations, the period at 19.49 days shows a higher and narrower peak as expected in case of a keplerian nature of the signal.

The RV data folded at the best-fit orbital period, as well as the best-fit orbital solution is shown in Figure 4.5. It shows a semi-amplitude of 4.8 ± 0.3 ms^{-1}. Following with the

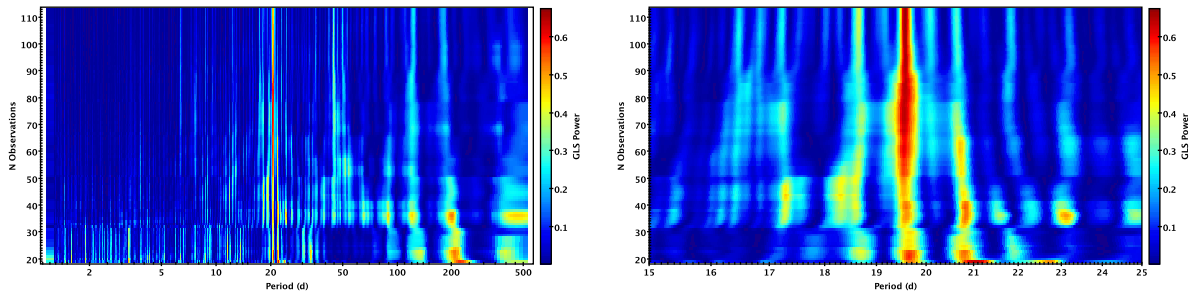

Figure 4.4: GLS periodogram power of the inspected periods in RV as a function of the number of observations. *Left panel:*The most significant period (the reddest ones) at 19.49 days clearly visible with a high power for $N_{obs} > 55$. *Right panel:* Zoom-in around the 19.49 days period.

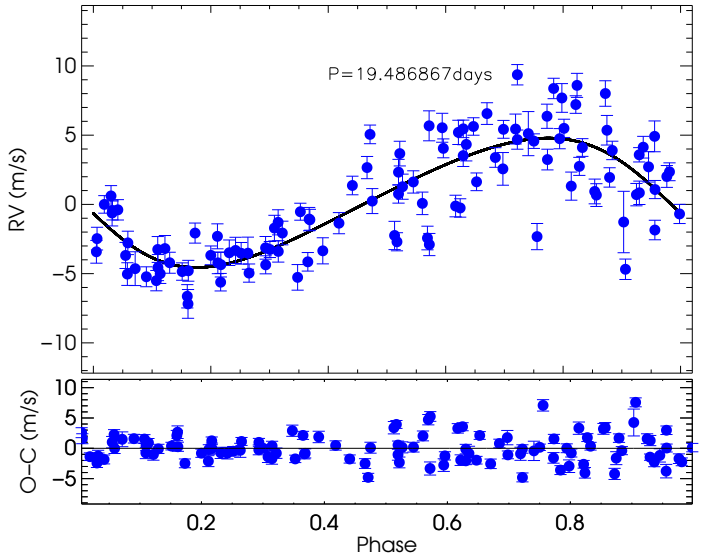

Figure 4.5: *Top panel:* Best orbital solution phase-folded for GJ 720 A for the trial period at 19.49 days. *Bottom panel:* Residual RVs after subtracting the best orbital solution.

analysis, in bottom panel of Fig. 4.6 we remove the orbital solution corresponding to the highest significant period (P = 19.49 d). The subtraction produces a strong decrease of the significance of the 19.49 days and of all its identified aliases (see right panel of Fig. 4.3) but others significant peaks are yet seen in the periodogram around 40-50 days (0.02-0.025 d^{-1}) and 80-105 days (0.0125- 0.0095 d^{-1}). In the next section we will study the possible stellar activity effects and how they can be related with the modulations found in RV.

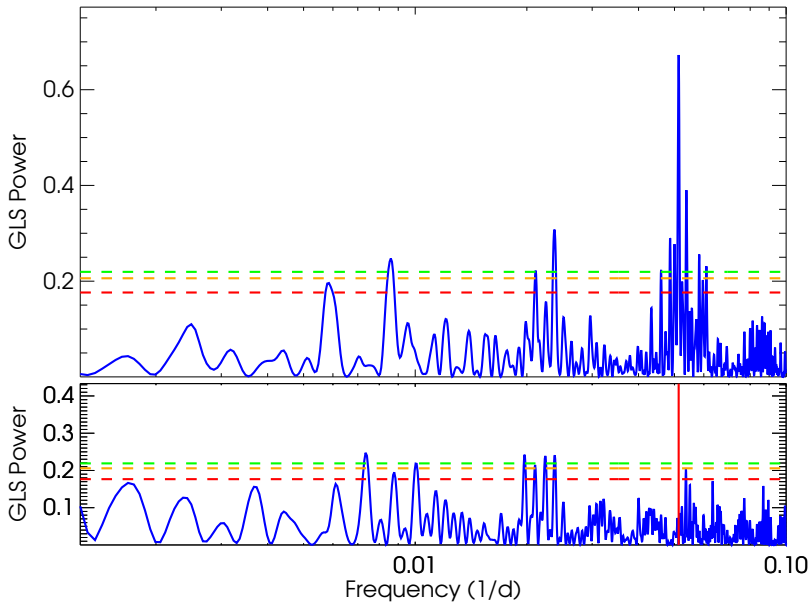

Figure 4.6: *Top panel:* GJ 720 A GLS Periodogram in phase domain of the original RV. *Bottom panel:* GLS periodogram GJ 720 A after removing the signal at 19.49 days. Significant peaks around 0.025-0.02 d^{-1} (40-50 days) and 0.0095-0.0125 d^{-1} (80-105 days) remain. The dashed lines indicate 0.1% (green), 1% (orange) and 10% (red) levels of false alarm probability. The red vertical line indicates the position of the removed signal at 19.49 days.

4.1.3 Origin of periodic signals

As explained in sections 1.2 and 1.3, M dwarfs are on average more active than solar-like stars (Leto et al. 1997; Osten et al. 2005) with inhomogeneities on their surface that rotate with the star. These inhomogeneities cause RV variations due to the distortion of the spectral line profile that can be confused with planetary signals or even hide it. In order to disentangle the effects of activity from true RV variations we analysed the spectroscopic indicators of chromospheric activity, the Ca II H & K lines (S-index, explained in detail in section 3.3.1) and the bisector velocity span (BVS). The time-serie of the S-index activity indicator is presented in Fig. 4.7 after removing a linear trend observed in the S-index data. Figure 4.8 (left panel) shows the relations between the S-index before removing the linear trend observed with the RV measurements, because studying the relation between the both quantities only after S-index de-trend could eliminate some kind of possible correlation between them. On the other hand, right panel of Figure 4.8 shows the relation between the

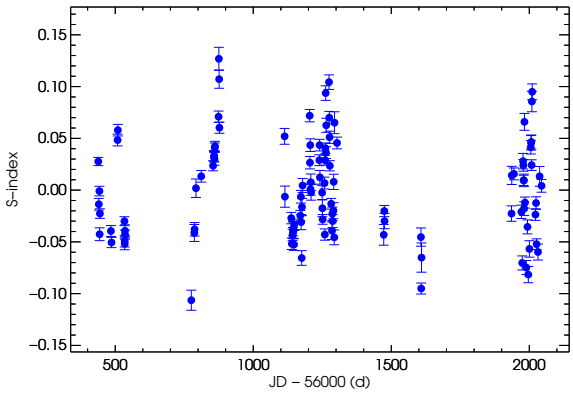

Figure 4.7: S-index time-serie after linear trend removal for GJ 720 A.

BVS with the RVs. As explained in section 1.2 any correlation between these quantities and the RV can be a good indication that the observed RV variations are due to changes in the shape of the lines produced by stellar surface features. However the absence of a correlation does not guarantee that stellar activity is not the origin of the RV variations. In our case no significant correlation was found between the S-index (both cases) and the BVS with the RV. Results from a Spearman's correlation test gives a value of $\rho = 0.085$ with p-value $= 0.37$ for the S-index before removing the linear trend. For the BVS case the test results are $\rho = 0.074$ and p-value $= 0.44$. In the following, all the S-index data analysed correspond with those resulting after removing the observed linear trend.

We analyse the GLS periodogram of the S-index (right panel of Fig. 4.9) from the values

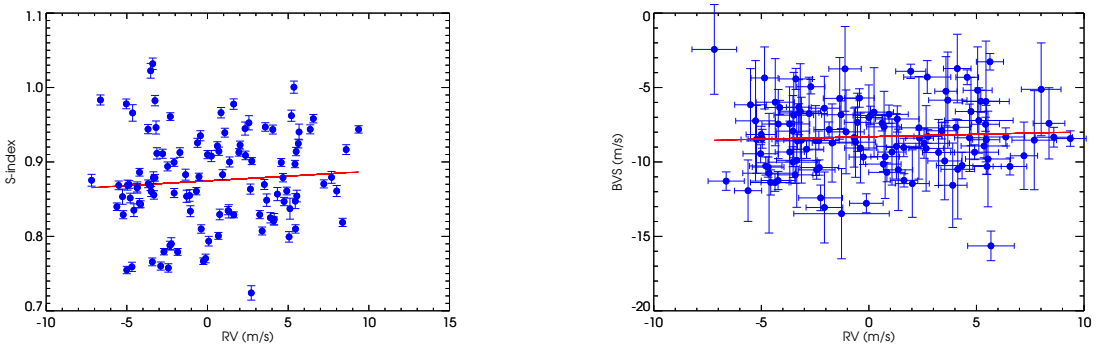

Figure 4.8: *Left panel:* Relation between S-index (before removing linear trend) and RV for GJ 720 A. *Right panel:* Relation between BVS and RVs. No significant correlation was found in any case.

obtained after removing the observed linear trend in the time-series. The most significant peak was found at 518 days. After removing this long-term variability (Fig. 4.9, right panel) we obtain a clear and significant period at 36.58 ± 0.1 days corresponding with the rotation period of the star. The same technique was used to obtain the rotation period of the star by Suárez Mascareño et al. (A&A, in press) established at $P_{\rm rot} = 34.5 \pm 4.7$ days. The small difference between the two measurements might be related to the different number of observations taken into account when the analysis was done.

Figure 4.10 compares the GLS periodograms of the S-index (before and after removing the long-term signal, top and middle-top panels), the BVS (middle-bottom panel) and the residual RVs (bottom panel). Despite of removing at the beginning of the analysis the observed linear trend from the time-series of the S-index, the first panel of Figure 4.10 still presents another long-term signal at 518 days, as previously explained. Therefore, the residual long-term signal (Fig. 4.10 bottom panel) could be explained by the presence of long-term activity. While the significant peaks around 40-50 days in the RV residual (bottom panel) also can be connected with some stellar activity effect compatible with the stellar rotation ($\sim$ 40 days, middle-top panel). On the other hand, BVS data present no significant peak at 19.49 days (Fig. 4.10 middle-bottom panel).

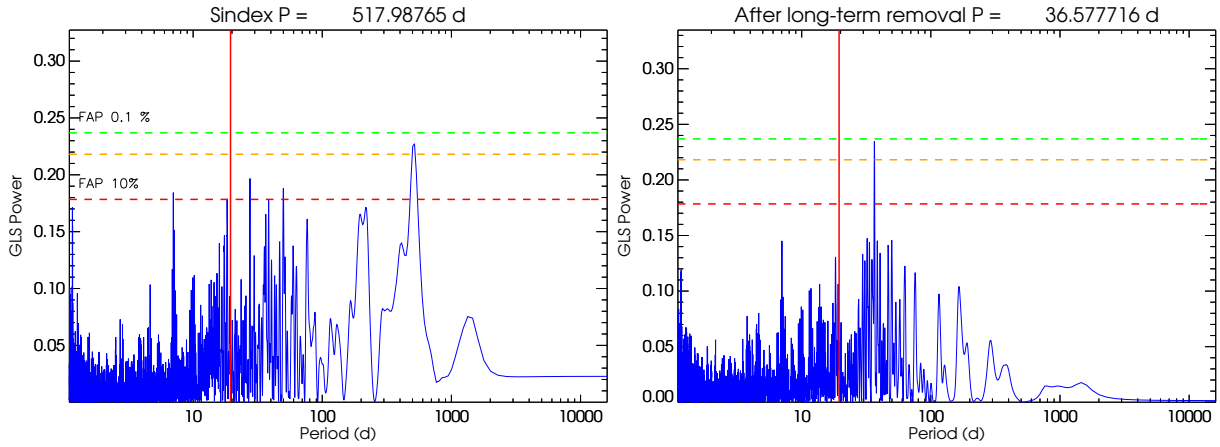

Figure 4.9: *Left panel:* GLS periodogram of S-index for GJ 720 A. The dashed lines indicate the 0.1% (green), 1% (orange) and 10% (red) level of false alarm probability. The vertical red line corresponds to the period found in RV at 19.49 days. *Right panel:* GLS periodogram of S-index after removing the signal at 518 days. The highest peak found (36.58 ± 0.1 days) is consistent with the rotation period also established ($P_{\rm rot} = 34.5 \pm 4.7$ days) by Suárez Mascareño et al. (A&A, in press).

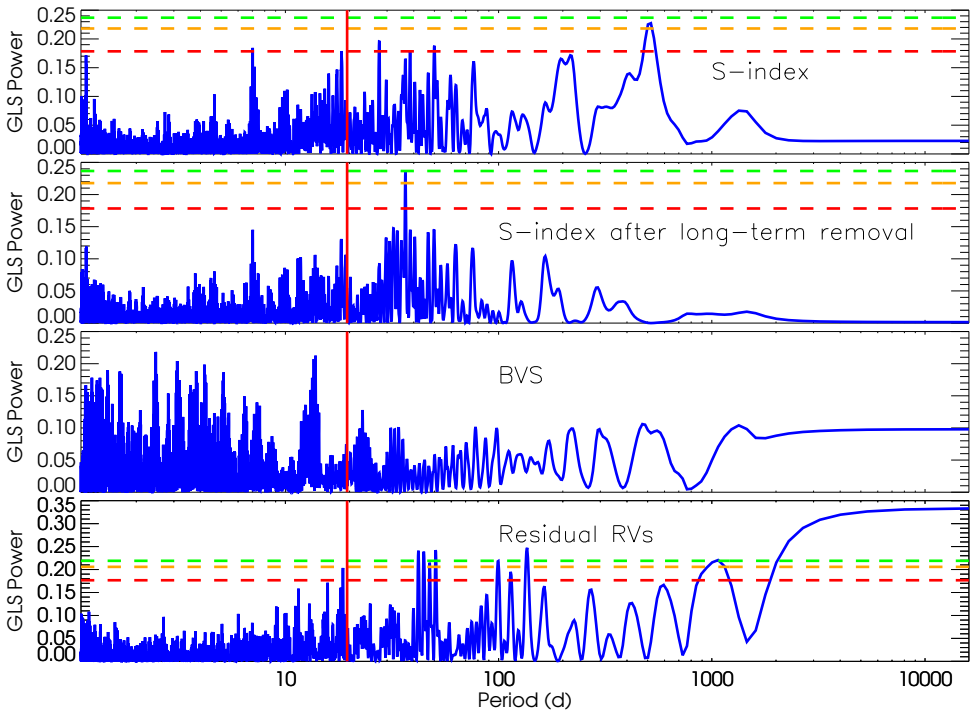

Figure 4.10: GLS periodograms of S-index before and after removing the long-term variability, BVS and residual RV for GJ 720 A. The vertical red line corresponds to the period found in RV at 19.49 days. The dashed lines indicate the 0.1% (green), 1% (orange) and 10% (red) level of false alarm probability.

We make use again of the stacked periodograms in Fig. 4.11 using the S-index activity indicator. As explain before the RV case (see Fig. 4.4) shows after 55 observation a clear, significant and narrow period at 19 days. The S-index after removing the long-term signal at 518 days (Figure 4.11) shows a signal around 36-38 days which increases its significance with increasing the number of observations until a number of 95 observations. After that, the power starts to decrease. This signal clearly corresponds with the stellar rotation period found at 36 days as seen and explained in Figure 4.9. Another important thing to note in Figure 4.11 is that around 19 days (RV main period) there is a residual periodic signal that loss significance after 70 observations.

This argument complicates the hypothesis of a planetary companion at 19 days because it could be possible that our candidate orbital period will be related with some activity effect

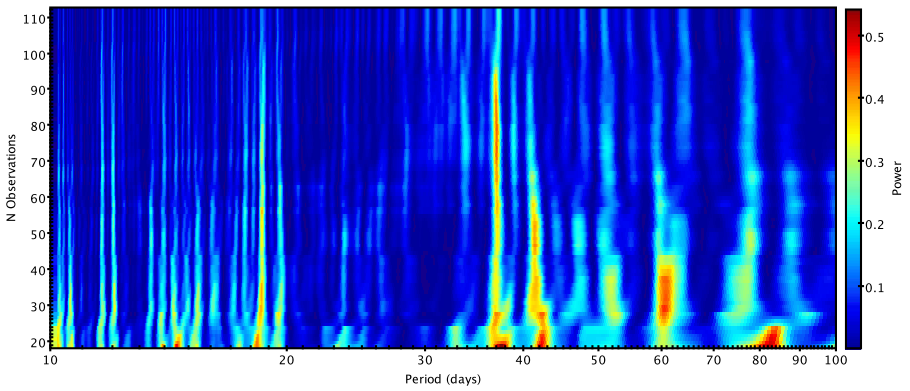

Figure 4.11: Zoom-in (10 to 100 days) of stacked periodograms of the S-index data after remove long-term signal at 518 days for GJ 720 A.

coupled to stellar rotation period.

4.1.4 Summary

GJ 720 A, presents an interesting high significant periodic signal suggesting the presence of a companion. In order to definitively conclude on the presence of a substellar companion in the future we need to perform further analysis such as to study the photometric light-curve or perform a Gaussian processes analysis. Assuming the planetary hypothesis as responsible of the signal found at 19.48 days, the best orbital parameters for the possible planet are summarized in Table 4.2. Our supposed planet would have a minimum mass around 13 $M_{\oplus}$ at a distance of 0.12 ± 0.004 AU from the host star with an orbital period of 19.487 ± 0.008 days. In Figure 4.12 we represent the position occupied by our candidate planet in the diagram of known Neptune-type and Super-Earth planets around M dwarfs. The planet would cover an interesting region poorly populated by Super-Earths corresponding to a gap in the minimum mass range between 15 to 25 $M_{\oplus}$ and orbital periods between 6 to 20 days. Other tests will be needed to understand if the period found at 19 days in RV could be related with some activity effects and confirm or dismiss the planetary hypothesis.

Table 4.2: Best fit orbital parameters for GJ 720 A

Parameter	Units	Value
P	Period (days)	19.487 ± 0.008
T_P	Periastron time (JD-2,400,000)	57244.36 ± 1.34
e	Eccentricity	0.16 ± 0.06
ω_*	Argument of periastron (deg) .	99.35 ± 25.99
K	RV semi-amplitude (m/s)	4.67 ± 0.31
γ	Systemic velocity (m/s)	0.24 ± 0.21
$M_P \sin i$ ..	Minimum mass (M_J)	0.042 ± 0.003
a	Semi-major axis (AU)	0.118 ± 0.004

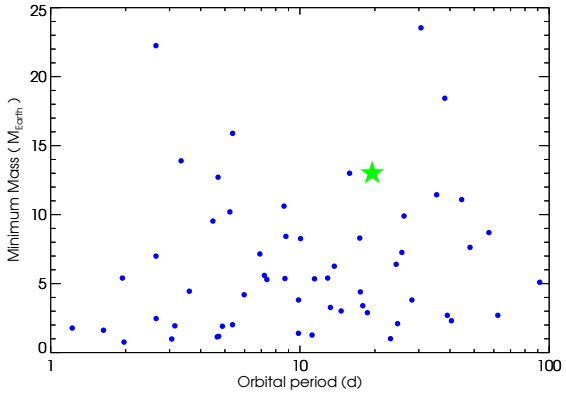

Figure 4.12: Minimum mass vs. orbital period diagram for known Neptune-type and Super-Earth planets around M dwarfs (http://www.exoplanet.eu). The green star indicates the location of our candidate planet around GJ 720 A

4.2 Search for planets around GJ 521 A

In this section we discuss the analysis of GJ 521 A, a M1.5 dwarf located at a distance of 13.00 ± 0.27 pc (Lépine & Gaidos 2011). The basic stellar parameters, reported in Table 4.3, were computed making use of the spectra used in RV analysis, as for the rest of stars in our sample, and following the procedure described in Maldonado et al. (2015a).

GJ 521 A has been monitored from the 24th of March 2013 to the 3rd of August 2017 obtaining a total of 143 data points. This target is a good candidate to show the possible difficulties that can be found when the RV analysis is made. The 82 collected data until August 2016 were pointing to a periodic RV variation at about 18 days at a high significant

Table 4.3: Stellar parameters of GJ 521 A derived in this work.

Parameters	Value
α (J2000)	13:39:24.1022
δ (J2000)	+46:11:11.363
V [mag]	10.24
d (pc)	13.00 ± 0.27
Derived from HARPS-N spectra	
$T_{\rm eff}$ (K)	3601 ± 68
log g (dex)	4.79 ± 0.04
[Fe/H] (dex)	-0.09 ± 0.09
$v \sin i$ (km s^{-1})	0.91
P_{rot} (days)	34.5 ± 4.7
Mass ($M_\odot$)	0.47 ± 0.05
Radius ($R_\odot$)	0.47 ± 0.05
log $L/L_\odot$	-1.486 ± 0.094

level (left panel Fig. 4.13). With the aim to understand better the origin of the signal we decided to continue the monitoring of this target until August 2017. At the end of the observations, with a total of 143 data points, our periodic variation at 18 days had disappeared with an important decrement of its significancy (right panel Fig. 4.13).

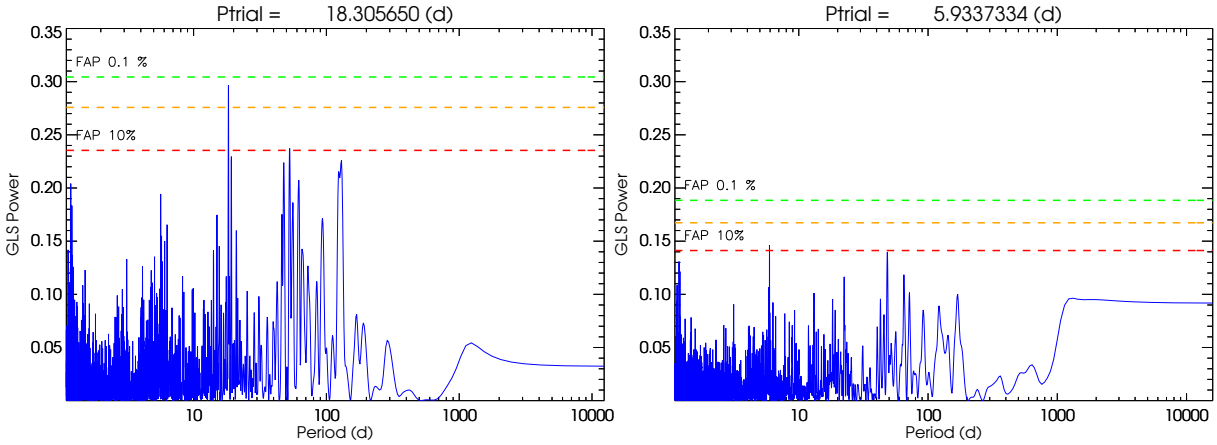

Figure 4.13: *Left panel:* GLS periodogram for GJ 521 A with 82 data points (until August 2016). The significant peak is around 18 days. *Right panel:* GLS periodogram for a total of 143 data points (until August 2017). The significant periodic variation at 18 days has disappeared.

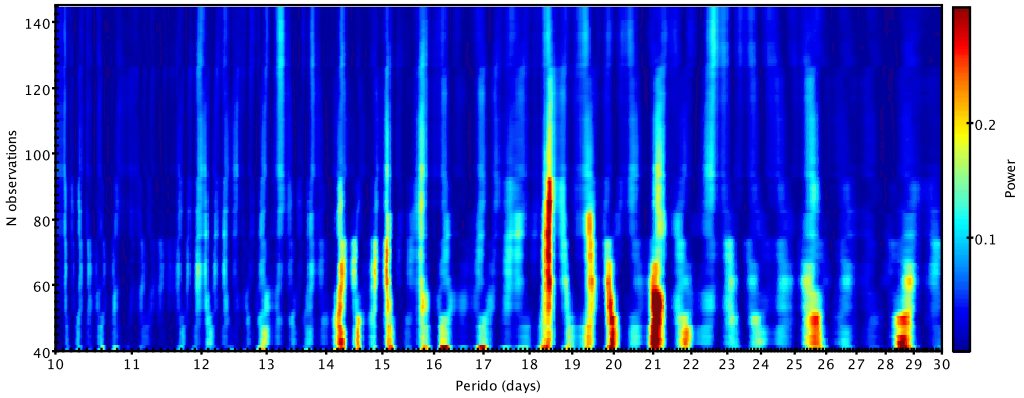

Figure 4.14: Zoom-in of stacked periodogram of RV as a function of the period for GJ 521 A between 10-30 days.

Using the cumulative GLS, increasing the number of observations to study the stability of the peaks and making a zoom-in around 18 days, we appreciate in Figure 4.14 the complexity of this target with many periodic signals whose cumulative power have decreased as we added more observations and finally resulting with no significant periodic signals at the end of the observations.

In Figure 4.15 the spectral window function analysis does not reveal new helpful or clarifying information showing a high number of possible aliasing phenomena that must be analysed. The study of S-index activity indicator reveals in Figure. 4.16 a clear and unique periodicity at 47.3 ± 0.2 days consistent with the rotation period of the star (49.5 ± 3.5 days) identified by Suárez Mascareño et al. (A&A, in press) using the same technique.

In this case we are not sure on how the first signal found at 18 days with a large number of observations done could rapidly decrease and how this effect can be related with the stellar activity. The most probable hypothesis is that the RV periodic signal was due to some features on the stellar surface that was evolving in time. But if our hypothesis is correct it is unclear why the signal at 18 days is not apparently linked with some aliasing phenomena due to rotation period of the star.

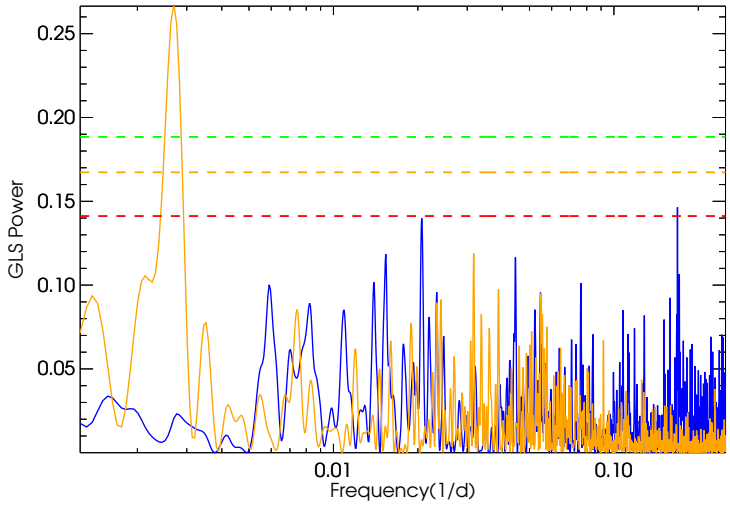

Figure 4.15: Spectral window function for GJ 521 A (orange line) and RV GLS periodogram (blue line). The dash coloured lines represent the false alarm probability of 0.1% (green), 1% (orange) and 10% (red).

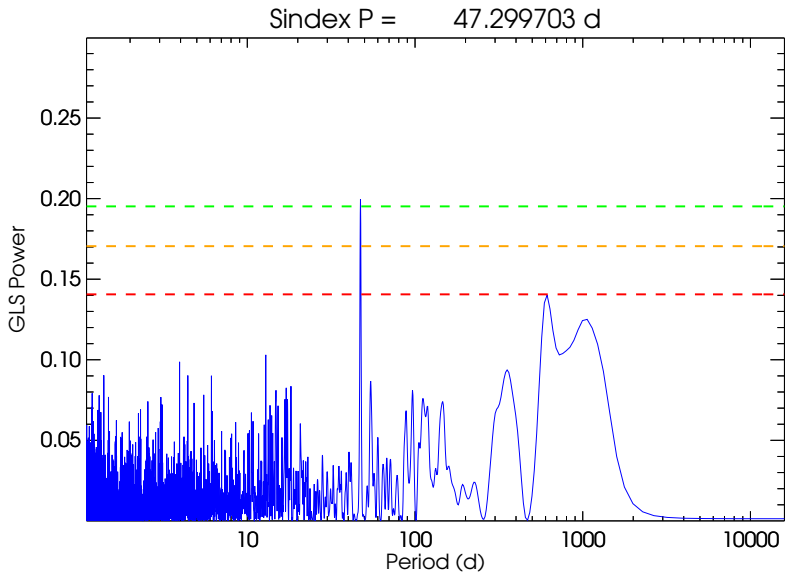

Figure 4.16: GLS periodogram of the S-index for GJ 521 A. The dash coloured lines represent the false alarm probability of 0.1% (green), 1% (orange) and 10% (red).

4.3 Conclusions

GJ 720 A presents an interesting significant periodic variation in radial velocity pointing to a keplerian origin. We note that before we can make a solid conclusion, it will be necessary the study of the photometric light-curve or/and Gaussian processes analysis. However, assuming the companion hypothesis we obtained the best Keplerian fit and derived the orbital parameters. The possible planet around GJ 720 A would have a minimum mass of 13 $M_{\oplus}$ and orbital period of 19.487 ± 0.008 days covering the existing gap on Super-Earth and Neptune-type discovered planets around M dwarfs.

On the other hand the analysis of GJ 521 A shows some of the problems that arise in the RV study of low-mass stars. In this case we had a promising periodic signal where at first it did not look like related with any activity effect but adding new observations it disappeared rapidly. It is possible that we are dealing with some kind of stellar activity but until now we can conclude nothing relevant for GJ 521 A. A new observing strategy will be needed to study it.

Chapter 5

Optical-Infrared simultaneous radial velocity measurements

5.1 A substellar companion around K giant star: TYC 4282-605-1

5.1.1 Introduction

Several physical mechanisms related to the host star characteristics may mimic the presence of a planet. They include granulation and activity phenomena such as spots, plagues and even cycles as well as radial and non-radial pulsations (Hatzes & Cochran 2000). These phenomena may occur on several time scales and produce radial velocity (RV) variations hardly distinguishable from those induced by a low-mass companion.

The K giant stars usually have masses in the 0.2-10 $M_{\odot}$ mass range and radii between 2 and 100 $R_{\odot}$. Their precise evolutionary stage is difficult to determine because the evolutionary tracks of the stars belonging to the red giant branch, red clump (for solar metallicity) and asymptotic giant branch fall close and can intersect with each other in the H-R diagram (Chaplin & Miglio 2013).

The variability of these objects can be quite complex. Luminous red-giants are known to exhibit regular and semi-regular light curves, with periods of tens and hundreds of days, and additional long-term modulations not yet fully understood (Wood et al. 2004). Several mechanisms have been suggested, such as rotational modulation, additional pressure or gravity pulsation modes, mass loss effects induced by companions, amongst others. The

space mission *CoRoT* disclosed the huge asteroseismic potential of G-K giants: the regular patterns due to solar-like oscillations and the progressive shift of frequency of maximum oscillation power were both observed (De Ridder et al. 2009). Further detailed investigations of the pulsational properties allowed asteroseismologists to investigate the internal stellar structure (see Chaplin & Miglio 2013; Hekker & Christensen-Dalsgaard 2016, for reviews).

Surface features and non-radial pulsations are expected to produce changes in the shape of the spectral line profile which can be misinterpreted with velocity shifts. These changes can be measured using spectral line bisectors that are correlated with RV in case of distortion of the lines. The measurements of the bisector require very high resolution spectra and a stable instrument. The absence of variations in the spectral line shape is a necessary condition but it is not sufficient to prove the existence of planetary companion.

Photometric observations are useful to understand the long-period RV variations as they constitute an independent measure of the time scales of rotation and pulsation periods. Photometric variability on the same time scale of the RV variations would immediately exclude the planetary companion hypothesis. Photometric analysis, together with the monitoring of the Ca II H and K lines (measured using the same spectra as to derive RVs) and bisector analysis are very helpful to reject the companion hypothesis and should always be used when possible.

As mentioned before, the pulsations in K giants are excited by p-modes spanning a large interval of periods. The amplitudes of the RV variations are expected to show an atmospheric gradient as it happens for Cepheids (see Fig. 7 in Nardetto et al. 2017). The processes of stellar origin are chromatic, therefore measurements of the RV in more than one spectral band may be helpful to discriminate the origin (stellar or keplerian) of the observed variations. Pulsations cause light variations, and in this case the photometric amplitudes are also different at visible and infrared wavelengths (Percy et al. 2001).

A similar behaviour is expected in the case of activity, where the variations are due to the difference of temperature between the unperturbed photosphere and the spot. On the contrary the planetary signal is independent from the spectral band, therefore the comparison of the RV amplitude variations in the two bands may provide an effective way to discriminate stellar and keplerian variations.

We present the analysis of the RV variations of the giant star TYC 4282-605-1 observed with HARPS-N at the TNG. These observations were obtained within the Global Architecture of Planetary Systems (GAPS, see Covino et al. 2013) observing programme. The GAPS programme started its operations in August 2012 taking advantage of the high performance

of the HARPS-N spectrograph (Cosentino et al. 2012), mounted at the Italian telescope TNG in La Palma, Canary Islands.

The observations showed a periodic signal in RV that could be attributed to a planet. Since we cannot exclude a possible alternative explanation, we acquired additional data in the near infrared (NIR) with the GIANO spectrograph (Oliva et al. 2006) at the TNG, to obtain quasi-simultaneous observations in optical and NIR to discriminate between a stellar and keplerian origin of the periodicity observed in the optical band.

In Sects. 5.1.2 and 5.1.3 we derive the stellar parameters and discuss the chemical analysis, respectively. Sections 5.1.4 and 5.1.5 describe the observations with HARPS-N, the RV analysis of the collected spectra, the effects of the stellar contribution to RV variation through the study of the bisector as asymmetry indicator and finally the chromospheric emission from Ca II H and K lines. Section 5.1.6 describes the photometric analysis. Our methods of extracting the RV in NIR are given in Sect. 5.1.7 together with observations, data reduction of the GIANO spectrograph and the consistency between optical and NIR data. Finally, the conclusions are presented in Sect. 5.1.9.

The content of this chapter has been the subject of the paper: The GAPS Programme with HARPS-N at TNG. XV. A substellar companion around a K giant star identified with quasi-simultaneous HARPS-N and GIANO measurements, published in A&A by González-Álvarez et al. (2017).

5.1.2 Stellar properties

TYC 4282-605-1 is a K giant star with a visible magnitude of V=10.581 ± 0.01 mag (stellar parameters from literature are summarised in Table 5.1) misclassified as an M star in Lépine & Gaidos (2011) and for this reason it was included in the original M stars sample in the GAPS programme. The first collected spectra showed soon its earlier type and low gravity. Notwithstanding that the star was misclassified, we decided to continue monitoring this target because of the large variations of RV observed in the first few observations.

Our HARPS-N data (see Sect. 5.1.4) were used to determine the stellar parameters through the higher signal-to-noise ratio (S/N) co-added spectrum with a value of ~ 400 at 5500 Å. Our analysis yielded a temperature of $T_{\rm eff} = 4300 \pm 50$ K, a surface gravity $\log g = 2.0 \pm 0.2$ dex, a micro-turbulent velocity $\xi = 1.19 \pm 0.2$ km s^{-1} and an iron abundance of [Fe/H] $= -0.07 \pm 0.16$ dex with a method based on measurements of equivalent widths (EWs) that relies on the excitation and ionisation equilibria of Fe lines, explained accurately

Table 5.1: Stellar parameters of TYC 4282-605-1 from literature.

Parameters	Value
α (J2000)	22 55 29.2581$^{(a)}$
δ (J2000)	+62 14 20.849$^{(a)}$
B [mag]	$12.105 \pm 0.01^{(a)}$
V [mag]	$10.58 \pm 0.01^{(a)}$
B-V [mag]	1.52 ± 0.01
J [mag]	$7.667 \pm 0.023^{(b)}$
H [mag]	$6.963 \pm 0.033^{(b)}$
K [mag]	$6.778 \pm 0.021^{(b)}$
μ_α [mas/yr]	$44.2 \pm 3.5^{(c)}$
μ_β [mas/yr]	$6.8 \pm 3.5^{(c)}$
U_{LSR} [km s^{-1}]	$-154.4 \pm 50.4^{(d)}$
V_{LSR} [km s^{-1}]	$-63.0 \pm 17.9^{(d)}$
W_{LSR} [km s^{-1}]	$-48.5 \pm 19.0^{(d)}$

$^{(a)}$ Zacharias et al. (2012); $^{(b)}$ Cutri et al. (2003); $^{(c)}$ Høg et al. (2000); $^{(d)}$ This work (see text)

in Sect. 5.1.3.

To measure the projected rotational velocity ($v \sin i$), we performed a spectral synthesis using the *synth* driver within MOOG code (version 2014, Sneden 1973) and fixing the stellar parameters ($T_{\rm eff}$, $\log g$, ξ) at the values derived through the EWs method. We followed the prescriptions given by D'Orazi et al. (2011), and fixed the macroturbulence velocity to the value derived from the relation by Valenti & Fischer (2005). Further details on the procedure of spectral synthesis are given in other works within the GAPS project (see, e.g. Covino et al. 2013; Damasso et al. 2015; Esposito et al. 2014). The resulting $v \sin i$ is reported in Table 5.2.

For the estimation of the stellar mass, radius, luminosity and age (listed in Table 5.2) we used the isochrones by Bressan et al. (2012) shown in Fig. 5.1. From the spectroscopic parameters ($T_{\rm eff}$ and $\log g$) extracted in this work we identified the evolutionary track followed by TYC 4282-605-1, classifying this object as a 10.1 Gyr star, being therefore an old giant star with mass $0.97 \pm 0.03 M_\odot$.

Thanks to the empirical calibration of $T_{\rm eff}$ versus colour and [Fe/H] of giant stars proposed by Alonso et al. (1999) we obtained the bolometric correction ($BC(\rm V) = -0.636 \pm 0.003$, as a function of $T_{\rm eff}$ and [Fe/H]) and the colour excess ($E_{\rm B-V} = 0.24 \pm 0.01$) that allowed us to

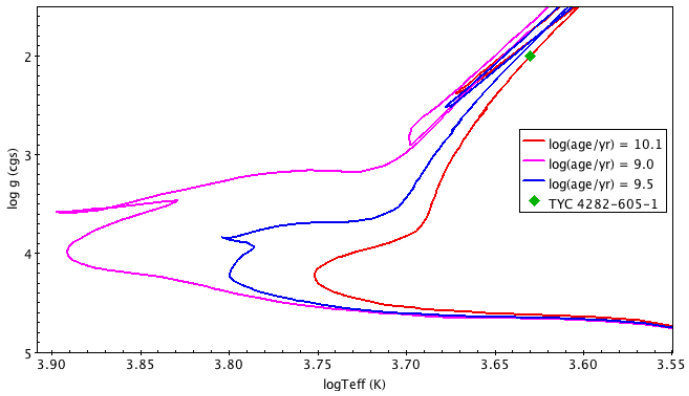

Figure 5.1: Isochrones by Bressan et al. (2012) place the target (green diamond) as an old giant star with log (age/yr) = 10.1 (red line). The estimated parameters (mass, radius, luminosity) are listed in Table. 5.2

estimate the distance of the star according to the following equations:

$$M_{bol} = M_{bol_\odot} - 2.5 \log \frac{L}{L_\odot} \quad ; \quad M_{bol_\odot} = 4.75 \tag{5.1.1}$$

$$M_{bol} = M_V + BC(V) \tag{5.1.2}$$

$$M_V = m_V + 5 - 5 \log d \text{ (pc)} - \mathrm{A_V} \tag{5.1.3}$$

where the total extinction, A_V, is defined as $A_\mathrm{V} = 3.1 \times E_{B-V}$, M_V is the absolute magnitude in V band, $m_\mathrm{V} = 10.581 \pm 0.01$ is the apparent V magnitude provided by the UCAC4 catalogue and d is the distance of the star measured in parsec. The computation yields the star at a distance of 700 ± 143 pc from the sun.

Since the star has been observed by Gaia and included in the first data release (Gaia Collaboration et al. 2016), we have computed the stellar mass using its Gaia parallax of $\pi = 2.74 \pm 0.56$ mas ($d = 364.96 \pm 74.59$ pc) using the relation $g = G\frac{M}{R^2}$ where g is measured spectroscopically and R is computed from $L = \sigma T_{eff}^4 4\pi R^2$. The resulting mass is 0.26 ± 0.15 $M_\odot$. Such low mass is unexpected for an evolved giant unless the star has lost substantial fraction of it mass. In this case we should find chemical anomalies that are not evident from our analysis (see Sect. 5.1.3).

The discrepancy of our distance with the Gaia one is at only the 2σ level, before applying the Lutz-Kelker correction (Lutz & Kelker 1973) but given the Gaia's operational distance

Table 5.2: Stellar parameters of TYC 4282-605-1 derived in this work.

Parameters	Value
Derived from HARPS-N spectra	
$T_{\rm eff}$ (K)	4300 ± 50
log g (dex)	2.0 ± 0.2
ξ (km s^{-1})	1.19 ± 0.2
[Fe/H] (dex)	-0.07 ± 0.16
$v \sin i$ (km s^{-1})	3.0 ± 0.5
Estimated from isochrones [(a)]	
Mass ($M_\odot$)	0.97 ± 0.03
Radius ($R_\odot$)	16.21 ± 4.01
log L ($L_\odot$)	1.91 ± 0.18
d (pc)	700 ± 143
Age (Gyr)	10.1 ± 0.05

[(a)] Bressan et al. (2012)

range, the Lutz-Kelker correction must be applied. The measurement of distances from trigonometric parallaxes is complicated by the existence of the Lutz-Kelker bias, which generates selection effects and also requires the use of correction factors for the distance to a given star derived from its parallax. We deprecate the Gaia's distance value and we assume a stellar distance of $d = 700 \pm 143$ pc and a stellar mass of $0.97 \pm 0.03 M_\odot$ as determined by isochrones.

5.1.3 Chemical analysis

Chemical abundance of individual elements C, Na, Mg, Al, Si, Ca, Ti, Cr, Fe, Ni, Cu, Y, Ba, and La were obtained using the MOOG code together with ATLAS9 atmosphere models (Kurucz 1993), with no overshooting. Abundances of Na, Mg, Al, Si, Ca, and Ni were obtained using lines of the neutral atoms (X I), while for Ti, Cr, and Fe we have exploited lines of both neutral and single ionised species (X II). The lines selected in the chemical analysis of these elements were taken from Maldonado et al. (2015b).

For the above mentioned species we have carried out EW analysis, using the driver *abfind* in MOOG; the ARES code (Sousa et al. 2007) has been used to measure EW values, but we have carefully double checked each single spectral feature using the task *splot* in IRAF[I].

[I]IRAF is the Image Reduction and Analysis Facility, a general purpose software system for the reduction

For C, Cu, Y, Ba and La we have instead performed spectral synthesis calculations using the driver *synth*, and including hyperfine structure and isotopic splitting, as needed. The abundance of C I has been determined by synthesing the CH band at 4300 Å using the line list by Plez (private communication), whereas for Cu we have used the line at 5782 Å, including HFS information by Steffen (1985). As for neutron-capture elements we have employed lines at 4883.68 Å and 4900.12 Å for Y II, the line at 5853.69 Å for BaII, and LaII lines at 4322.51 Å and 6390.48 Å. For details on oscillator strengths and atomic parameters for these spectral features we refer to e.g. D'Orazi et al. (2012, 2017).

The first step is the determination of the atmospheric parameters and iron abundance by means of the spectroscopic analysis, following the standard procedure. Effective temperature (T_{eff}) has been derived by zeroing the slope between abundances from Fe I lines and the excitation potential of the spectral features. Similarly, microturbulence values (ξ) has been obtained imposing no spurious trend between abundances from Fe I and the reduced EWs (that is EW/λ). The surface gravity (log$g$) comes from the ionisation balance, that is Δ[A(Fe II)− A(Fe I)]=0. The solution is reached when all the three conditions are simultaneously satisfied, better than 1σ from the error on slopes for temperature and microturbulence and better than roughly one-third the error bar in FeI and FeII features (i.e. the standard deviation from the mean). We have obtained T_{eff}=4300±50 K, log$g$=2.00±0.2 dex, ξ=1.19±0.20 km s^{-1}. By adopting these atmospheric stellar parameters we have inferred an iron abundance of A(Fe I)=7.43±0.01 (rms=0.134, 207 lines) and A(Fe II)=7.43±0.03 (rms=0.102, 15 lines).[II]

Our results are reported in Table 5.3, which includes abundances for the species under scrutiny in this study along with corresponding uncertainty. The solar abundances adopted throughout the manuscript are given in Column 2 and have been employed to derive the [X/Fe] ratios listed in Column 5.[III] Two kind of internal (random) errors affect our abundance values, that is errors due to EW measurements (or to the determination of best fit via spectral synthesis) and errors related to atmospheric parameters. For the first source of errors, assuming Gaussian statistics, the line-to-line scatter errors are computed as $\sigma/\sqrt{n}$, where σ is the standard deviation of the derived individual abundances from the n lines. For species for which only one spectral line is available (i.e., Cu and Ba) we have repeated the measurement several times by changing the continuum displacement and other criteria

and analysis of astronomical data. IRAF is written and supported by National Optical Astronomy (NOAO) observatories

[II]The derived abundances are expressed in the usual scale, $A(X) = \log(N_X/N_H) + 12$.

[III][X/Fe]=[X/H]−[Fe/H], where [X/H]=A(X)-A(X)$_\odot$.

Table 5.3: Derived abundances for TYC 4282-605-1

Ion	$\langle A(X)\rangle_{\odot}^{(1)}$	$\langle A(X)\rangle^{(1)}$	n	$[X/Fe]^{(2)}$
C I	8.43 ± 0.07	8.20 ± 0.08	1	-0.23 ± 0.15
Na I	6.38 ± 0.01	6.57 ± 0.04	3	0.26 ± 0.16
Mg I	7.62 ± 0.02	7.91 ± 0.04	2	0.36 ± 0.13
Al I	6.48 ± 0.01	6.82 ± 0.09	2	0.41 ± 0.15
Si I	7.60 ± 0.01	7.78 ± 0.03	13	0.25 ± 0.05
Ca I	6.42 ± 0.02	6.46 ± 0.03	12	0.11 ± 0.18
Ti I	5.02 ± 0.01	4.97 ± 0.02	15	0.02 ± 0.17
Ti II	5.04 ± 0.01	4.91 ± 0.05	5	-0.06 ± 0.06
Cr I	5.68 ± 0.01	5.63 ± 0.03	18	0.02 ± 0.16
Cr II	5.67 ± 0.01	5.67 ± 0.06	3	0.07 ± 0.06
Ni I	6.29 ± 0.01	6.28 ± 0.02	37	0.06 ± 0.05
Cu I	4.25 ± 0.05	4.19 ± 0.07	1	0.01 ± 0.15
Y II	2.19 ± 0.05	2.06 ± 0.04	2	-0.06 ± 0.20
Ba II	2.13 ± 0.05	2.08 ± 0.08	1	0.02 ± 0.25
La II	1.05 ± 0.04	0.97 ± 0.01	2	-0.01 ± 0.20
	$\langle A(X)\rangle_{\odot}^{(1)}$	$\langle A(X)\rangle^{(1)}$	n	$[Fe/H]^{(2)}$
Fe	7.50 ± 0.01	7.43 ± 0.02	222	-0.07 ± 0.19

$^{(1)}$ line-to-line scatter errors as $\sigma\sqrt{n}$, $^{(2)}$ final uncertainties due to the propagation of errors in stellar parameters plus the line-to-line scatter errors

and inspected the corresponding variation in the resulting abundances. In order to estimate uncertainties due to stellar parameters we have instead proceeded in the standard way, that is by varying one parameter at the time and inspecting the corresponding change in the resulting abundance. The total uncertainties for the derived abundances are then calculated by summing in quadrature line-to-line scatter errors and those related to the stellar parameters (Column 5).

Our findings point to a significant enrichment in the abundances of Na I, Mg I, Al I and Si I while Ca I, Ti I, II, Cr I, II and Ni I are consistent with the solar value. The same result holds for heavy elements (Cu I, Y II, Ba II and La II) for which we retrieve a solar-scaled abundance pattern.

To investigate the nature of the enhancement of some of the studied elements we decided to compare our results with the work by Alves-Brito et al. (2010) for a sample of giant

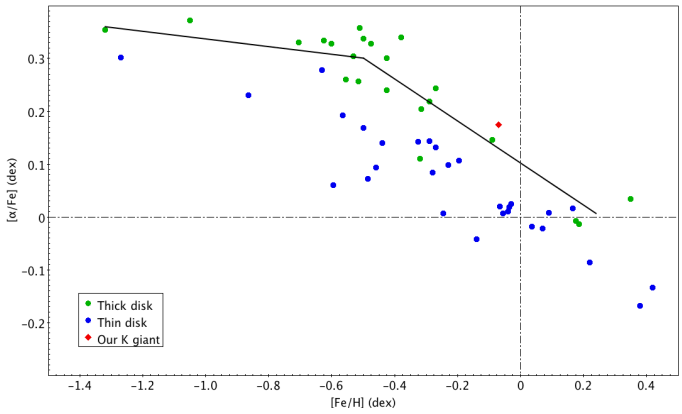

Figure 5.2: Mean α-elements abundance ratio ([O, Mg, Si, Ca, Ti/Fe]) as a function of [Fe/H] by Alves-Brito et al. (2010). The symbols are explained in the figure. The black line represents the linear fit of local thick disk star.

stars in the local disk. The authors show a chemical distinction between the local thin and thick disks stars. Their results suggest that the local thick disk stars have α-enhancements relative to solar abundances in K giants higher than those stars located in the local thin disk. As shown in Fig. 5.2 the [α/Fe] chemical pattern of TYC 4282-605-1 clearly follows the performed linear fit for [α/Fe] vs. [Fe/H] of local thick disk stars. We demonstrated thus that the chemical composition of our target supports that it is an old K giant (age = 10.1 Gyr) belonging to local thick disk.

This result is confirmed by the kinematic velocities. Calculation of the space velocity with respect to the Sun is based on the procedure presented by Johnson & Soderblom (1987), corrected for the effect of differential galactic rotation (Scheffler & Elsasser 1988), by adopting a solar Galactocentric distance of 8.5 kpc and a circular velocity of 220 km s^{-1}. The correction of space velocity to the local standard of rest is based on a solar motion, $(U, V, W)_{\odot}$ = (10.0, 5.2, 7.2) km s^{-1}, as derived from Hipparcos data by Dehnen & Binney (1998). TYC 4282-605-1 shows kinematic properties typical of the thick disk population (see. Table 5.1) following the distributions of the space velocities for the thick disk sample calculated by Bensby et al. (2004).

5.1.4 HARPS-N observations and radial velocity analysis

We collected 48 spectra of TYC 4282-605-1 with HARPS-N at TNG in the four seasons from August 2012 to November 2015. Spectra were obtained with an integration time of 900 s

and an average S/N of 70 at 5500 Å. The main characteristics of HARPS-N, very similar to HARPS at ESO, are describe in detail in chapter 2.1. In summary its main characteristics are the very high stability, the high spectral resolution of R=115,000 and the large wavelength coverage from 3800 to 6900 Å.

The reduction of the spectra and the RV measurements were obtained using the latest version (Nov. 2013) of the HARPS-N instrument Data Reduction Software (DRS) pipeline with a K5 binary mask. The measurement of the RVs is based on the weighted cross-correlation function (CCF) method (Baranne et al. 1996; Pepe et al. 2002). In Table 5.5, we list the RVs and their corresponding errors. We obtained the first three spectra with the simultaneous Th-Ar calibration lamp, while the rest of the spectra, obtained with a new charge-coupled device (CCD) after the failure of the previous one, were collected with the sky background in the second fiber. We have verified that our results do not change considering or excluding the first three data points, and that a systematic correction offset is not needed. The RV measurements for the four seasons are shown in Fig. 5.3 after removal of median RV. They have a standard deviation of 337.5 ms^{-1} much more larger than the

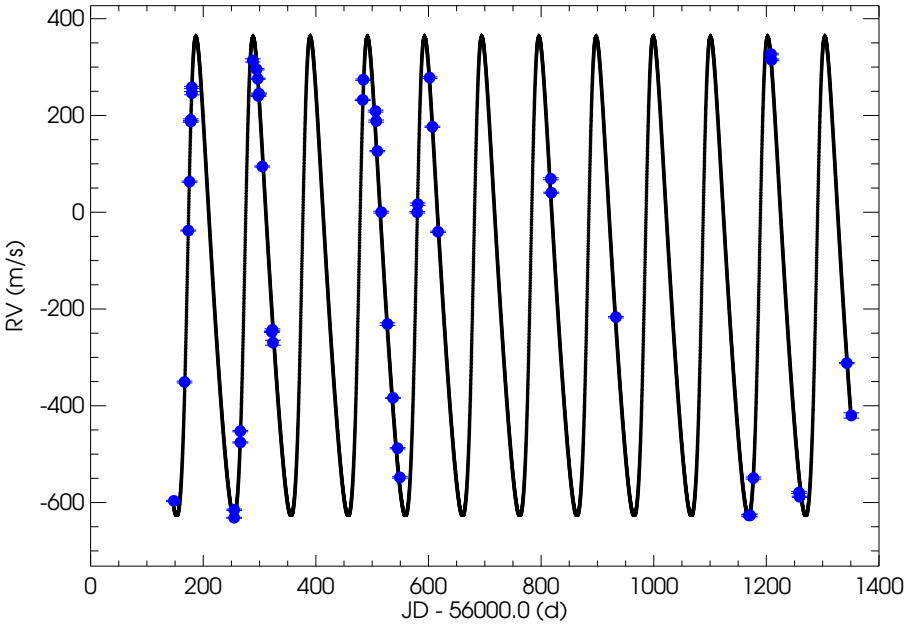

Figure 5.3: Radial velocity measurements from the four observing seasons with HARPS-N (blue dots). Removal of median of RV has been applied to the data set before plotting. The curve represents the orbital solution (see Table 5.4).

average error (1.8 ms^{-1}), pointing to an intrinsic variability.

To detect a possible periodic signal in our data we used the Generalized Lomb-Scargle periodogram (GLS, Zechmeister & Kürster 2009), which is the most common method in case of unevenly spaced times and it is characterised by a simple statical behaviour. The GLS periodogram allows us to identify significant periods in the data which can be used as starting estimates for the algorithm if their amount of power is higher than the chosen confidence level.

The GLS periodogram reveals a clear periodicity with a highly significant peak at period $P = 101.54$ days in the top panel of Fig. 5.4 with a power much higher than the lowest false alarm probability (FAP) fixed at 0.1% (green line) and estimated through a bootstrap method with 10,000 iterations. To verify the presence of possible aliasing phenomenon, we plot the window function in Fig. 5.5 showing that the strong peak around 101 days, corresponding to 0.01 $days^{-1}$ in the domain of frequencies, is not related with a periodicity in the sampling.

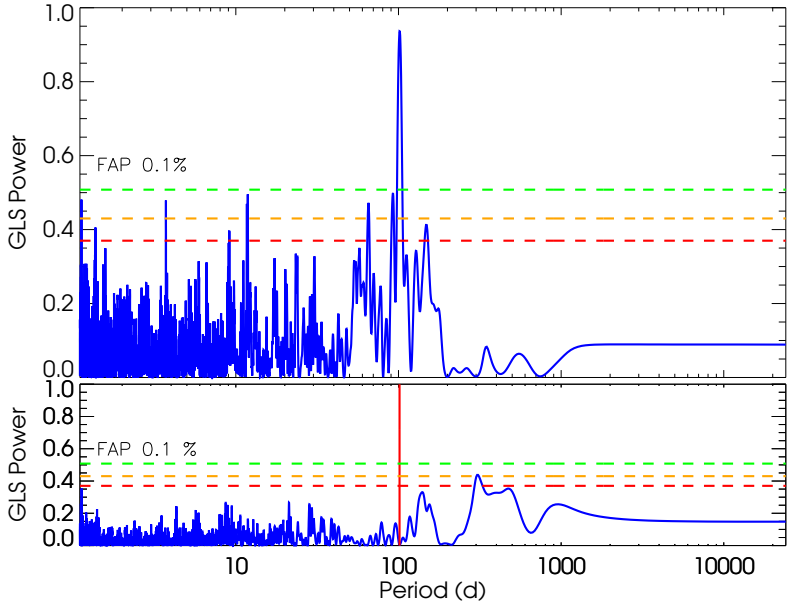

Figure 5.4: *Top panel:* GLS periodogram of RVs measured with HARPS-N with a significant peak at 101.54 days, the horizontal dashed lines represent the false alarm probabilities (FAP) of 0.1% (green line), 1% (orange) and 10% (red), respectively. *Bottom panel:* Periodogram of the residuals data after subtracting the orbital fit. The red solid line indicates the location of the maximum period found with the RV.

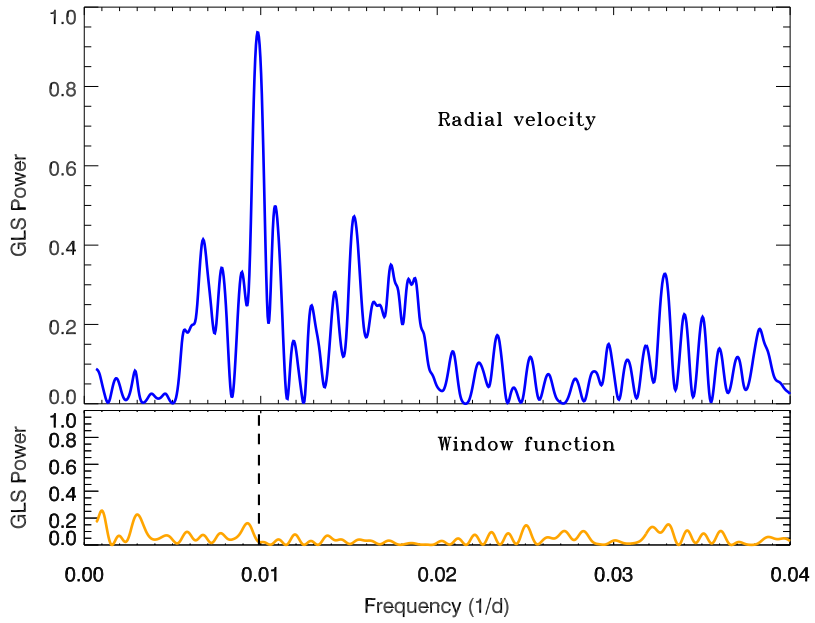

Figure 5.5: GLS periodogram expressed in frequency of the TYC 4282-605-1 RVs (upper panel) and the corresponding window function (lower panel). The strong peak found around 101 days corresponds with the value in frequency of 0.01 days^{-1}.

Assuming the companion hypothesis we used the RVLIN code [IV] (see Wright & Howard 2009) to obtain the best Keplerian fit and derive the orbital parameters listed in Table 5.4. The orbital solution and RV data are presented in Fig. 5.3 as a function of the time.

In order to analyse the residuals data we use the orbital fit to remove the period and its harmonics simultaneously. The periodogram of the residuals (bottom panel of Fig. 5.4) does not show other significant peaks, but a marginal long term signal between 300-500 days is present. The RV and residuals measurements (rms = 23.02 ms^{-1}) phase-folded are shown in Fig. 5.6. Our solution resulted in a semi-amplitude, $K_{\rm opt} = 495.2 \pm 5.1$ ms^{-1}, eccentricity, $e = 0.28 \pm 0.01$, semi-major axis, $a = 0.422 \pm 0.009$ AU and a minimum mass for the companion, $M_P \sin i = 10.78 \pm 0.12$ $M_{\rm J}$, assuming the stellar mass of 0.97 ± 0.03 $M_\odot$ previously derived. We estimated the errors of the derived orbital parameters (reported in Table 5.4) through a bootstrap (10,000 re-sampling) analysis.

[IV] The code is available at http://exoplanets.org/code/

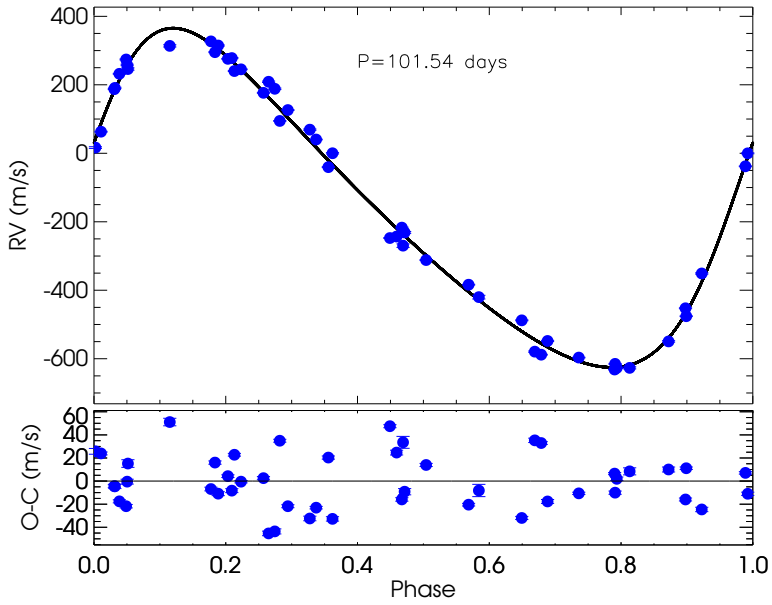

Figure 5.6: *Top panel:* Radial velocity data of the four observing seasons of HARPS-N phased to the correspond orbital period. The solid line is the orbital solution. *Bottom panel:* Residual RV variations after subtracting the orbital solution. The residuals show a standard deviation value of 23.02 ms^{-1}.

Table 5.4: Best fit orbital parameters

Parameter	Units	Value
P	Period (days)	101.54 ± 0.05
T_P	Periastron time (JD-2,400,000)	56479.28 ± 0.57
e	Eccentricity	0.28 ± 0.01
ω_*	Argument of periastron (deg) .	288.94 ± 2.38
K	RV semi-amplitude (m/s)	495.2 ± 5.1
γ	Systemic velocity (m/s)	$-12,361.54 \pm 3.58$
$M_P \sin i$ ..	Minimum mass ($\mathrm{M_J}$)	10.78 ± 0.12
a	Semi-major axis (AU)	0.422 ± 0.009

Table 5.5: Measurements of radial velocity with HARPS-N

Epoch [JD]	RV [kms^{-1}]	error [kms^{-1}]
56147.839	-12.784	0.001

Table 5.5: Measurements of radial velocity with HARPS-N (continue)

Epoch [JD]	RV [kms^{-1}]	error [kms^{-1}]
56166.789	-12.538	0.002
56173.522	-12.225	0.001
56175.743	-12.124	0.001
56177.793	-12.000	0.001
56177.875	-11.996	0.002
56179.774	-11.929	0.002
56179.888	-11.941	0.003
56254.898	-12.819	0.001
56254.972	-12.802	0.001
56265.822	-12.640	0.001
56265.943	-12.663	0.001
56287.877	-11.873	0.003
56294.842	-11.892	0.001
56296.838	-11.911	0.001
56297.838	-11.947	0.001
56298.862	-11.942	0.001
56304.837	-12.093	0.001
56321.813	-12.435	0.001
56322.841	-12.430	0.002
56323.836	-12.457	0.005
56483.194	-11.955	0.001
56484.233	-11.913	0.001
56506.194	-11.978	0.002
56507.145	-11.999	0.002
56509.159	-12.061	0.001
56516.042	-12.187	0.002
56527.155	-12.418	0.003
56537.019	-12.571	0.001
56545.210	-12.675	0.001
56549.192	-12.735	0.002
56580.046	-12.187	0.001
56581.044	-12.170	0.003

Table 5.5: Measurements of radial velocity with HARPS-N (continue)

Epoch [JD]	RV [kms^{-1}]	error [kms^{-1}]
56602.066	-11.909	0.002
56606.945	-12.011	0.001
56616.947	-12.228	0.001
56817.168	-12.118	0.002
56818.143	-12.147	0.001
56932.895	-12.404	0.002
57169.103	-12.814	0.002
57171.085	-12.814	0.003
57177.087	-12.737	0.002
57208.095	-11.860	0.002
57209.211	-11.872	0.002
57258.008	-12.766	0.002
57258.998	-12.775	0.001
57342.797	-12.499	0.001
57350.926	-12.607	0.005

5.1.4.1 Bisector analysis

Stellar activity and pulsations can cause deformations in the line profile of the spectral lines producing a shift of the centroid of the line. This effect can be quantified by several asymmetry indicators, including the bisector. In presence of surface inhomogeneities or surface deformations we expect some (anti) correlation between RV and the CCF bisector velocity span (BVS). The top panel of Fig. 5.7 shows the BVS as a function of the RV measurements. No significant correlation was found with Spearman's correlation coefficient of $\rho = -0.17$. The bottom panel of the same figure shows the correlation between BVS and RV residuals having a value of $\rho = 0.47$. In Fig. 5.9 (middle panel) the GLS periodogram of the BVS is shown and no significant peak is found at the 101 days period, indicating that the modulation found in the RV is probably not connected to stellar activity or pulsations. That instead may be responsible for the long term (> 300 days) signal and for the correlation between BVS and RV residuals likely related to the stellar rotation. The lack of a correlation

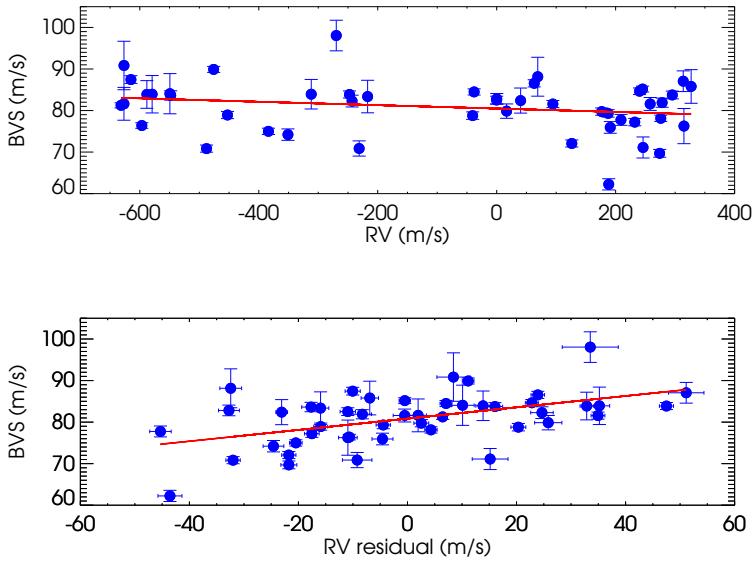

Figure 5.7: Bisector velocity span (BVS) versus RV measurements (top panel) and versus residuals of RV (bottom panel).

of the 101 days signal does not imply necessarily the presence of a companion as the origin of the RV periodicity but it is a necessary condition.

5.1.5 Chromospheric emission, S-index

Stellar activity can produce RV variations and create a signal that could be misinterpreted as an exoplanet. Some apparent RV offsets are related to the magnetic activity of the star and surface features such as spots. Also, the convection patterns of the stellar surface can suffer local or global changes due to the magnetic activity. When a star has a large convection layer hotter and bluer material can emerge from its convection cells (e.g. stellar granulation) and it causes apparent blueshifts to the integrated stellar spectrum (Anglada-Escudé & Butler 2012). For these reasons, one could expect apparent RV jitter whenever the magnetic field of the star experiences changes. One way to disentangle the effects of activity is to measure activity indicators such as the Mount Wilson S-index (Noyes et al. 1984). This index measures the relative flux of the Ca II H and K lines in emission ($\lambda_{\rm K}$ = 3933.664 and $\lambda_{\rm H}$ = 3968.470) compared with a local continuum (e.g. Lovis et al. 2011). These lines in emission are formed in the hot plasma of the chromospheres of stars, and

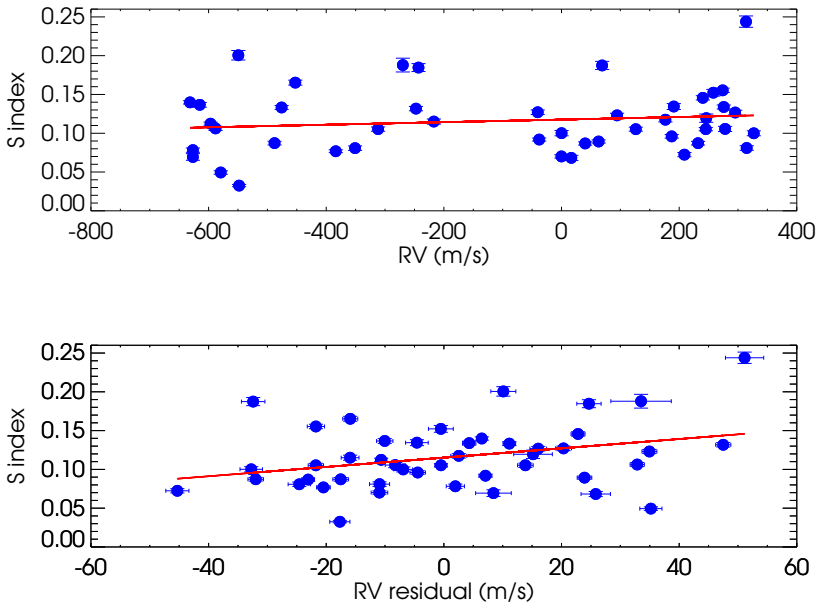

Figure 5.8: Correlation between RV (top panel) and RV residual (bottom panel) with S-index.

their intensity varies with the strength of the stellar magnetic field.

The width of the chromospheric lines in giant stars is larger than in main-sequence stars because of the Wilson-Bappu effect (e.g. Linsky 1980; Park et al. 2013). Nevertheless, their width can still be sensitive to the activity level of the star, that is, to the level of non-thermal heating of its chromosphere, as found by Elgaroy et al. (1997). Therefore, we shall use the chromospheric S-index to look for a possible correlation with the RV variation that can indicate activity as the physical cause of the observed RV modulation, although the sensitivity of the method is lower than in the case of main-sequence stars. We checked that the band passes defined by Lovis et al. (2011) for main-sequence star are adequate for our giant and we used HARPS-TERRA (Template-Enhanced Radial velocity Re-analysis Application) software (Anglada-Escudé & Butler 2012) that incorporates the automatic measurements of the S-index and its corresponding errors using the necessary information provided by the HARPS DRS.

This analysis give us another argument in favour of the companion interpretation at 101 days as shown in Fig. 5.8 through the low Spearman correlation coefficient between the S index with RV ($\rho = 0.15$, in the top panel) and with the RV residuals ($\rho = 0.29$, middle panel), respectively. Figure 5.9 (top panel) shows the GLS periodograms for S index,

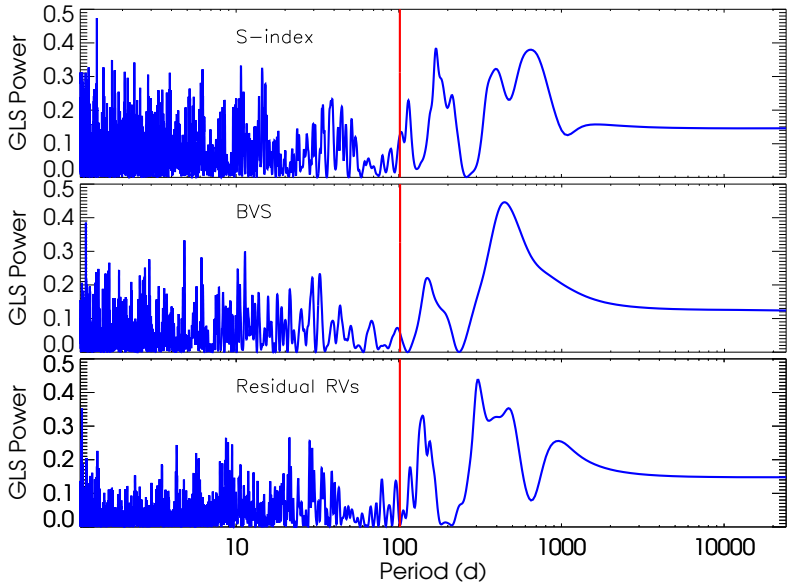

Figure 5.9: GLS Periodograms of S index, BVS and residual RV. There is no significant period at 101 days (red line).

BVS (middle) and residual RVs (bottom) in order to check that there is not activity effects correlated at 101 days. As a result, the activity has been excluded as being responsible of the significant signal found in optical band.

5.1.5.1 The case of a pulsating star

The physical parameters listed in Table 5.2 and the RV curve shown in Fig. 5.6 suggest the possibility that TYC 4282-605-1 is a pulsating star. Therefore, we must discuss it on the basis of what reported in Sect. 5.1.1.

We note that the RV curve has a reverse shape of that expected from a radial pulsation mode (see Fig. 2 in Nardetto et al. 2017, for a close comparison with the RV curve of δ Cep).

A rising branch steeper than the descending one in the RV curve implies a descending branch steeper than the rising one in the photometric light curve, but such a shape is not very common in pulsating stars. These light curves seem to be confined to few unusual cases, like V1719 Cyg stars. However, these variables show only slight asymmetric RV curves (see Fig. 3 in Poretti & Antonello 1988) and therefore the RV curve of TYC 4282-605-1 would be unique.

The line profiles have also to change during pulsation, to reflect the outward and inward motion of the atmosphere (see Fig. 1 in Nardetto et al. 2017). In particular, variations of the full-width half-maximum (FWHM) and of the bisector span values are expected over the pulsation period. No periodicity has been observed in the bisector spans of TYC 4282-605-1 (Fig. 5.9). We also analyzed the FWHM values and we did not find any variability as well.

Therefore, the detailed analysis of the HARPS-N spectra does not support pulsation as the cause of the RV curve shown in Fig. 5.6 upper panel. On the other hand, the scatter observed in the residuals (Fig. 5.6, lower panel) could be due to solar-like oscillations and/or granulation effects (Kjeldsen & Bedding 2011). For comparative purposes, solar-like oscillations are visible with an amplitude up to 60 $\mathrm{m\,s^{-1}}$ and apparent periodicity around 1 d in HD 170053, a red giant very similar to TYC 4282-605-1 (Poretti et al. 2015). Unfortunately, the time sampling of the HARPS-N spectra of TYC 4282-605-1 is not suitable for detecting amplitude and time scale of such short-period oscillations.

5.1.6 Photometric analysis

Any detected photometric variability on the same time scale of the RV variations makes the companion hypothesis questionable (Hatzes 2002). We checked for evidence of a P ∼100 days periodicity in the light curve obtained by the APACHE survey (A PAthway to the Characterization of Habitable Earths, Sozzetti et al. 2013). More than 6350 photometric points in standard Cousin I-band have been collected over three observing seasons between 2012 and 2014, with the time span covering a total of 782 days. The differential light curve was derived by using UCAC4 762-068173, 761-069159, 761-069142 and 762-068154 as comparison stars. For the present analysis we have considered the nightly mean values of the total light curve assuming the standard deviation of the mean as the uncertainty for each binned value. We discarded four nights over a total of 109 because of the photometry scarce quality resulting in errors larger than 0.02 mag. We calculate the GLS periodogram in the frequency range 0.00125-0.1 $\mathrm{d^{-1}}$ (10-800 days) to search for possible periodic modulation, limiting our investigation to periods lower than the observational time span (Fig. 5.10).

The highest peak occurs at $P \sim 530$ days (0.00189 $\mathrm{d^{-1}}$), with p-value=0.1% estimated through a bootstrap (with re-sampling) analysis. Despite the statistical significance, we cannot conclude anything about the physical nature of this signal, but only ascertain the existence of a possible long-term variability, due to the poor sampling of our dataset and the fact that it does not cover the minimum two cycles necessary for verifying the actual

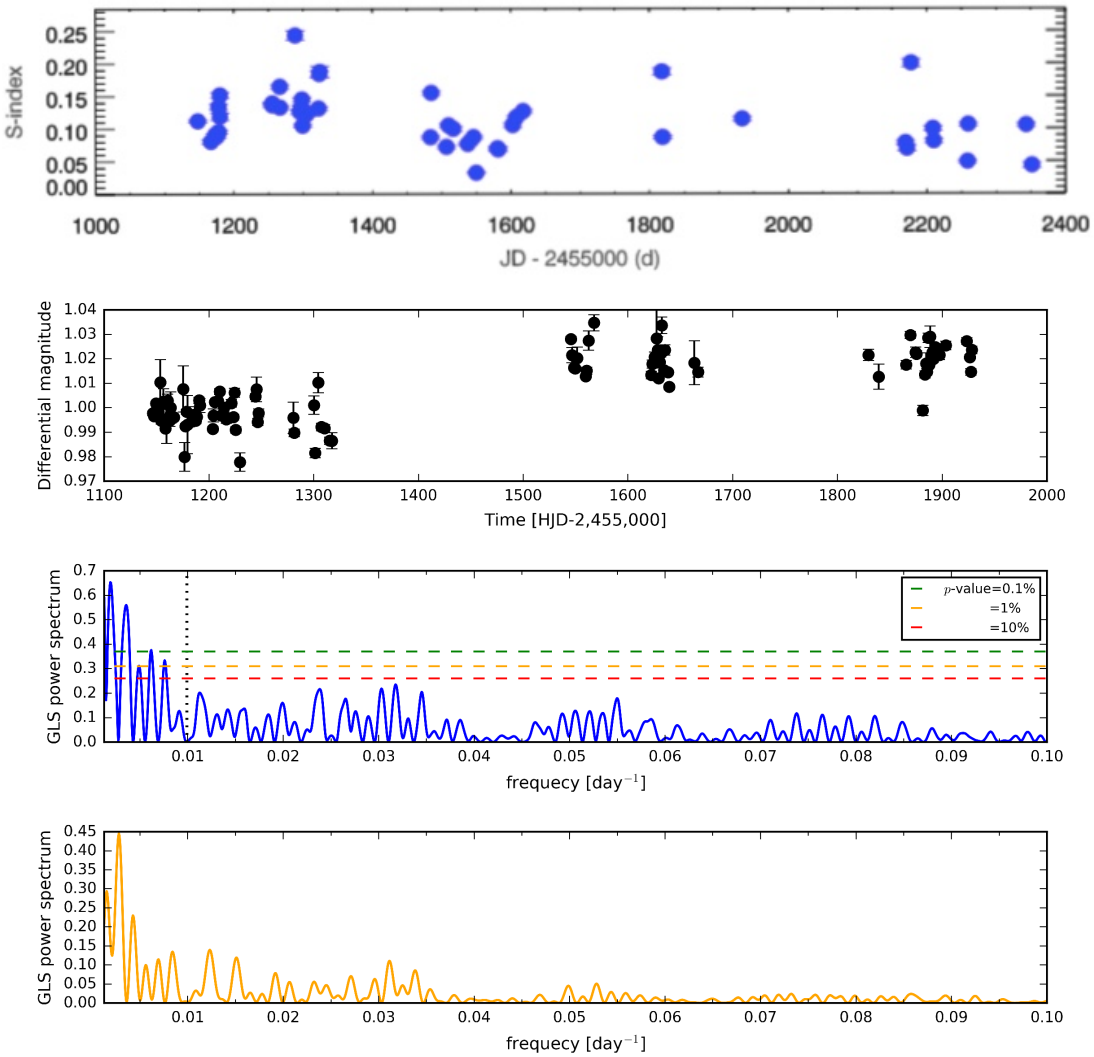

Figure 5.10: *Upper panel*: Time serie of the S-index. *Middle-Upper panel*: Differential light curve of TYC 4282-605-1 collected by the APACHE survey. *Middle-Bottom panel*: Generalized Lomb-Scargle (GLS) periodogram of the differential light curve. The dotted vertical line marks the orbital period of the TYC 4282-605-1 companion. *Bottom panel*: Spectral window function of the APACHE observations.

periodic modulation.

However we note that the signal could coincide with the long-term signal found in the activity indicators (bisector, S-index) and present in the residuals of the radial velocity (See Fig. 5.9) likely linked to the rotation of the star. We note that the light curve (see Fig. 5.10,

second panel) presents an offset between the first season and the rest of the observations. The increase occurring between the first and second season seems to correspond to a decrease of S-index (see upper panel of Fig. 5.10). This is suggestive of an activity long-term effect, with higher activity during the first season (low photometry and high S-index) and low activity level during the second and third seasons.

What is more relevant here is that the periodogram, that considers the three observing seasons, does not show significant signals at or close to $P \sim 101$ days. The same result is obtained when the observing seasons have been analysed separately and this also occurs for the residuals (not showed). This lack of photometric signal at 101 days is another point against radial pulsation as origin of the RV variability (see Sect. 5.1.5.1).

5.1.7 GIANO NIR observations

5.1.7.1 Observations and data reduction

With the goal to compare the radial velocity amplitude in optical and infrared to further check the origin of the observed radial velocity periodicity we have collected seven NIR spectra from May 2015 to August 2015 (time coverage 100 days) with GIANO-A at the TNG, with the epochs of observation carefully selected to optimise the covering phase found with HARPS-N optical data.

Our observations were collected with the original configuration of GIANO-A at the Nasmyth-B focus (Oliva et al. 2006) of TNG. It was fiber-fed with two fibers of 1 arcsec angular diameter at a fixed angular distance of 3 arcsec on sky. An image slicer subdivides the light beam from each fiber so the echellogram is composed by four traces instead of two. A typical 2D output of GIANO can be seen and is explained in detail in the Chapter 2 (Fig 2.4). The GIANO spectrograph is equipped with a 2048 x 2048 HAWAII-2 detector, allowing us to image almost the whole spectral range over 49 orders, with only small missing regions at the longest wavelengths.

Since GIANO is not equipped yet with a gas absorption cell for high precision radial velocities measurements, we obtained the RVs by using the telluric lines as a reference. However, our method can be easily adapted with absorption cells that are now planned in an upgrade of this instrument.

To extract and wavelength-calibrate the GIANO spectra, we have used the ECHELLE package in IRAF and some new, ad hoc scripts that have been grouped in a package named

GIANO TOOLS [V]. The GIANO data reduction manual [VI] with a detailed description is available on the TNG website and in section 2.1 we reported the main steps followed in the reduction of the spectra obtained with GIANO and used in this work.

Observations of science targets are performed by nodding-on-fiber technique, i.e. target and sky are taken in pairs and alternatively acquired on fiber A and B, respectively, for an optimal subtraction of the detector noise and background. From each pair of exposure, an (A-B) 2D-spectrum is computed and then is extracted and summed to get a final 1D wavelength-calibrated spectrum with the best possible signal-to-noise ratio. The spectra in this work were obtained with 600s integration time for each nodding.

2D-spectra of halogen lamps are used to map the geometry of the four spectra in each order, for optimal extraction purposes. The four spectra in each order are independently extracted and wavelength-calibrated, to minimise feature smearing in wavelength due to the small distortion of the slit image along the spatial direction. The instrument is stable enough that flat-fields taken during the daytime are perfectly suited for this purpose.

Each extracted spectrum is wavelength-calibrated by using the U-Ne lamp reference spectra taken at the end of the night. We use a set of approximately 30 bright lines (mostly Ne lines) distributed over a few orders to obtain a first fit, then the optimal wavelength solution is computed by using $\sim$ 300 U-Ne lines distributed over all orders.

5.1.7.2 Radial velocity computations

In the computation of the RVs in the NIR an ensemble of Interface Definition Language (IDL) procedures was used. It was created to measure RVs with the Cross Correlation Function (CCF) method (Baranne et al. 1979). A brief summary of the procedure is explained in the following and more details can be found in Carleo et al. (2016).

- Pre-reduction: spectrum normalisation

  The first step is to have a uniform wavelength scale of the spectra and it is necessary to re-sampling the original ones in order to have a constant step in RV and reduce the RV errors. The re-sampling should be made with the same steps for stellar and telluric lines. In order to re-sample the individual order of the input spectrum we make use of a third degree cubic spline interpolation and a continuum normalisation.

[V] Available on `http://www.tng.iac.es/instruments/giano/`
[VI] `http://www.bo.astro.it/giano/documents/handbook_giano_v1.2.0.pdf`

- Subtraction of telluric contribution

  The goal is to obtain the stellar spectrum cleaned from telluric lines. First a median spectrum of the Earth atmosphere was created in order to subtract it from the normalised stellar spectra. In the same way, the telluric spectrum cleaned from stellar contribution is obtained. Therefore, for each science observation we obtained two cleaned spectra: the stellar spectrum without telluric lines, and the telluric spectrum without the stellar contribution, both of them are used in order to derive the stellar and telluric RV.

- Stellar mask

  We use the CCF method, correlating the spectrum with a mask. It was necessary to prepare two masks, for the stellar and telluric spectra, respectively. It is important that the same mask is used for all the stellar spectra in order to obtain the variations of RVs rather than their absolute values. From the re-sampled, normalised and cleaned spectra (star and telluric), we built a list of stellar lines and masks.

- Telluric mask

  The line list of the telluric target, just like stellar mask, is obtained by considering the median telluric spectrum. Using the line list obtained with the normalised spectra of the telluric standard it is possible to build the telluric mask. We chose only the telluric lines with a similar intensity to the stellar lines.

- Subtraction of stellar contribution

  The stellar and telluric spectra can contaminate each other, therefore we subtract the stellar template in order to obtain telluric spectrum without stellar contribution.

- High precision RVs

  The subtraction of the telluric RV from the star RV gives the final RV for each spectrum, $\mathrm{RV} = \mathrm{RV}_{\mathrm{star}} - \mathrm{RV}_{\mathrm{tell}}$ and the internal errors are obtained taking into account the weight of each order and assuming that S/N is given only by statistics of photons. The total error for one specific order is the combination of the telluric and stellar contribution.

The RV errors computed as above vary from epoch to epoch with a mean value about 18 ms^{-1}. The final RV and the corresponding error for each epoch is listed in Table 5.6.

Table 5.6: Measurements of radial velocity with GIANO

Epoch [BJD]	RV [kms^{-1}]	error [kms^{-1}]
57169.709	-12.869	0.016
57174.706	-13.005	0.026
57177.701	-12.942	0.017
57208.728	-12.078	0.014
57210.714	-12.133	0.017
57236.601	-12.676	0.021
57259.755	-12.959	0.014

5.1.7.3 Consistency between optical and IR data

In order to confirm or reject the companion hypothesis of the RV variations observed in the K giant, we used a set of high precision optical and NIR RVs to search for consistency between the two wavelength domains.

The orbital parameters that characterise a Keplerian orbit have been derived from the optical RVs (see Table 5.4). Because of the smaller number of data points in NIR than in the optical, we only fitted the Keplerian orbit to the GIANO RVs for the RV semi-amplitude (K_{IR}) and systemic velocity (γ_{IR}), keeping the other parameters (P, T_P, e) fixed at the values derived from the optical RVs. The obtained values in NIR are $\gamma_{IR} = -12,560.42 \pm 6.46$ m/s and $K_{IR} = 477.6 \pm 9.5$ m/s. The different value between center of mass RV (γ) in optical and NIR enables us to determine the offset between the two datasets. It is important to note that before the observations with GIANO, we have simulated several possible strategies in order to have the best phase coverage and number of observations. We obtained the best results concentrating the observations at phases close to the minimum and maximum, with few observations at the other phases.

The seven NIR Doppler points from GIANO plotted in Fig. 5.11 were corrected by offset and median of RV, but were not used for fitting. In Fig. 5.11 we find that the GIANO data follow the Keplerian model predicted by HARPS-N RVs. The NIR data have an excellent phase coverage (one full period) and have consistent amplitude (1.5 σ) with the optical data. Our results support the hypothesis of an orbiting companion around the K giant star TYC 4282-605-1 with the orbital parameters list on Table 5.4.

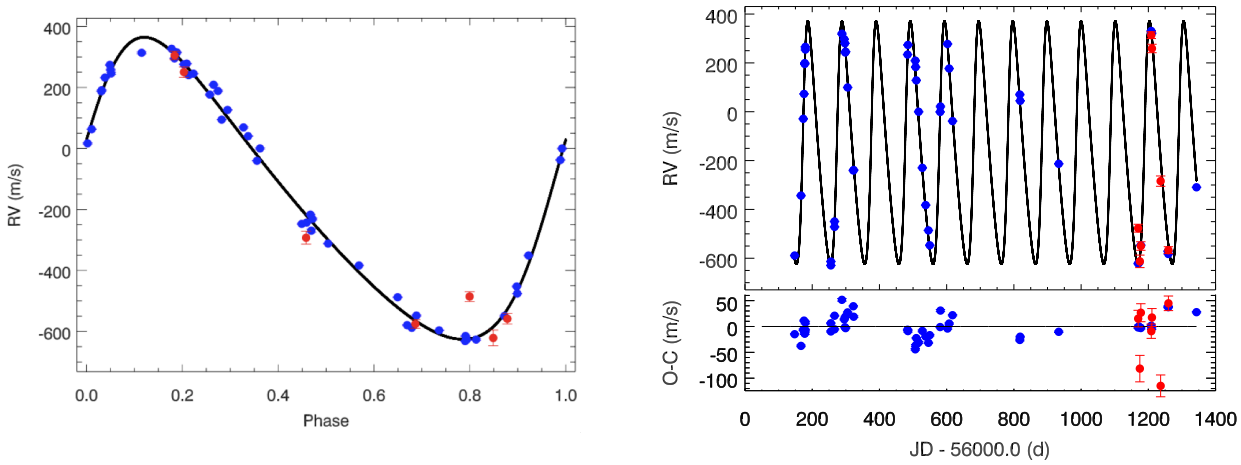

Figure 5.11: GIANO NIR radial velocity with red circles and HARPS-N optical RVs with blue circles. The best fit Keplerian model obtained from optical data is plotted with a solid black line. *The left panel* shows the RV data in function of the phase. *The right panel* shows the RV as a function of the time and the residuals information. The NIR radial velocities (in red) are in excellent agreement with the optical data (in blue).

5.1.8 Implication on the star and planet properties

We have reported the discovery of a sub-stellar companion around K giant star TYC 4282-605-1. We note that this is the first time that IR+optical RV measurements were used to confirm a planet discovery around a K giant. The main orbital properties are the following: $M_P \sin i = 10.78 \pm 0.12$ M_J; $P = 101.54 \pm 0.05$ days; $e = 0.28 \pm 0.01$; $a = 0.422 \pm 0.009$ AU.

It is possible to establish an upper-limit to the mass of the low-mass companion taking advantage of the knowledge of the eccentricity and imposing that the minimum distance from the star cannot be smaller than the stellar radius (16 $R_\odot$). We obtain an upper limit of 40 M_J resulting in a range of mass between 10 and 40 M_J for our sub-stellar companion.

Our planet is rather close to its parent star with $asini/R \sim 5$. This poses it close to the limiting value $a/R \sim 3$ that Villaver et al. (2014) estimated from the fast tidal decay of the planetary orbits in their models. Indeed they find that only three planets around red giant branch (RGB) stars have $a/R < 10$ considering the observations collected till September 1st 2013. Our star is less massive than most of the RGB hosts that have masses between 1.2 and 2.8 $M_\odot$ (cf. Fig. 12 in Villaver et al. 2014) so the radius inflation during its ascent along the red giant branch was slower giving a longer remaining lifetime to the planet. The orbit of our planet is significantly eccentric and allows us to apply the theory by Verbunt & Phinney

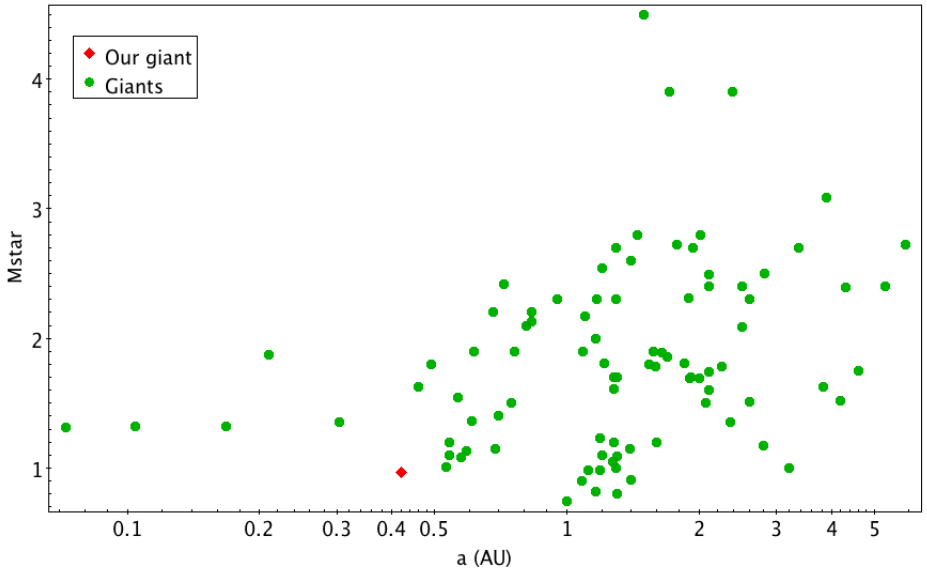

Figure 5.12: Observed orbital distance vs. stellar mass for known planets orbiting giant stars taken from the Heidelberg group (https://www.lsw.uni-heidelberg.de/users/sreffert/giantplanets/giantplanets.php)

(1995) to estimate the decrease of the eccentricity due to tides inside the red giant host after it left the main sequence. Considering Eqs. (6) and (9) of Verbunt & Phinney (1995), we estimate that $e \sim 0.35$ when the star ended its main-sequence evolution because tides did not have time to circularise and shrink the orbit given that the star was still on the initial phase of the red giant branch ascent. If our star were a red clump giant or were ascending the asymptotic giant branch, that is, if it were a core or shell helium-burning object that previously reached the red giant tip, the planet would have been engulfed during the phase of rapid radius increase during the red giant branch ascent and would not be there. We expect that the planet will be engulfed by the star in the next evolutionary phase and indeed today it is one of the closest planet to its host star (see Fig. 5.12, see also Fig. 12 in Villaver et al. 2014). In other words, the presence of the planet and its eccentric orbit are a strong argument in favour of our previous estimate of the evolutionary phase and mass of our star.

5.1.9 Summary and conclusions

Our goal was to determine the origin of the periodic variability found with HARPS-N in optical band using also NIR radial velocity measurements. The comparison between the amplitude variations in two different bands allowed us to understand the origin of the periodicity

of RV time series.

We obtained NIR RVs with the GIANO spectrograph derived by an ensemble of IDL procedures created to measure RVs with the CCF method. The NIR RVs are in excellent agreement with the optical data obtained with HARPS-N, following the best Keplerian model prediction and being consistent in amplitude. Thus, we confirm the presence of a substellar companion around the giant star after a careful analysis to exclude a stellar origin of the signal thanks to the study of the photometric light curve, the bisector time series and the RV analysis in NIR with GIANO.

In this work we have also studied the chemical abundance of the K giant to explain the nature of the enhancement found for some of α-elements. Based on the study done by Alves-Brito et al. (2010) and the derived kinematic properties for the target, we can conclude that our K giant it is compatible with a star located in the local thick disk.

We have shown the capability of GIANO to discern the presence of a companion around a giant star and further studies would benefit from the ongoing efforts to use HARPS-N and GIANO-B in a simultaneous way. This can be considered a pilot study for the GIARPS project (GIANO-B + HARPS-N) with which is possible to take in a single exposure a high resolution spectrum from 0.383 to 2.45 μm. This upgrade will make future observations more efficient, providing precious information on the origin of the radial velocity variations.

Chapter 6

Summary and conclusions

In this thesis we discuss in detail the relevance of the stellar activity effects on the search for planetary companions through the RV method and how important it is specially in the study of M dwarf stars. Our data were taken at Telescopio Nazionale Galileo (TNG) using the echelle spectrograph HARPS-N in visible range and GIANO echelle spectrograph in the NIR. Observations and data reduction are explained in chapter 2. Knowing that the stellar activity is a big challenge with which we have to deal in order to disentangle stellar signals from those of keplerian origin, then we specially focused on how the coronal and chromospheric activity behave in M dwarf stars (chapter 3). The search for planets has recently focused on these stars because of their several advantages despite of their high levels of activity that make difficult their study. In chapter 3, we have been able to conclude that our sample follows the same trends as FGK stars and other late-K/early-M studied in the literature and allow us an extension of the analysis of the Ca II H & K and $H\alpha$ flux-flux relationships of main-sequence dwarfs to the low flux domain. Another important work was the study of the rotation period - activity relationship where we extended the up to now available sample of dM stars to the non-saturated X-ray emission regime. Most of the work discussed in this chapter is part of several published paper within the HADES collaboration: Scandariato et al. (2017), Maldonado et al. (2017) and Suárez Mascareño et al. (A&A, in press).

Regarding the search for planets around M stars (chapter 4) we present a candidate planet around the M dwarf GJ 720 A, whose radial velocity curve shows a high periodic signal at $\sim$ 19 days, possibly of keplerian origin. Further tests are planned to corroborate this hypothesis. In order to present on a true case the problems arising from the activity in

the RV study of low-mass stars we discuss the case of GJ 521 A.

A different analysis has been done in chapter 5 on a red giant star, TYC 4282-605-1. For this kind of stars the origin of the astrophysical noise, that can hamper the possibility to identify planets, is linked to the pulsating modes. For this target we discovered an orbiting low-mass companion at 101 days by making use of a multi-wavelength approach. To the best of our knowledge it is the first time that RVs in VIS and NIR are used quasi-simultaneously to confirm a planet around a giant star. This discovery is published in González-Álvarez et al. (2017).

This project has been a pilot programme for the GIARPS project, the new observing mode at TNG that use at the same time HARPS-N and GIANO, splitting the stellar light and feeding simultaneously the two spectrographs. This new mode very useful in presence of significant activity, has already applied to Carleo et al. (A&A submitted)

6.1 List of articles

- HADES RV Programme with HARPS-N at TNG. III. Flux-flux and activity-rotation relationships of early-M dwarfs, Maldonado et al. (2017), A&A, 598, A27

- HADES RV Programme with HARPS-N at TNG. IV.Time resolved analysis of the Ca II H & K and Hα chromospheric emission of low-activity early-M dwarfs, Scandariato et al. (2017), A&A, 598, A28

- GIARPS@TNG: GIANO-B and HARPS-N together for a wider wavelength range spectroscopy, Claudi et al. (2017), EPJP, Volume 132, Issue 8, article id.364, 8 pp

- The GAPS Programme with HARPS-N at TNG. XV. A substellar companion around a K giant star identified with quasi-simultaneous HARPS-N and GIANO measurements, González-Álvarez et al. (2017), A&A, 606, A51

- HADES RV Programme with HARPS-N at TNG. VII. Rotation and activity of M-Dwarfs from time-series high-resolution spectroscopy of chromospheric indicators, Suárez Mascareño et al. 2017 (A&A, in press)

- Multi-band high resolution spectroscopy rules out the hot Jupiter BD+20 1790b, First results from GIARPS Commissioning, Carleo et al. 2017 (A&A submitted)

- The GAPS Programme with HARPS-N at TNG XVII. Measurement of the Rossiter-McLaughlin effect of the transiting planetary systems HAT-P-3, HAT-P-12, HAT-P-22, WASP-39 and WASP-60, Mancini et al. 2017 (A&A submitted)

- Eyes on K2-3: A court of three likely sub-Neptunes characterized with HARPS-N and HARPS, Damasso et al. 2017 (A&A submitted)

Bibliography

Affer, L., Micela, G., Damasso, M., et al. 2016, A&A, 593, A117

Alonso, A., Arribas, S., & Martínez-Roger, C. 1999, A&AS, 140, 261

Alves-Brito, A., Meléndez, J., Asplund, M., Ramírez, I., & Yong, D. 2010, A&A, 513, A35

Anglada-Escudé, G. & Butler, R. P. 2012, ApJS, 200, 15

Baranne, A., Mayor, M., & Poncet, J. L. 1979, Vistas in Astronomy, 23, 279

Baranne, A., Queloz, D., Mayor, M., et al. 1996, A&AS, 119, 373

Bean, J. L., Seifahrt, A., Hartman, H., et al. 2010, ApJ, 713, 410

Bensby, T., Feltzing, S., & Lundström, I. 2004, A&A, 421, 969

Boller, T., Freyberg, M. J., Trümper, J., et al. 2016, A&A, 588, A103

Borucki, W. J., Koch, D., Basri, G., et al. 2010, Science, 327, 977

Bozza, V., Mancini, L., & Sozzetti, A., eds. 2016, Astrophysics and Space Science Library, Vol. 428, Methods of Detecting Exoplanets

Bressan, A., Marigo, P., Girardi, L., et al. 2012, MNRAS, 427, 127

Browning, M. K., Basri, G., Marcy, G. W., West, A. A., & Zhang, J. 2010, AJ, 139, 504

Carleo, I. & Gratton, R. 2015, Mem. Soc. Astron. Italiana, 86, 478

Carleo, I., Sanna, N., Gratton, R., et al. 2016, Experimental Astronomy, 41, 351

Chaplin, W. J. & Miglio, A. 2013, ARA&A, 51, 353

Chauvin, G., Lagrange, A.-M., Dumas, C., et al. 2004, A&A, 425, L29

Claudi, R., Benatti, S., Carleo, I., et al. 2017, European Physical Journal Plus, 132, 364

Claudi, R., Benatti, S., Carleo, I., et al. 2016, in Proc. SPIE, Vol. 9908, Society of Photo-Optical Instrumentation Engineers (SPIE) Conference Series, 99081A

Cosentino, R., Lovis, C., Pepe, F., et al. 2012, in Proc. SPIE, Vol. 8446, Ground-based and Airborne Instrumentation for Astronomy IV, 84461V

Covino, E., Esposito, M., Barbieri, M., et al. 2013, A&A, 554, A28

Cutri, R. M., Skrutskie, M. F., van Dyk, S., et al. 2003, VizieR Online Data Catalog, 2246

Damasso, M., Biazzo, K., Bonomo, A. S., et al. 2015, A&A, 575, A111

Dawson, R. I. & Fabrycky, D. C. 2010, ApJ, 722, 937

De Ridder, J., Barban, C., Baudin, F., et al. 2009, Nature, 459, 398

Dehnen, W. & Binney, J. J. 1998, MNRAS, 298, 387

Delfosse, X., Forveille, T., Perrier, C., & Mayor, M. 1998, A&A, 331, 581

D'Orazi, V., Biazzo, K., Desidera, S., et al. 2012, MNRAS, 423, 2789

D'Orazi, V., Biazzo, K., & Randich, S. 2011, A&A, 526, A103

D'Orazi, V., Desidera, S., Gratton, R. G., et al. 2017, A&A, 598, A19

Dressing, C. D. & Charbonneau, D. 2013, ApJ, 767, 95

Elgaroy, O., Engvold, O., & Joras, P. 1997, A&A, 326, 165

Endl, M., Kürster, M., Els, S., Hatzes, A. P., & Cochran, W. D. 2001, A&A, 374, 675

Esposito, M., Covino, E., Mancini, L., et al. 2014, A&A, 564, L13

Fleming, T. A., Molendi, S., Maccacaro, T., & Wolter, A. 1995, ApJS, 99, 701

Gaia Collaboration, Prusti, T., de Bruijne, J. H. J., et al. 2016, A&A, 595, A1

González-Álvarez, E., Affer, L., Micela, G., et al. 2017, A&A, 606, A51

Hatzes, A. P. 1999, in Astronomical Society of the Pacific Conference Series, Vol. 185, IAU Colloq. 170: Precise Stellar Radial Velocities, ed. J. B. Hearnshaw & C. D. Scarfe, 259

Hatzes, A. P. 2002, Astronomische Nachrichten, 323, 392

Hatzes, A. P. & Cochran, W. D. 2000, AJ, 120, 979

Hatzes, A. P., Kanaan, A., & Mkrtichian, D. 1999, in Astronomical Society of the Pacific Conference Series, Vol. 185, IAU Colloq. 170: Precise Stellar Radial Velocities, ed. J. B. Hearnshaw & C. D. Scarfe, 166

Hekker, S. & Christensen-Dalsgaard, J. 2016, ArXiv e-prints

Henry, T. J., Jao, W.-C., Subasavage, J. P., et al. 2006, AJ, 132, 2360

Henry, T. J., Soderblom, D. R., Donahue, R. A., & Baliunas, S. L. 1996, AJ, 111

Høg, E., Fabricius, C., Makarov, V. V., et al. 2000, A&A, 355, L27

Horne, K. 1986, PASP, 98, 609

Howard, A. W., Marcy, G. W., Bryson, S. T., et al. 2012, ApJS, 201, 15

Huensch, M., Schmitt, J. H. M. M., & Voges, W. 1998, A&AS, 132, 155

Hünsch, M., Schmitt, J. H. M. M., Sterzik, M. F., & Voges, W. 1999, A&AS, 135, 319

Isobe, T., Feigelson, E. D., Akritas, M. G., & Babu, G. J. 1990, ApJ, 364, 104

Johnson, D. R. H. & Soderblom, D. R. 1987, AJ, 93, 864

Kasting, J. F., Whitmire, D. P., & Reynolds, R. T. 1993, Icarus, 101, 108

Kjeldsen, H. & Bedding, T. R. 2011, A&A, 529, L8

Kosovichev, A. G., de Gouveia Dal Pino, E., & Yan, Y., eds. 2013, IAU Symposium, Vol. 294, Solar and Astrophysical Dynamos and Magnetic Activity

Kurucz, R. 1993, ATLAS9 Stellar Atmosphere Programs and 2 km/s grid. Kurucz CD-ROM No. 13. Cambridge, Mass.: Smithsonian Astrophysical Observatory, 1993., 13

Lépine, S. & Gaidos, E. 2011, AJ, 142, 138

Leto, G., Pagano, I., Buemi, C. S., & Rodono, M. 1997, A&A, 327, 1114

Linsky, J. L. 1980, ARA&A, 18, 439

López-Santiago, J., Montes, D., Gálvez-Ortiz, M. C., et al. 2010, A&A, 514, A97

Lovis, C., Dumusque, X., Santos, N. C., et al. 2011, ArXiv e-prints

Lovis, C. & Pepe, F. 2007, A&A, 468, 1115

Lutz, T. E. & Kelker, D. H. 1973, PASP, 85, 573

Maggio, A., Sciortino, S., Vaiana, G. S., et al. 1987, ApJ, 315, 687

Maldonado, J., Affer, L., Micela, G., et al. 2015a, A&A, 577, A132

Maldonado, J., Eiroa, C., Villaver, E., Montesinos, B., & Mora, A. 2015b, A&A, 579, A20

Maldonado, J., Martínez-Arnáiz, R. M., Eiroa, C., Montes, D., & Montesinos, B. 2010, A&A, 521, A12

Maldonado, J., Scandariato, G., Stelzer, B., et al. 2017, A&A, 598, A27

Martínez-Arnáiz, R., López-Santiago, J., Crespo-Chacón, I., & Montes, D. 2011, MNRAS, 414, 2629

Martínez-Arnáiz, R., Maldonado, J., Montes, D., Eiroa, C., & Montesinos, B. 2010, A&A, 520, A79

Martínez Fiorenzano, A. F., Gratton, R. G., Desidera, S., Cosentino, R., & Endl, M. 2005, A&A, 442, 775

Matt, S. P., Brun, A. S., Baraffe, I., Bouvier, J., & Chabrier, G. 2015, ApJ, 799, L23

Mayor, M., Pepe, F., Queloz, D., et al. 2003, The Messenger, 114, 20

Mayor, M. & Queloz, D. 1995, Nature, 378, 355

Melo, C. H. F., Pasquini, L., & De Medeiros, J. R. 2001, A&A, 375, 851

Montes, D., Fernandez-Figueroa, M. J., Cornide, M., & de Castro, E. 1996a, in Astronomical Society of the Pacific Conference Series, Vol. 109, Cool Stars, Stellar Systems, and the Sun, ed. R. Pallavicini & A. K. Dupree, 657

Montes, D., Fernandez-Figueroa, M. J., Cornide, M., & de Castro, E. 1996b, A&A, 312, 221

Montes, D., Fernandez-Figueroa, M. J., de Castro, E., & Cornide, M. 1995, A&A, 294, 165

Montes, D., López-Santiago, J., Fernández-Figueroa, M. J., & Gálvez, M. C. 2001, A&A, 379, 976

Nardetto, N., Poretti, E., Rainer, M., et al. 2017, A&A, 597, A73

Newton, E. R., Irwin, J., Charbonneau, D., et al. 2017, ApJ, 834, 85

Newton, E. R., Irwin, J., Charbonneau, D., Berta-Thompson, Z. K., & Dittmann, J. A. 2016, ApJ, 821, L19

Noyes, R. W. 1984, Advances in Space Research, 4, 151

Noyes, R. W., Hartmann, L. W., Baliunas, S. L., Duncan, D. K., & Vaughan, A. H. 1984, ApJ, 279, 763

Oliva, E., Origlia, L., Baffa, C., et al. 2006, in Proc. SPIE, Vol. 6269, Society of Photo-Optical Instrumentation Engineers (SPIE) Conference Series, 626919

Origlia, L., Oliva, E., Baffa, C., et al. 2014, in Proc. SPIE, Vol. 9147, Ground-based and Airborne Instrumentation for Astronomy V, 91471E

Osten, R. A., Hawley, S. L., Allred, J. C., Johns-Krull, C. M., & Roark, C. 2005, ApJ, 621, 398

Pallavicini, R., Golub, L., Rosner, R., et al. 1981, ApJ, 248, 279

Park, S., Kang, W., Lee, J.-E., & Lee, S.-G. 2013, AJ, 146, 73

Pepe, F., Mayor, M., Galland, F., et al. 2002, A&A, 388, 632

Percy, J. R., Wilson, J. B., & Henry, G. W. 2001, PASP, 113, 983

Perger, M., García-Piquer, A., Ribas, I., et al. 2017, A&A, 598, A26

Pizzolato, N., Maggio, A., Micela, G., Sciortino, S., & Ventura, P. 2003, A&A, 397, 147

Poretti, E. & Antonello, E. 1988, A&A, 199, 191

Poretti, E., Mathias, P., Barban, C., et al. 2015, in Astrophysics and Space Science Proceedings, Vol. 39, Asteroseismology of Stellar Populations in the Milky Way, ed. A. Miglio, P. Eggenberger, L. Girardi, & J. Montalbán, 101

Ptak, A. & Griffiths, R. 2003, in Astronomical Society of the Pacific Conference Series, Vol. 295, Astronomical Data Analysis Software and Systems XII, ed. H. E. Payne, R. I. Jedrzejewski, & R. N. Hook, 465

Queloz, D., Henry, G. W., Sivan, J. P., et al. 2001, A&A, 379, 279

Randich, S., Schmitt, J. H. M. M., Prosser, C. F., & Stauffer, J. R. 1996, A&A, 305, 785

Reid, I. N., Gizis, J. E., & Hawley, S. L. 2002, AJ, 124, 2721

Reid, I. N., Hawley, S. L., & Gizis, J. E. 1995, AJ, 110, 1838

Reiners, A., Joshi, N., & Goldman, B. 2012, AJ, 143, 93

Robertson, P., Mahadevan, S., Endl, M., & Roy, A. 2014, Science, 345, 440

Robinson, R. D., Cram, L. E., & Giampapa, M. S. 1990, ApJS, 74, 891

Rosen, S. R., Webb, N. A., Watson, M. G., et al. 2016, A&A, 590, A1

Saar, S. H. & Donahue, R. A. 1997, ApJ, 485, 319

Sanz-Forcada, J., Micela, G., Ribas, I., et al. 2011, A&A, 532, A6

Saxton, R. D., Read, A. M., Esquej, P., et al. 2008, A&A, 480, 611

Scandariato, G., Maldonado, J., Affer, L., et al. 2017, A&A, 598, A28

Scheffler, H. & Elsasser, H. 1988, Science, 240, 1680

Schmitt, J. H. M. M., Fleming, T. A., & Giampapa, M. S. 1995, ApJ, 450, 392

Schmitt, J. H. M. M. & Liefke, C. 2004, A&A, 417, 651

Sneden, C. 1973, ApJ, 184, 839

Sousa, S. G., Santos, N. C., Israelian, G., Mayor, M., & Monteiro, M. J. P. F. G. 2007, A&A, 469, 783

Sozzetti, A., Bernagozzi, A., Bertolini, E., et al. 2013, in European Physical Journal Web of Conferences, Vol. 47, European Physical Journal Web of Conferences, 03006

Stassun, K. G., Hebb, L., Covey, K., et al. 2011, in Astronomical Society of the Pacific Conference Series, Vol. 448, 16th Cambridge Workshop on Cool Stars, Stellar Systems, and the Sun, ed. C. Johns-Krull, M. K. Browning, & A. A. West, 505

Steffen, M. 1985, A&AS, 59, 403

Stelzer, B., Alcalá, J., Biazzo, K., et al. 2012, A&A, 537, A94

Stelzer, B., Damasso, M., Scholz, A., & Matt, S. P. 2016, in 19th Cambridge Workshop on Cool Stars, Stellar Systems, and the Sun (CS19), 62

Stelzer, B., Frasca, A., Alcalá, J. M., et al. 2013a, A&A, 558, A141

Stelzer, B., Marino, A., Micela, G., López-Santiago, J., & Liefke, C. 2013b, MNRAS, 431, 2063

Stempels, H. C., Gahm, G. F., & Petrov, P. P. 2007, A&A, 461, 253

Strassmeier, K. G., Fekel, F. C., Bopp, B. W., Dempsey, R. C., & Henry, G. W. 1990, ApJS, 72, 191

Suárez Mascareño, A., Rebolo, R., González Hernández, J. I., & Esposito, M. 2015, MNRAS, 452, 2745

Truemper, J. 1992, QJRAS, 33, 165

Valenti, J. A. & Fischer, D. A. 2005, ApJS, 159, 141

Verbunt, F. & Phinney, E. S. 1995, A&A, 296, 709

Vidotto, A. A., Jardine, M., Morin, J., et al. 2013, A&A, 557, A67

Villaver, E., Livio, M., Mustill, A. J., & Siess, L. 2014, ApJ, 794, 3

Voges, W., Aschenbach, B., Boller, T., et al. 1999, A&A, 349, 389

West, A. A., Weisenburger, K. L., Irwin, J., et al. 2015, ApJ, 812, 3

Wood, P. R., Olivier, E. A., & Kawaler, S. D. 2004, ApJ, 604, 800

Wright, J. T. & Howard, A. W. 2009, ApJS, 182, 205

Wright, N. J., Drake, J. J., Mamajek, E. E., & Henry, G. W. 2011, ApJ, 743, 48

Zacharias, N., Finch, C. T., Girard, T. M., et al. 2012, VizieR Online Data Catalog, 1322

Zechmeister, M. & Kürster, M. 2009, A&A, 496, 577